Ph.D. 9091

THE EROSION OF DUCTILE METALS BY SOLID PARTICLES

by

Ian Michael Hutchings

A dissertation submitted to the University of Cambridge
for the degree of Doctor of Philosophy

October 1974

Trinity College
Cambridge

UNIVERSITY
LIBRARY
CAMBRIDGE

Preface

The work described in this dissertation was carried out between October 1971 and August 1974 in the Physics and Chemistry of Solids sub-department of the Cavendish Laboratory, Cambridge, under the supervision of Dr J. E. Field.

I am very grateful to Professor D. Tabor, F.R.S., for the opportunity to join the Laboratory and for the interest he has shown in my work. Dr Field has been a source of constant encouragement and I am particularly indebted to him for his helpful comments on the manuscript and for his expert advice on high-speed photography.

I have been considerably influenced by Dr R. E. Winter's original approach to research and would like to thank him for his infectious enthusiasm and for many helpful discussions.

My thanks are also due to Mr A. H. Peck for the excellence of his photographic work.

The work was supported by the Science Research Council which I thank for a Research Studentship.

The work described in this dissertation is entirely original except where reference is made to the work of others and has not been submitted for a degree at any other university.

October 1974

Trinity College,
Cambridge.

Contents

Chapter One

Review of Previous Work

1.1 Introduction

The wear of materials by impacting abrasive particles is a severe problem in many situations. These range from pneumatic pipelines for transporting powders to gas turbine engines operating in sandy or dusty conditions. Rocket motor nozzles, boiler tubes and fans used in heavy industry all suffer from erosive wear, which is in many cases the major cause of failure of the machine or component concerned. There is therefore a considerable economic incentive to investigate the process of erosion; not only may the wear of machinery be reduced, but constructive applications of the process might be further developed. Erosive cutting of rock and the cleaning and preparation of metal surfaces are examples of such uses.

The difficulty of selecting a material with a high resistance to erosion has been recognized for some time; Wahl and Hartstein (1946) summarised the empirical data available then, which included the somewhat surprising fact, since confirmed by many workers, that increasing the hardness of a carbon steel has little effect upon its resistance to erosion. Most early research was devoted to this problem of finding erosion-resistant materials, and little consistent information was gathered about the effects of impact angle and velocity of the impinging particles. In the last twenty years, considerably more has become known about the process of erosion, and several theoretical approaches have been made to the problem; this work will be summarised in the following sections.

1.2 Experimental results

1.2.1 Presentation of data

UNIVERSITY LIBRARY CAMBRIDGE

It is well established that the erosion of a surface,

which may be expressed as weight lost or volume removed, is directly proportional to the total mass of eroding particles which have struck it, all other variables remaining constant. In some cases, an "incubation period" of low erosion precedes the establishment of a constant erosion rate, but such incubation is of short duration, and the erosion thereafter follows the linear relation described.

Erosion may therefore conveniently be quoted as the weight lost per unit mass of impacting particles (dimensionless erosion parameter) or as volume lost per mass of impacting particles. Most authors quote erosion as the dimensionless parameter, but for some purposes the second unit is more useful. Unless otherwise specified, the term "erosion" in this work will be used to refer to the first, dimensionless, quantity.

1.2.2 Typical erosive particles

The particles responsible for erosive wear vary in composition, but are universally harder than the material which they erode. More than 70% of the dust which causes erosion in gas turbine engines in the desert is quartz (Sage and Tilly 1969), and quartz is also a major constituent of flue ash in coal-fired boilers (Raask 1969). Aluminium oxide and silicon carbide particles have been used in many experimental studies of erosion, as well as quartz and sand. Typical erosive particles are between 5 and 500 μm in diameter; impact velocities may be as high as 600 ms^{-1} in gas turbine engines (Goodwin, Sage and Tilly 1969) and as low as 10 ms^{-1} in solid transport systems.

1.2.3 Variation of erosion with angle - ductile and brittle erosion

Figure 1.1 shows the variation of erosion with impact angle for two different target materials. The impact angle is the angle between the particle velocity vector and the target surface, as defined in the figure. The erosion of aluminium is a maximum at $\sim 18^{o}$, and falls to about one third of this value for normal impacts. The

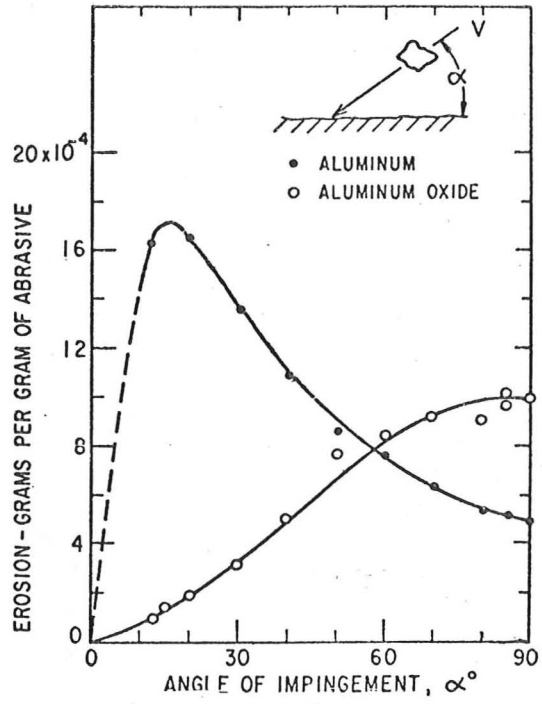

Figure 1.1
The variation of erosion with impact angle for ductile and brittle materials. The particles were silicon carbide grains (100 μm), velocity of impact 156 ms^{-1}. Target materials: aluminium (solid circles) and aluminium oxide (open circles).
(Finnie, Wolak & Kabil 1967)

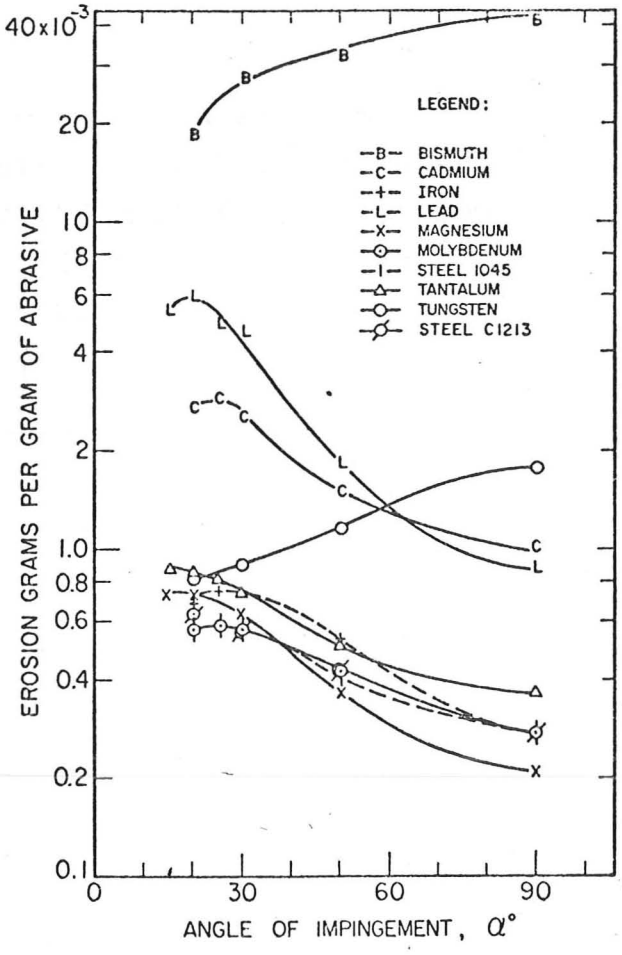

Figure 1.2
The variation of erosion with impact angle for a number of pure metals. 250 μm silicon carbide particles, 78 ms^{-1}.
(Finnie, Wolak & Kabil 1967)

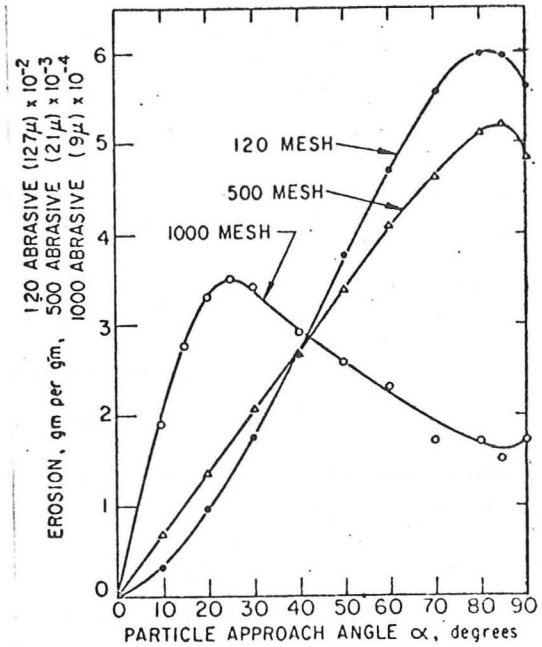

Figure 1.3
The variation of erosion with impact angle for particles of different sizes on a brittle material (plate glass). Particle sizes 120 mesh (127 μm), 500 mesh (21 μm) and 1000 mesh (9 μm), velocity 156 ms^{-1}.
(Sheldon and Finnie 1966b)

behaviour of aluminium oxide (corundum or sapphire) is strikingly different. The erosion rises monotonically to a maximum at 90°. The behaviour of aluminium is typical of a ductile metal, and that of aluminium oxide, of a brittle material. This distinction has been noted by numerous workers, most metals being found to conform to a ductile erosion pattern, and few materials being impossible to classify into either group. Figure 1.2 shows the variation of erosion with angle of impact for a number of metals. All the metals normally considered ductile do indeed show ductile erosion curves, while tungsten and bismuth, which both show brittle erosion characteristics, have very low ductility.

It is important to note that this distinction between ductile and brittle erosion does not only depend upon the bulk properties of the target material, but also upon the size and velocity of the impinging particles. A brittle material may in fact erode in a characteristically ductile manner when the particles are so small that the volume which they deform becomes comparable with the volume between flaws in the material. This effect has been studied by Sheldon and Finnie (1966b); figure 1.3 shows how the erosion of plate glass changes from brittle to ductile as the particle size is reduced.

A distinctive feature of ductile erosion is the formation of surface ripples on the eroded surface. The phenomenon occurs only at shallow impingement angles, and ripples do not form when the erosion is of the brittle type. Finnie and Kabil (1965) have studied this effect in detail.

The sharp distinction between the two types of erosion, brittle and ductile, suggests that the mechanisms by which material is removed by the impacting particles are not the same in the two cases. Sheldon and Finnie (1966a) and Finnie and Oh (1966) have investigated the erosion of brittle materials both experimentally and theoretically, and find a reasonable correlation between their theory and experiment, at least for normal impacts. The theories of ductile erosion are not so satisfactory; this dissertation will deal mainly with this type, and unless qualified, "erosion" will refer to the characteristic ductile mode.

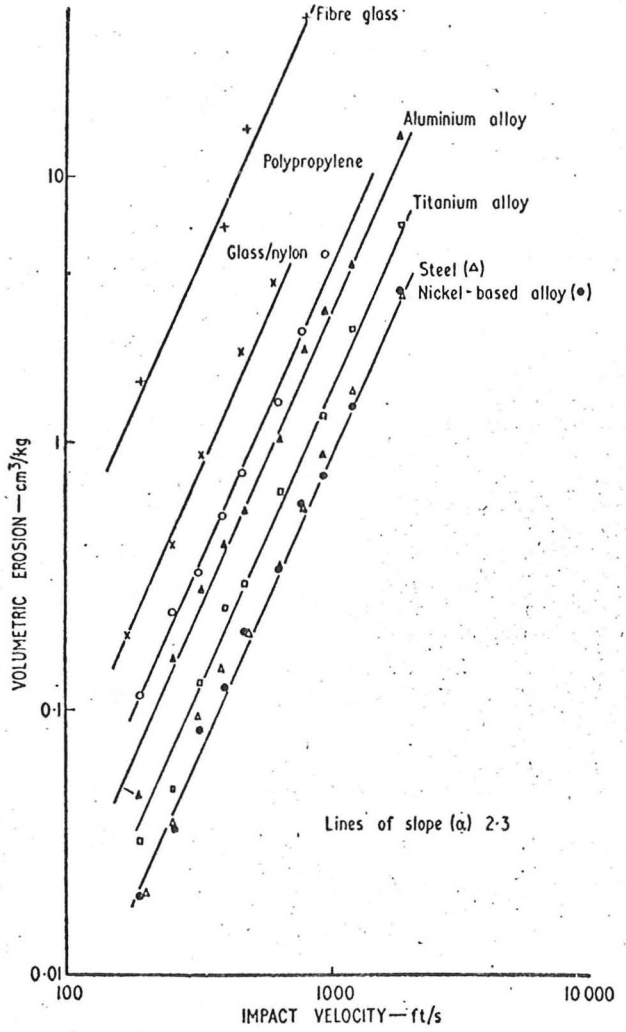

Figure 1.4
The influence of velocity on erosion for various materials. Note the slope of 2.3. Quartz particles,
(Goodwin, Sage & Tilly 1969)

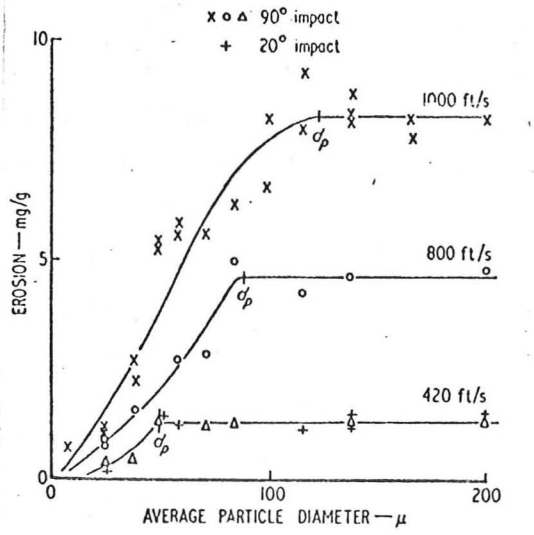

Figure 1.5
The influence of particle size on the erosion of an 11% Cr steel by quartz particles. Impact velocities 312 ms^{-1}, 250 ms^{-1} and 131 ms^{-1}.
(Goodwin, Sage & Tilly 1969)

1.2.4 Variation of erosion with velocity

Many workers have investigated the effect of particle velocity upon erosion, and have found that over a wide range of velocity their results fit an equation of the form

$$\text{Erosion} = Av^n$$

where v is the particle velocity and A depends upon the experimental conditions. The exponent n is always greater than 2.0, values of 2.1 to 2.5 having been obtained by Finnie, Wolak and Kabil (1967) for many pure metals, and the value of 2.3 by Goodwin, Sage and Tilly (1969) for several alloys and non-metals. (see figure 1.4)

Brittle materials tend to exhibit higher values of the velocity exponent than ductile metals; the figure 6.5 has been reported by Finnie (1960) for the erosion of glass by steel shot, and values from 2.5 to 4.4 by Sheldon and Finnie (1966a) for several brittle materials.

1.2.5 Particle size, shape and material

Experimental work has shown that the erosion per unit mass of impacting particles depends to a certain extent upon the size of the particles. Goodwin, Sage and Tilly (1969) found that the erosion (weight loss per unit mass of abrasive) of metals by quartz is linearly dependent upon particle size up to a critical size, and then remains constant for larger particles. Their results are shown in figure 1.5, and are in substantial agreement with those of Kleis (1969), whose investigations extended to considerably larger particles ($\sim$1 mm diameter). Tilly (1973) has also pointed out that below a critical particle size and velocity (e.g. 5 μm and 250 ms^{-1}) the erosion is not measureable.

Even though the magnitude of erosion might change with particle size, it is unlikely that the fundamental mechanisms by which the particles remove material change, since the characteristic ductile erosion curve is retained for particles as small as 9 μm and as large as $\sim$1mm (Kleis 1969). Figure 1.6 shows superimposed curves for 9 and 127 μm particles.

The shape of the eroding particles certainly affects the wear rate, but it is difficult to obtain information on the effects of shape alone, since particle fragility also

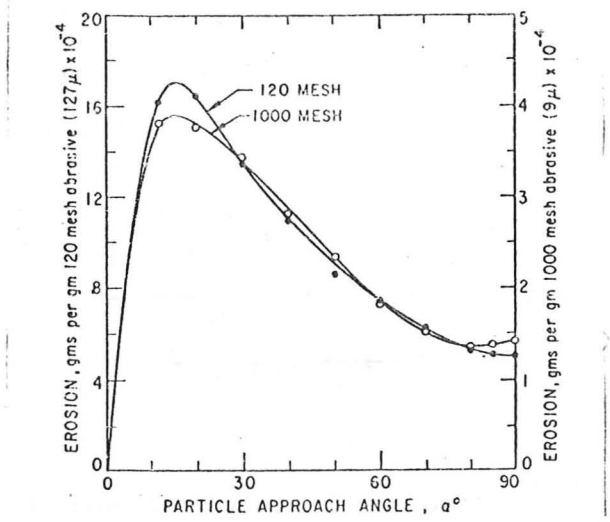

Figure 1.6
The variation of erosion with angle; comparison of two different sizes (127 μm & 9 μm) of silicon carbide grit, eroding pure aluminium at 156 ms^{-1}.
(Sheldon & Finnie 1966a)

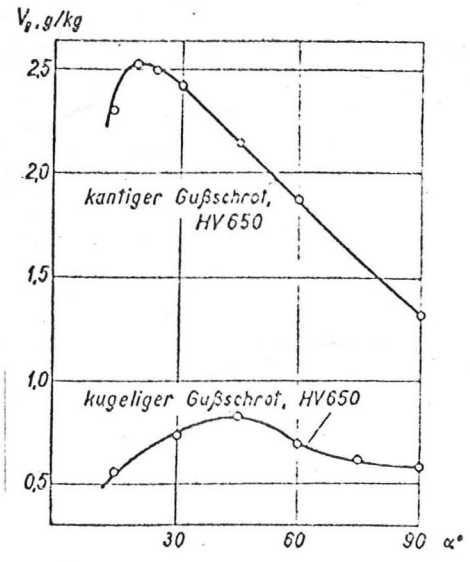

Figure 1.7
The variation of erosion of mild steel with angle; angular iron shot (upper curve) compared with round iron shot (lower curve) at the same impact velocity (120 ms^{-1})
(Kleis 1969)

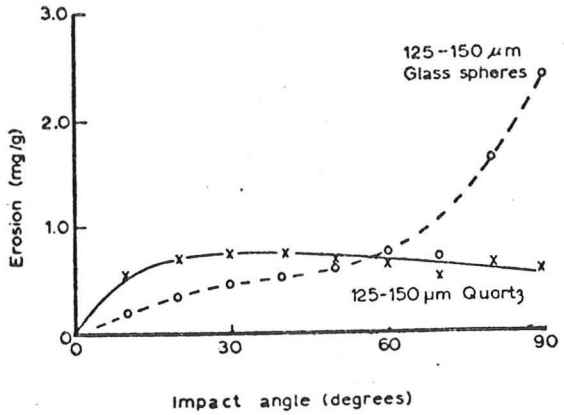

Figure 1.8
Dependence of the erosion of an aluminium alloy on impact angle for two different types of particle (angular quartz and spherical glass); velocity 250 ms^{-1}.
(Tilly & Sage 1970)

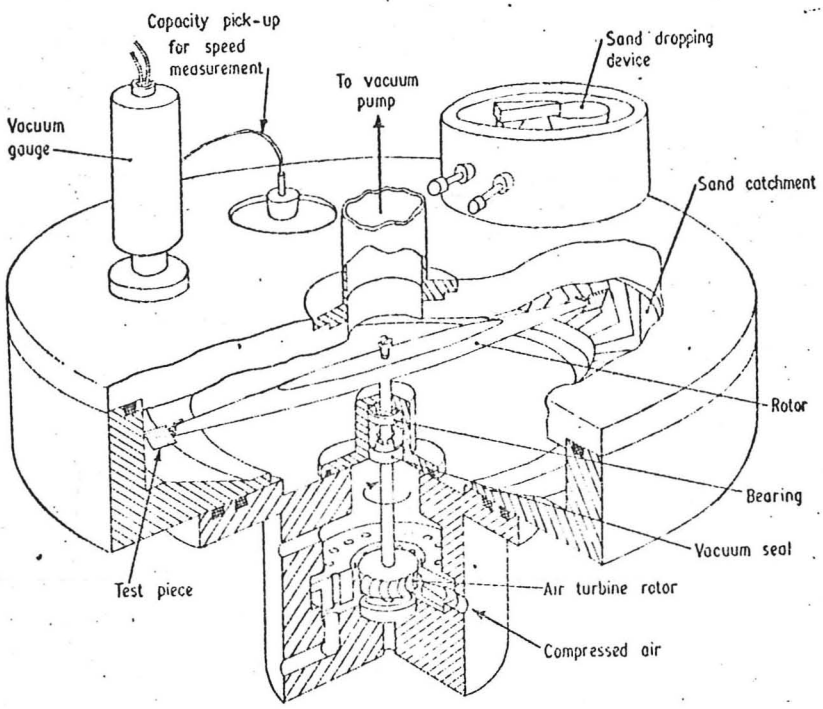

Figure 1.9
The whirling arm test rig used at the National Gas Turbine Establishment.
(Goodwin, Sage & Tilly 1969)

seems to affect erosion, and this may be directly related to the shape of the particles. Kleis (1969), however, has eroded mild steel with angular and spherical iron shot, which do not break up on impact. Figure 1.7 shows his results - the angular particles cause appreciably more erosion than the spherical, and the angle of maximum erosion is rather lower with angular particles than with round shot.

As mentioned above, erosive particles are nearly always harder than the material which they erode; should they be softer, the erosion decreases considerably, but not always to zero (Kleis 1967). The material of the abrasive particle can therefore affect its eroding power in this way.

A rather more important effect is that of particle fragmentation. Figure 1.8 shows the variation with impact angle of the erosion of an aluminium alloy by particles of different fragility. The relatively strong quartz particles give a characteristic ductile erosion curve, whereas glass beads, which fracture readily on impact, cause very much more erosion at normal incidence and result in a curve of different shape. Tilly's (1973) theory of erosion which takes into account the effects of fragmentation will be discussed later.

1.2.6 Tensile stress

Since the rotating blades of turbines are under considerable centrifugal stress, it is of interest to discover whether tensile stress in the specimen might affect its rate of erosion. Tilly (1969a) investigated this possibility and found a slight but significant decrease in erosion with increasing tensile stress. Smeltzer et al (1970) found an increase in erosion with increasing tensile stress, but again the effect was small and not considered worthy of further investigation.

1.2.7 Temperature

The effect of testpiece temperature upon the rate of erosion also appears small, but consistent results have been reported. Tilly (1969a) has found that the effect of increasing the temperature of a variety of alloys is to decrease the rate of erosion. Confirmatory results have

been obtained by Fehndrich (1969), Raask (1969) and Wood (1966). A corresponding increase in erosion at low temperatures has been observed by Lepikson and Siimpoeg (1969) who found that cooling mild steel from room temperature to 120K increased its erosion rate significantly.

1.2.8 Particle concentration

Kleis (1969) and Wood (1966) have noted a decrease in erosion with increasing particle flux; the impingement rates at which this becomes noticeable are high (200 $kgm^{-2}s^{-1}$) but there are obvious implications of this result in the design of accelerated erosion tests.

1.2.9 Chemical effects - erosion/corrosion

Many practical cases of dust erosion take place in highly corrosive environments; in such cases it is difficult to separate the effects of erosion from those of corrosion, and the two processes may well occur cooperatively. For example, Kleis (1969) has shown that quartz with 1% moisture content can cause double the erosion caused by dry quartz; whether this effect is physical or truly chemical is not clear. 0.5% sulphur dioxide in dry nitrogen increases the rate of erosion of mild steel to six times that in pure nitrogen (Muravkin and Riabchenko 1960). The majority of erosion tests have been conducted in air or vacuum (10^{-3}torr), and good correlation is found between the results obtained in the two environments, suggesting that surface oxidation is not important in such tests.

1.2.10 Testpiece material

Many investigations have been aimed at discovering how the resistance of a material to erosion depends upon other, more readily accessible, properties. The numerous results obtained with ductile metals confirm the early work reviewed by Wahl and Hartstein (1946). The commonest structural material used in erosive environments is steel, and little improvement can be made in the erosion resistance

of steels either by heat treatment (Finnie, Wolak and Kabil 1967) or by alloying (Tilly 1969a). Other alloys and pure metals have been tested and attempts made to correlate their erosion resistance with other properties. These will be discussed in section 1.5.

1.2.11 Single impacts

The processes occurring in a single impact have been studied by very few workers. Several scanning electron micrographs have been published of the surface damage caused by single erosive particles (Smeltzer et al. 1970, Jones and Gardos 1971 and Tilly 1973). Sheldon and Kanhere (1972) have made the only quantitative comparison between the weight losses resulting from single impacts and those found in erosion experiments using many particles.

1.3 Experimental techniques

In comparing the results of erosion experiments it is important to realise the limitations of the testing techniques used. Two types of equipment are in common use, the air-blast device and the whirling arm rig.

In the first apparatus, the erosive particles are entrained in a fast-flowing gas stream which accelerates them down a tube. The velocity with which they leave the tube depends upon a number of variables, and careful attention must be paid to these if a reasonably uniform particle velocity is required. Since, as we have seen, the erosion of all materials varies more rapidly than the square of the particle velocity, it is especially desirable to hold this velocity constant. A theoretical treatment of the air-blast rig has been given by Smeltzer et al. (1970) which shows that long ($\sim$3m) acceleration tubes are needed to ensure that the larger particles reach the gas flow velocity; a similar point was made by Finnie (1960). Such long tubes have not been used by many workers, most relying upon photographic measurement of particle velocities to ensure that the particles reaching the target are reasonably monoenergetic. Another disadvantage of this technique is that the actual angle at which the particles strike the surface is somewhat

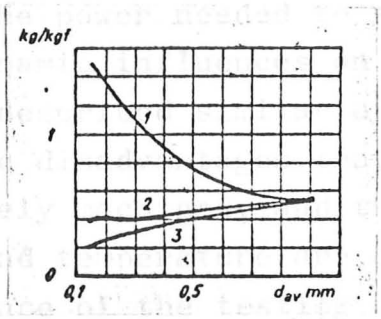

Figure 1.10
The effect of the test conditions on erosion rates. Erosion (ordinate) plotted against particle diameter (abscissa) for quartz sand on steel at an angle of 38° using the following test equipment:

(1) an air blast rig with a constant pressure of 300 kPa
(2) a vacuum whirling arm rig - impact speed 81 ms^{-1}
(3) a centrifugal accelerator - nominal impact speed 81 ms^{-1}

(Kleis & Uuemyis 1971)

uncertain. The gas flow over the target may deflect the smaller particles, and some may not strike the surface at all (Tilly 1969a).

The whirling arm rig, being rather more complex, is used by fewer workers, but seems to be the only apparatus capable of producing definitive results. Figure 1.9 shows such a rig; the two specimens are attached to the ends of a rotating arm in an evacuated (10^{-3} torr) chamber. Erosive particles are dropped into the path of the specimens at a controlled rate; the specimens are of sufficient depth to ensure that all the dust particles are struck. The impact velocity is closely defined, since the rotor speed may be precisely controlled and the variation of impact velocity across the specimen face is typically less than 1½%. Evacuation of the test chamber reduces the power needed to spin the rotor, and eliminates aerodynamic influences on the angle of impact. Kleis (1969) has described similar apparatus. Whirling arm rigs have the disadvantages that specimens must be small and accurately machined, and that the effects of specimen stress and temperature are not easily investigated.

The influence of the testing apparatus upon the results obtained is illustrated in figure 1.10; the apparent dependence of erosion rate upon particle size is shown for three different types of test apparatus. Curve 1 was obtained with a pneumatic blast rig in which the air pressure was held constant and the particle size changed. Since the smaller particles achieved higher velocities than the larger, it appears that they are considerably more erosive. Curve 3 was obtained with a centrifugal accelerator, as described by Kleis (1969). In this apparatus a stream of particles falls onto the centre of a rotating horizontal disc with radial grooves. The particles are accelerated down the grooves; although their tangential velocity when they leave the disc is constant, the radial component depends upon the frictional resistance they experience while sliding down the groove. It is seen that this curve lies below what must be regarded as the "true" curve (number 2) obtained with a vacuum whirling arm rig. In any critical appraisal of the results of erosion experiments it is therefore essential

to know how they were obtained, and to know the spread of velocity among the particles striking the testpiece.

1.4 Theoretical treatments of ductile erosion

1.4.1 Aims of theoretical treatments

Several theoretical approaches to the problem of ductile erosion have been made in the last twenty years. The purpose of such a treatment is to predict the erosion rate in any situation from a knowledge of such variables as particle size, shape, material and velocity, the angle of impact and the surface material. Ideally, a theory should also be able to predict the resistance to erosion of different metals from a knowledge of their other, more readily measureable, properties.

Many of the theories seek only to fit the empirical data into a coherent pattern, without reference to the physical mechanisms underlying the erosion process. The more valuable approach is to base the theory upon a physical model, preferably with some experimental justification, but such attempts have led to oversimplification of the problem. A brief survey of the theories will be presented here, together with a discussion of their validity in the light of experimental evidence.

1.4.2 Finnie (1958 and 1960)

Finnie's approach is essentially mechanical; he considers that abrasive grains will cut into the surface on impact and remove metal by a "cutting or displacing" action. Figure 1.11 illustrates this approach. Finnie acknowledges that the mechanism will only operate at low impingement angles, but emphasises that these are important since for ductile metals the angle of maximum erosion is around 20^{o}. He solves the equations of motion of the particle making the following assumptions:

(i) that the ratio of vertical force component to horizontal force component is a constant (K).

(ii) that the length l over which the particle contacts the surface divided by the depth of cut Y_t (see figure 1.11a) is a constant (ψ)

(iii) that the cutting face of the particles is of constant

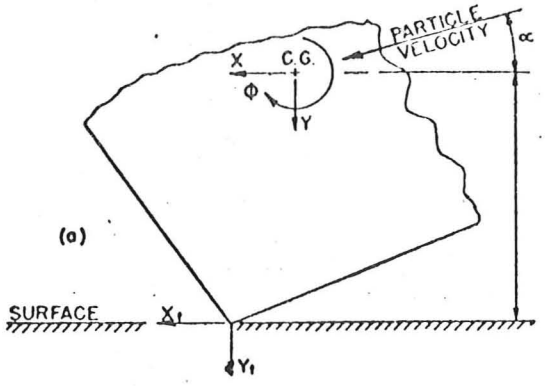

IDEALIZED PICTURE OF AN ABRASIVE GRAIN STRIKING A SURFACE.

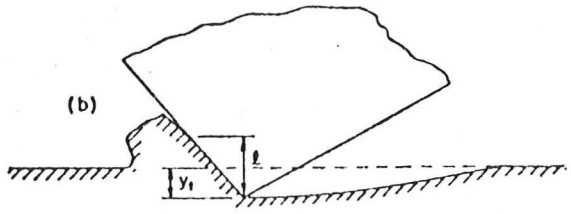

IDEALIZED PICTURE OF AN ABRASIVE GRAIN REMOVING MATERIAL.

Figure 1.11
Finnie's theoretical approach to erosion.
(Finnie 1958)

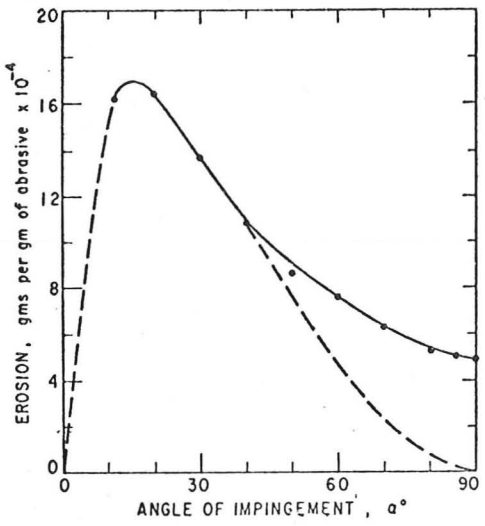

Figure 1.12
Predicted (dashed curve) and observed (solid curve) erosion of pure aluminium by 127 μm SiC particles at 156 ms^{-1}.
(Sheldon & Finnie 1966a)

width b .

(iv) that a constant plastic flow stress p is reached immediately upon impact (ignoring elastic stresses).

To estimate the volume of material removed, he assumes that this will be equal to the volume swept out by the tip of the particle, the cutting process being terminated either when

(i) the horizontal velocity of the particle tip becomes zero ($\dot{x}_t=0$) or

(ii) the particle leaves the surface (y=0).

The final equations governing weight loss are :

$$W=\frac{n}{p\psi}.\frac{mv^2}{K}\left[\sin 2\alpha - \frac{6}{K}\sin^2\alpha\right] \qquad (1.1)$$

for $\tan\alpha \leqslant K/6$

and $$W=\frac{n}{p\psi}.\frac{mv^2}{K}.\frac{K\cos^2\alpha}{6} \qquad (1.2)$$

for $\tan\alpha \geqslant K/6$.

Here n is the density of the metal being eroded and W is the total weight eroded by a mass m of abrasive grains, the assumption being made that all grains will remove the same amount of material. The angle for maximum erosion is given by $\tan 2\alpha_{max} = K/3$.

Finnie (1958) performed scratching tests to estimate the value of K, and from these, and by analogy with the process of grinding, suggests a value of $K = 2$ .The angle of maximum erosion is therefore predicted to be $\sim 17^o$ and equations 1.1 and 1.2 become

$$W = \frac{n}{p\psi}.\frac{mv^2}{2}\left(\sin 2\alpha - 3\sin^2\alpha\right) \quad \alpha \leqslant 18.5^o \qquad (1.3)$$

and $$W = \frac{n}{p\psi}.\frac{mv^2}{6}\cos^2\alpha \quad \alpha \geqslant 18.5^o \qquad (1.4)$$

Figure 1.12 shows experimental results for the erosion of pure aluminium by silicon carbide grains (solid line) and the predictions of Finnie's theory (dotted line). The value of $p\psi$ has been selected to give the best fit ; it is seen that the theory underestimates the erosion at

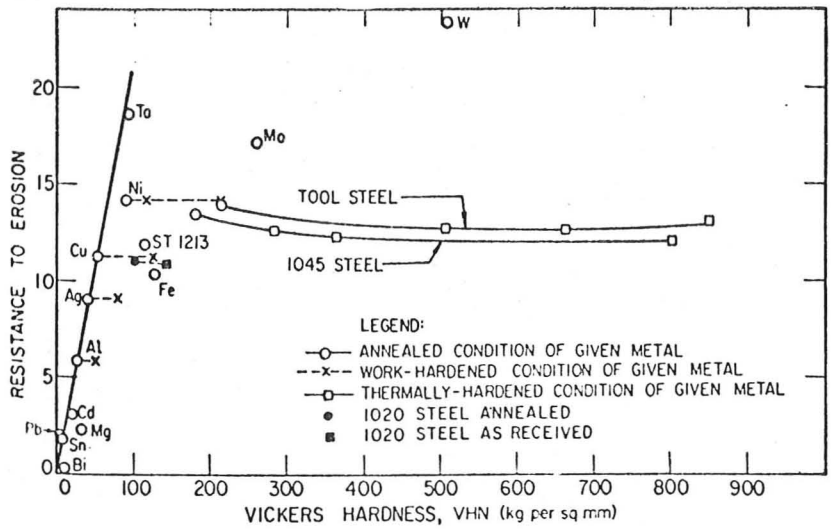

Figure 1.13
Resistance to erosion (grams of eroding particles per mm^3 removed) as a function of indentation hardness for erosion by 250 μm SiC particles at 20^o and 78 ms^{-1}. (Finnie, Wolak & Kabil 1967)

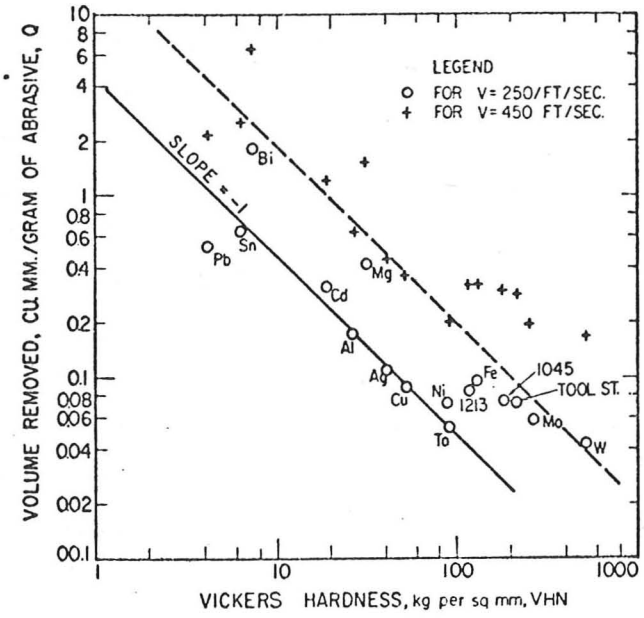

Figure 1.14
Volume removed (mm^3 per gram of 250 μm SiC particles) as a function of indentation hardness for metals eroded at 20^o and 78 ms^{-1} (250 ft/s), and 140 ms^{-1} (450 ft/s). (Finnie, Wolak & Kabil 1967)

high angles, predicting no erosion at 90°. An empirical correction may be introduced to bring the curves into coincidence, but there seems little physical justification for it (Finnie 1958).

The theory predicts that if the deformation process is similar in all metals, the volume eroded, at any rate near 18° impingement angle, will be inversely proportional to p, a plastic flow stress. Finnie, Wolak and Kabil (1967) compared the predictions of this theory with experimentally determined erosion rate, assuming that p will be proportional to the Vickers hardness of the metal. Figures 1.13 and 1.14 show their results, plotted on linear and logarithmic scales. While the metals Ag, Al, Sn, Cu and Ta lie close to the straight line, the other metals tested, and notably the steels of varying temper, lie some way from it. Tilly (1969) has found even less correspondence between the hardness of various alloys and their rates of erosion.

1.4.3 Bitter (1963)

Bitter accounts for the erosion at normal impact by splitting the wear into two components. That which predominates at low impact angles he terms 'cutting wear', while at high angles 'deformation wear' predominates. The phenomenon of brittle erosion differs from that of ductile only by the fact that in brittle materials no cutting wear occurs.

Bitter (1963a) develops his expression for the deformation wear term by considering the energy dissipated in plastic deformation of the material, calculated assuming an elastic-plastic normal impact. Since in an ideally brittle material, plastic flow does not occur, this approach is somewhat surprising. He finds that the energy loss is given by

$$\tfrac{1}{2} m (v-K)^2$$

where m is the total mass of the impinging particles, and v is their velocity. K is the velocity of impact at which plastic deformation first occurs.

He then replaces v by $v \sin\alpha$ to allow for impacts not at 90°, and assumes that an energy ε is needed to remove unit mass of material from the surface by this mechanism. For deformation wear, then,

$$W_d = \frac{\frac{1}{2}m\ (v\sin\alpha - K)^2}{\varepsilon} \qquad (1.5)$$

where W_d is the weight loss due to this type of wear.

His calculation of the "cutting wear" term (Bitter 1963b) is based on a similar specific energy approach, an energy ε being needed to displace unit mass from the surface. The two cases are considered, as by Finnie, of the particle leaving the surface while still moving horizontally, and of it stopping cutting while still in contact. To calculate the energy lost by the particle which will result in cutting wear, Bitter considers the particle to be spherical, of radius equal to the radius of the corner of the real particle, and yet of the same mass as the real particle. He then applies the elastic-plastic collision formulae of Andrews (1930), assuming a constant plastic flow stress, and derives the expressions :

$$W_c = \frac{2mC\ (v\sin\alpha - K)^2}{\sqrt{v\sin\alpha}} \cdot \left(v\cos\alpha - \frac{C(v\sin\alpha - K)^2}{\sqrt{v\sin\alpha}} \cdot \varepsilon\right) \qquad (1.6)$$

and

$$W_c = \frac{\frac{1}{2}m}{\varepsilon} \cdot \left(v^2\cos^2\alpha - K'(v\sin\alpha - K)^{\frac{3}{2}}\right) \qquad (1.7)$$

Equation 1.6 is valid when the particle rebounds while still cutting and equation 1.7 where it stops cutting during the impact.

At sufficiently high velocities, the elastic deformation may be neglected, and K and K' put equal to zero. C is given by

$$C = \frac{0.29}{y}\sqrt[4]{\frac{n}{y}}$$

where n is the density of the target material and y is its plastic flow stress. The total weight loss is then equal to $W_d + W_c$; the material is characterised by ε, ε, and C. For ductile metals, Bitter suggests that equation 1.7 will apply at impact angles greater than 15°; the sum of the two erosion terms is then :

$$W = \frac{\frac{1}{2}mv^2\sin^2\alpha}{\varepsilon} + \frac{\frac{1}{2}mv^2\cos^2\alpha}{\varepsilon} \qquad (1.8)$$

Since this equation contains two parameters, ϵ and ϱ, which cannot be expressed in terms of other material properties and must therefore be experimentally determined, this equation may be adjusted to fit experimental results well. Bitter (1963b), Head, Pacala and Poole (1967), Neilson and Gilchrist (1968a) and Kleis (1969) have all attempted to analyse erosion data using these equations. All find that the values of ϵ and ϱ needed to fit the experimental data depend not only upon the surface material, but also upon impact angle, velocity, particle size, shape and composition. Wood (1966) made a similar assessment of the erosion behaviour of several metals, attempting to correlate ϵ and ϱ with bulk properties of the metals such as hardness and strain energy to fracture. He was able to find no systematic correlation.

1.4.4 Thermomechanical approaches

The analyses of Smeltzer et al. (1970) and Ascarelli (1971) are based upon the premise that very high temperatures are developed under an impacting particle, and that the material is removed as a result of melting.

Smeltzer proposes two mechanisms by which the molten material is removed. In the first, droplets of metal are "splattered" out of the crater, while in the second they adhere to the particle, which is then dislodged by a subsequent impact. Their analysis will not be discussed in detail; the final equation contains a term for each mechanism and expresses the weight loss as:

$$W = A(\tfrac{1}{2}mv^2)(\sin\alpha - \sin^2\alpha) + B(\tfrac{1}{2}mv^2)\sin^2\alpha \qquad (1.9)$$

where A and B are constants.
This equation is essentially the same as Bitter's result (1.8); the functions of α are not the same as his, but clearly by selection of suitable values for A and B, a reasonable agreement may be obtained with experimental results. Predictably, Smeltzer found that A and B varied with velocity and particle type, and could find no correlation with elastic modulus, melting point,

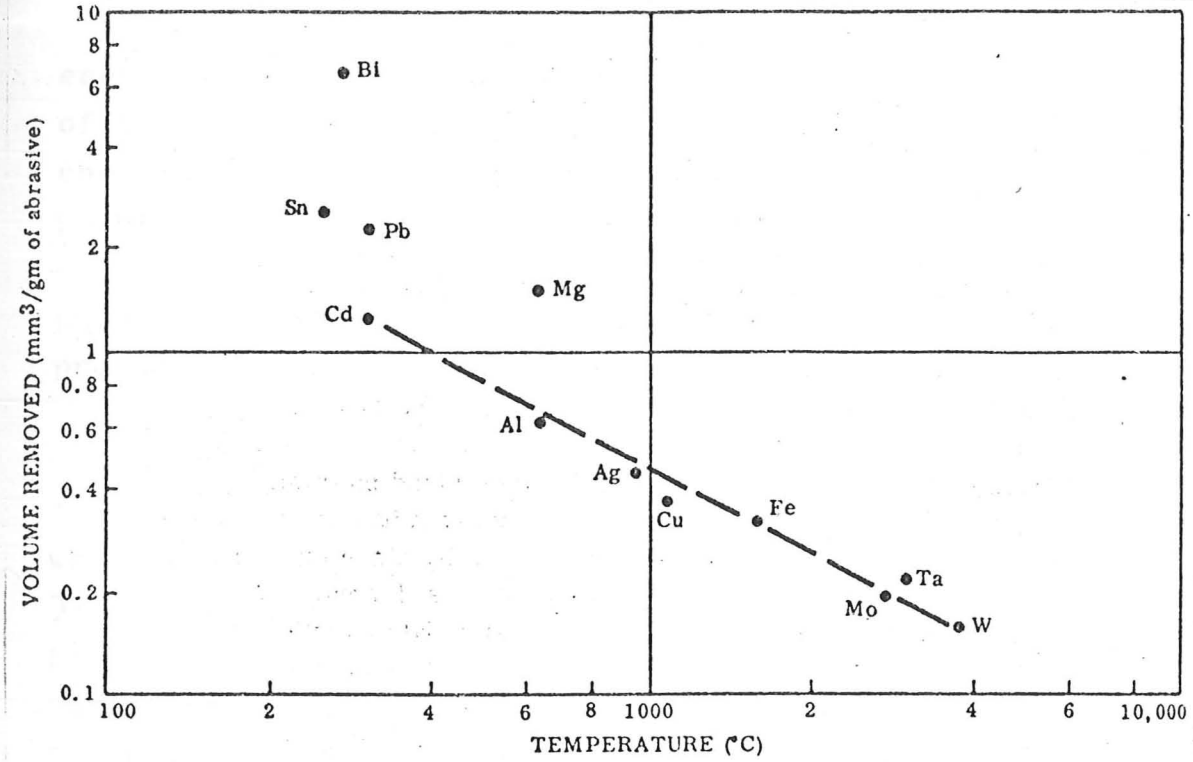

Figure 1.15
Erosion (mm^3 per gram of eroding particles) plotted against melting point (degrees C) for pure metals. Data on erosion taken from Finnie, Wolak & Kabil(1967) - silicon carbide grains at 20^o impact angle and 140 ms^{-1}.
(Smeltzer et al. 1970)

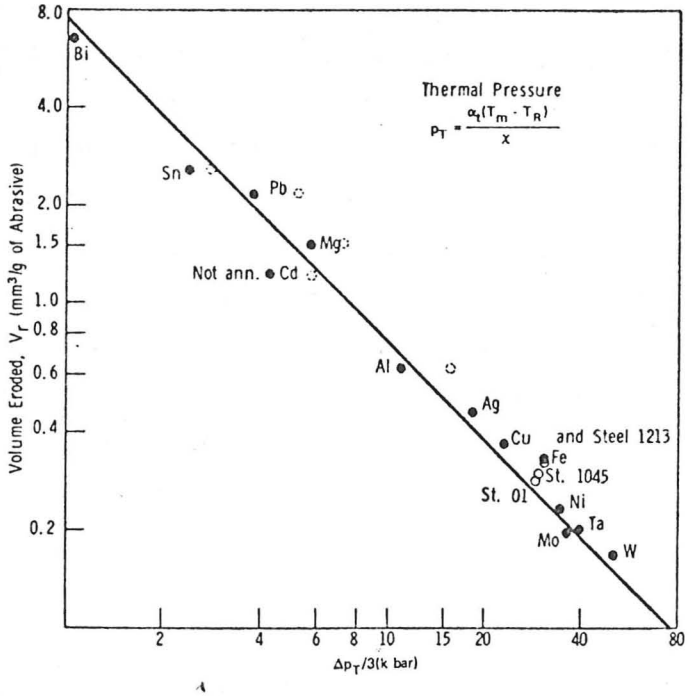

Figure 1.16
Volume eroded (from Finnie, Wolak & Kabil 1967) plotted against P_t, Ascarelli's thermal pressure parameter, for pure metals and some steels.
(Ascarelli 1971)

energy required to melt unit mass or surface tension of the liquid metal. He has, however, pointed out a correlation between erosion resistance and melting point for pure metals (see figure 1.15).

Ascarelli envisages some form of melting phenomenon, the erosion of a metal being inversely proportional to its "thermal pressure", P_t given by

$$P_t = \frac{3\alpha}{\chi} \quad (T_m - T_r) \qquad (1.10)$$

where α is the coefficient of linear thermal expansion, χ is the isothermal compressibility, T_m is the melting point of the metal and T_r is room temperature. The agreement between P_t and the erosion rates experimentally determined by Finnie, Wolak and Kabil (1967) is remarkably good ($\sim$25%) for all the metals tested by them. Figure 1.16 shows the correlation; the values of α and χ used to calculate P_t are room temperature values.

1.4.5 Sheldon and Kanhere (1972)

Sheldon and Kanhere describe a model for erosion by spherical particles. They calculate the depth of the plastic indentation made in a perfectly plastic material by a normally impacting sphere. This problem has been discussed by Tabor (1951); it was found empirically by Martel in 1895 that the volume of such an indentation is proportional to the kinetic energy of the sphere. Sheldon and Kanhere, however, erroneously state that the volume of the indentation is proportional to the cube of its depth, and so deduce that the volume removed by the impact, which they state "is nearly the full crater size" is directly proportional to the cube of the impact velocity, and inversely to the $^3/_2$ power of the hardness of the metal.

1.4.6 Tilly (1973)

This theory is the only one to allow for the effects of particle fragmentation. Erosion is considered to be a two component process. Primary erosion is a result of the impact of particles before fragmentation; equation 1.11, which expresses it, incorporates a

threshold size and velocity below which no erosion occurs :

$$E_1 = \frac{v^2}{\phi} \left(1 - \left(\frac{d_o}{d}\right)^{\frac{3}{2}} \cdot \frac{v_o}{v}\right)^2 \qquad (1.11)$$

ϕ is a specific energy, and d_o and v_o are the diameter and velocity of particles at the threshold conditions, which are determined experimentally.

The secondary damage, which results from fragmentation of the particles, causes erosion given by :

$$E_2 = \frac{v^2}{\psi} \cdot F$$

where ψ is a specific energy and F is the degree of fragmentation of the particles. If all the particles are broken then F = 1.

The total erosion is given by the sum of the two terms. Although the parameters d_o, v_o and F may be determined experimentally, the two specific energy terms ϕ and ψ are left for 'curve-fitting'; these have not been related to any material properties, and the variation of erosion with angle can only be argued qualitatively from this theory.

1.4.7 Empirical approaches

Purely empirical approaches have been taken by Brauer and Kriegel (1965), Raask (1969) and Head and Harr (1970).

Brauer and Kriegel examined the wear of bends in pipes carrying abrasive particles; they considered both brittle and ductile materials and found that their results could be correlated with the Young's modulus of the material (figure 1.17). The ductile metals, however, lie on a very small portion of the curve, and the test conditions were not simply analysed, rendering this finding of little practical use.

Raask wished to predict the life of mild steel boiler tubes in an erosive ash stream. He expressed his results in the form of an empirical equation which, over the limited range for which it was intended, enabled him to forecast erosion wear with sufficient accuracy.

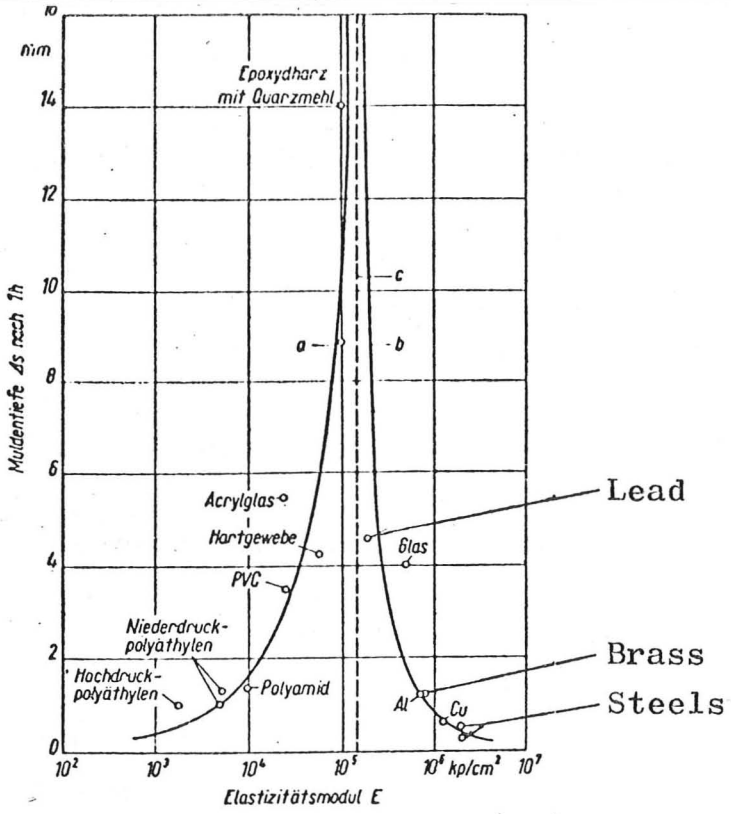

Figure 1.17
Depth of erosion pit (mm) after one hour in an air-blast rig, plotted against Young's modulus E.
(Brauer & Kriegel 1965)

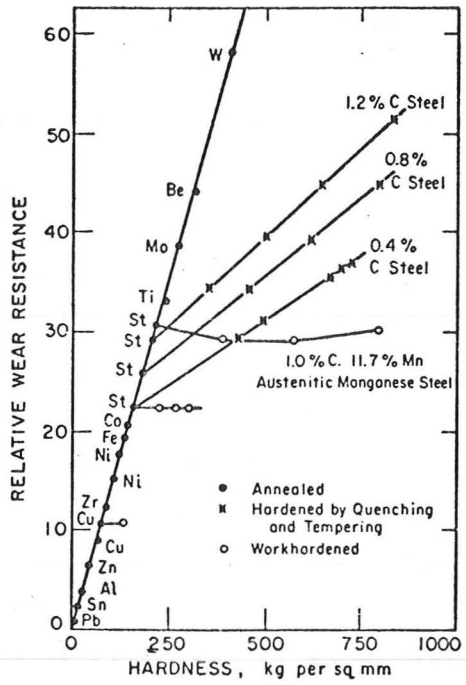

Figure 1.18
Relative wear resistance as a function of indentation hardness for metals rubbed against abrasive paper.
(Krushchov & Babichev 1956)

Head and Harr attempted a dimensional analysis of the problem, and then constructed an empirical model from their experimental data, using regression techniques to obtain the best fit. Their final model presents the erosion rate as a function of particle velocity, particle shape factor, impact angle, hardness of the particles, hardness of the target and "erosion resistance" of the target. This last is simply an energy per unit volume which should in theory be characteristic of the metal. Their equation contains eleven terms and gives a "very good fit" to the data. However, its ability to predict erosion under untried conditions is very limited, and Head, Lineback and Manning (1973) have modified it considerably with the aim of widening its usefulness, and have introduced another empirically determined variable.

1.5 Discussion

The qualitative features of ductile erosion have been well established, but none of the present theories can explain more than a few of the observed phenomena. The velocity exponent, for example, is certainly not 2, but in most cases nearer 2.4, yet all the theoretical treatments, except Tilly's, predict a variation of erosion with the square of the velocity. For large particles, Tilly also predicts this dependence. Clearly the underlying assumption that the weight loss will be proportional to the kinetic energy of the incident particles must be at fault; any approach which makes this hypothesis must fail in its prediction of the velocity exponent.

Similarly, attempts to correlate erosion resistance with a single material property have failed. Finnie predicts a dependence on some plastic flow stress, but the agreement found between this theoretical stress and observed indentation hardness is poor. Other attempts to compare erosion resistance with strain energy to fracture, elastic modulus and melting point have produced similar conclusions. The inefficiency of indentation hardness as an indication of erosion resistance is particularly frustrating, since it correlates well with abrasive wear, a process which intuitively might be

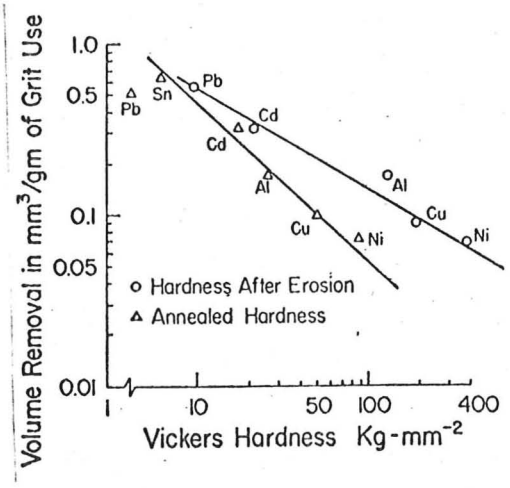

Figure 1.19
Volume eroded (mm^3 per gram of abrasive) plotted against indentation hardness for various metals. Note that the slope of -1 (implying inverse proportionality) is only found when the hardness of the annealed metal is considered. (Sheldon 1970b)

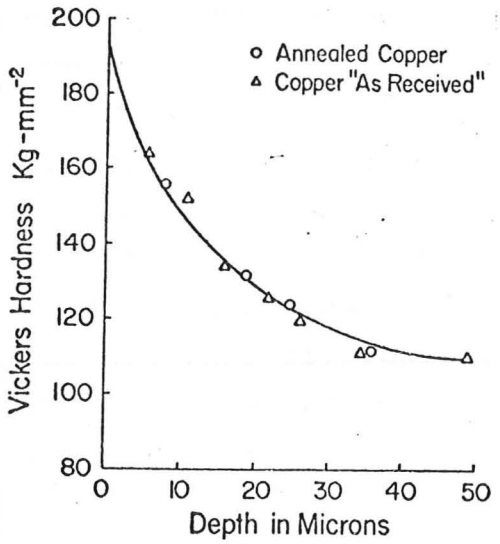

Figure 1.20
Indentation hardness plotted against depth below the surface of eroded specimens of copper. Note that annealed and work-hardened specimens give the same curve; the surface is clearly heavily work-hardened after erosion. (Sheldon 1970b)

thought similar to erosion. Figure 1.18 shows the results of Krushchov and Babichev (1956) who measured the wear rate of metals rubbed on abrasive paper. These results have been confirmed by later work (for a review of abrasive wear see Moore 1974). All the pure metals lie on a straight line, and heat treatment of carbon steels does increase their wear resistance, in contrast to the results of the erosion tests shown in figures 1.13 and 1.14.

It is noteworthy that those metals which do show a proportionality between erosion resistance and hardness in figure 1.13 only do so if the hardness of the annealed metal is considered (Sheldon 1970b). Figure 1.19 shows these results plotted against the hardness of fully work-hardened (after erosion) and annealed specimens; the straight line of slope -1 which shows the inverse proportionality fits only the annealed hardness values. This result is surprising, since surfaces are highly strain-hardened by erosion; Wellinger (1949) has shown plots of microhardness against depth below eroded surfaces, and a similar graph from Sheldon (1970b) is shown in figure 1.20. Previous work-hardening of the material has no effect upon erosion rates. (Finnie, Wolak and Kabil 1967)

The success of Ascarelli's "thermal pressure" as an indicator of erosion behaviour is surprising; the physical basis for his assumptions is weak, but the correlation over the complete range of metals tested suggests that the agreement may be more than fortuitous. It is, however, difficult to see how his calculation of "thermal pressure" which ignores the variation of thermal expansion coefficient and bulk modulus with temperature can predict erosion resistance, especially since the observed variation of erosion with temperature is of the opposite sign to that predicted. More experimental data on the erosion of pure metals is needed to test this theory.

The mechanism by which metal becomes detached from a surface by an impacting particle is far from clear. Conflicting evidence has been presented. Finnie (1958) suggests that metal is removed by the cutting or displacing action of the particle, and Tilly has shown photographic evidence of a metal chip partly removed by a glancing

UNIVERSITY LIBRARY CAMBRIDGE

impact which would appear to confirm this model. Smeltzer (1970), however, in a detailed SEM study of eroded surfaces, could find no evidence of micromachining and observed no traces of intact chips in the eroded debris; he felt that his observations supported a "localised melting" process.

Since simple energy-based theoretical approaches to the problem of erosion appear to be very limited in usefulness, more information is clearly needed on how metal is removed by an impacting particle. Only when an experimentally verified physical model has been developed can the process be analysed mathematically. It was to investigate the physical processes occurring in ductile erosion that this work was carried out.

Chapter Two

Introduction to this work

2.1 Introduction

We have seen in chapter 1 that no real understanding exists of the mechanisms by which erosive particles remove metal when they strike a surface. The first stage in formulating any theory of erosion is clearly to identify the important physical processes involved; the theories so far developed are not based on physical models for which there is good experimental evidence.

It is felt that the process of erosion must be stochastic in nature; irregular particles will strike the surface with random orientations, and it is quite possible that a large number of slightly differing mechanisms may in practice operate. However, it is argued that only a few fundamentally different processes can be important; it is essential before formulating any theory of erosion that these mechanisms be identified. Several possible mechanisms have been suggested in the numerous theories discussed in chapter 1; a consideration of the processes of machining and grinding suggests another.

2.2 Metal removal in machining and grinding

In the conventional machining of ductile metals with a single-point tool, two types of deformation may be distinguished: cutting and ploughing. Figure 2.1 shows the distinction between them; in cutting (a), a chip of metal flows continuously up the rake face of the tool, whereas in ploughing (b), the metal in front of the tool piles up and may even flow down the rake face. The incidence of ploughing and cutting is related to the rake angle of the tool face; the definition of rake angle is illustrated in the figure. For tool rake angles greater than a critical angle, cutting deformation occurs, while more negative rake angles result in ploughing. A typical value for this critical angle in orthogonal cutting is

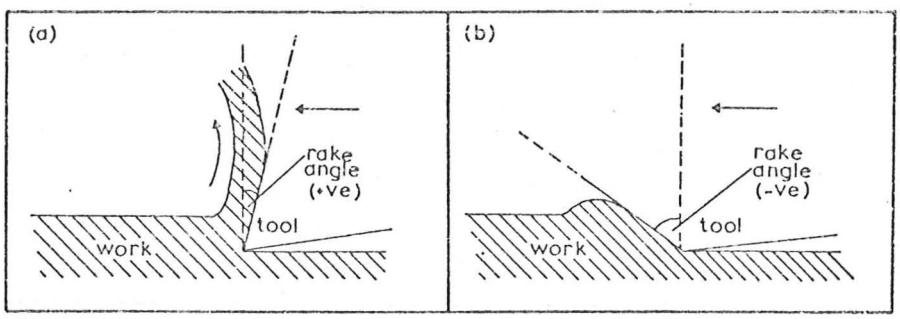

Figure 2.1
Geometry of the machining process (orthogonal).
(a) positive rake angle
(b) negative rake angle.

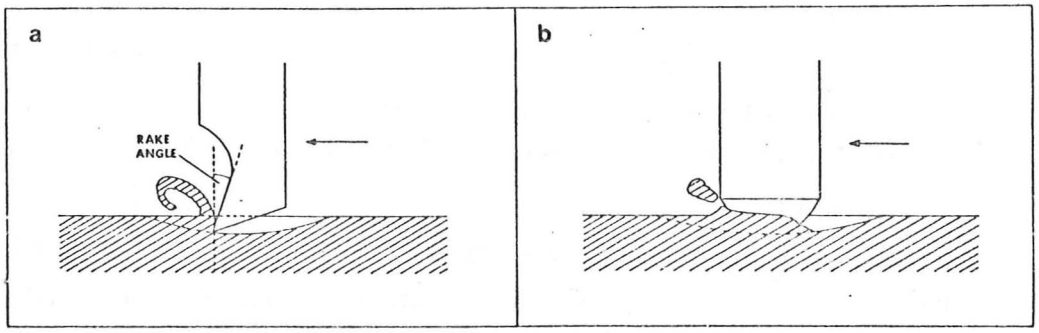

Figure 2.2
Influence of rake angle in Graham & Baul's grinding experiments.
(a) positive rake angle - cutting deformation
(b) large negative rake angle - ploughing deformation.
(redrawn from Graham & Baul 1972)

-60^{o} (Rubenstein, Groszman and Koenigsberger 1966)

While machining is seldom carried out with rake angles low enough to cause ploughing, there is little control over the orientation of grit in a grinding wheel or on abrasive paper, and a number of such particles will plough rather than cut. Mulhearn and Samuels (1962) found that for the small grit particles on abrasive paper the critical rake angle was 0 ± 2^{o}; in other words, all particles with negative rake angles deformed the metal by ploughing, while those with positive rake angles removed continuous chips of metal by cutting. Having made a statistical survey of the rake angles presented by the grits on a piece of abrasive paper, they could plot a rake angle distribution curve, and estimated that only one sixth (typically) of the particles would remove metal by cutting, the remaining five sixths deforming the surface by ploughing.

Although Mulhearn and Samuels assumed that the majority of grit particles, which caused ploughing deformation, would not remove metal, the work of Graham and Baul (1972) shows that in the process of grinding, ploughing deformation can lead to removal of material. The grinding process differs from that of abrasive rubbing in that the grit is constrained to move in a circular arc through the workpiece. A single-point tool at the end of a swinging arm was used to study the process; figure 2.2 shows tools midway through the arc of swing. The positive rake angle tool in (a) cuts a conventional chip, whereas the spherically-tipped tool in (b), which has a large negative rake angle, removes metal by a different mechansism associated with ploughing. The critical rake angle in this study was found to be $\sim -55^{o}$.

2.3 Rake angles in erosive particle impacts.

We have seen that erosive particles are harder than the metal which they erode, and that the impact angle at which most erosion occurs is $\sim 20^{o}$. The length/depth ratio of typical single impact scars formed at this angle is $\sim$10:1 (Finnie 1958). The impact geometry will therefore by similar to that occurring in grinding, and

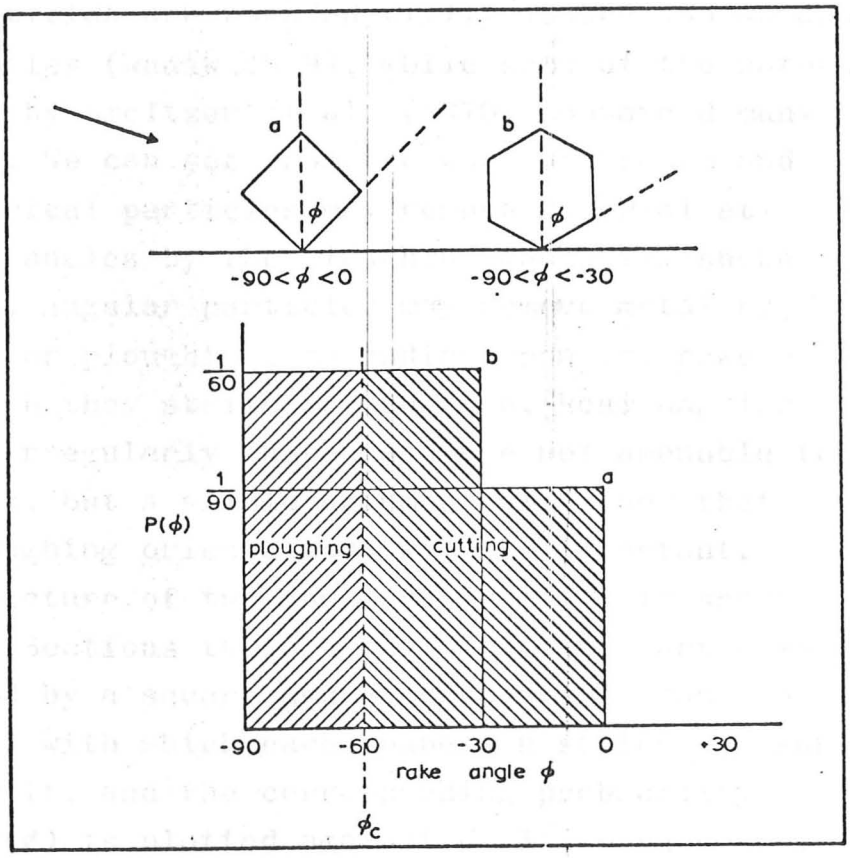

Figure 2.3

The way in which the probability of ploughing or cutting deformation depends on particle shape. A critical rake angle ϕ_c of -60^o has been assumed. For shallow impact angles the square particle (a) will plough in $\frac{1}{3}$ of its orientations and cut in $\frac{2}{3}$, while for the hexagonal particle (b) the probability is $\frac{1}{2}$ for each.

The probability of the rake angle lying between ϕ and $\phi + d\phi$ is $P(\phi).d\phi$; the function is normalised so that

$$\int_{-90^o}^{+90^o} P(\phi).d\phi = 1$$

we might expect that the deformation processes observed by Graham and Baul in grinding would also take place in erosion at shallow impact angles.

Dust particles may be broadly classified into rounded and angular shapes. Naturally occurring erosive dusts may be composed of particles of either shape; wind-blown sand particles are rounded (Tilly 1969b) and so are coal ash particles (Raask 1969), while some of the natural soils examined by Smeltzer et al. (1970) contained many angular grains. We can see from the work of Graham and Baul that spherical particles may remove material at oblique impact angles by the ploughing mechanism shown in figure 2.2b. Angular particles may remove metal by either cutting or ploughing, depending upon the rake angle with which they strike the surface. Real angular particles are irregularly shaped and are not amenable to simple analysis, but a simple argument will show that impacts at ploughing orientations will be important. An idealised picture of two angular particles is shown in figure 2.3. Sections through the impacting particles are represented by a square and a hexagon. The range of rake angles (ϕ) with which each shape can strike the surface is shown below it, and the corresponding probability distribution $P(\phi)$ is plotted against ϕ. It is seen that if a critical rake angle (ϕ_c) of -60^o is assumed, then ploughing deformation will take place in one third of the impacts of the square-sectioned particle (a), and in one half of the impacts of the grain with a hexagonal section.

Particle fragmentation is an important feature of the impact of even quite strong particles (e.g. silicon carbide and diamond - Tilly 1973); in such cases, even for normal impact, ploughing deformation may again be important. The break-up of brittle spheres on normal impact produces fragments of the form shown in figure 2.4 (Arbiter, Harris and Stamboltzis 1969). Several oblique fracture planes (P) break the sphere into fragments which then move radially outwards from the impact site. Tilly and Sage (1970) found that in such an impact the radial flow velocity is comparable with the initial impact velocity; numerous radial scars on the surface result from this flow. It is apparent from figure 2.4 that these

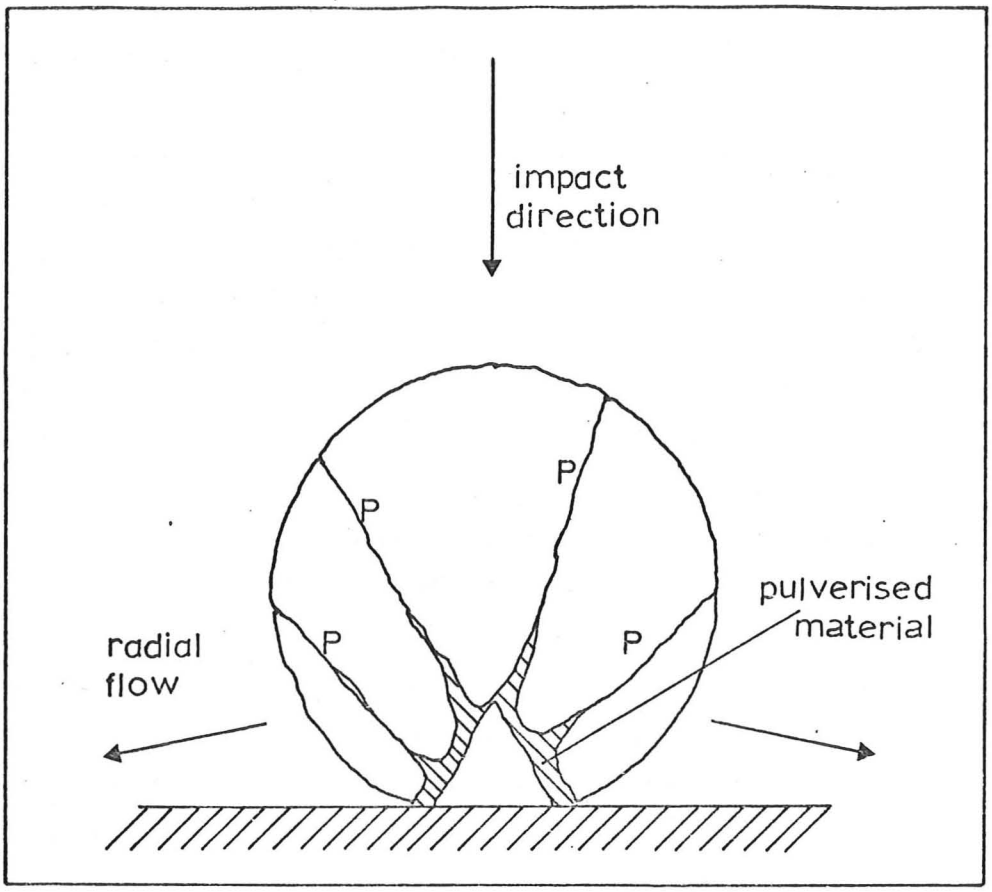

Figure 2.4
The fragmentation of a brittle sphere on normal impact (from Arbiter, Harris & Stamböltzis 1969)

fragments will all present negative rake angles to the metal surface, and many of them will cause ploughing deformation.

The possibility that ploughing deformation, of the type discussed, might be an important mechanism in the erosion of ductile metals has not been considered previously. Finnie's (1958) analysis assumes a mechanism of cutting or micromachining rather than ploughing, in which the volume of the chip cut from the crater is assumed to be equal to that swept out by the tip of the particle. This simple analysis overestimates erosion considerably, and Finnie (1960) had to introduce a correction factor to allow for the proportion of particles which do not cut in an idealised manner.

While the arguments above suggest that erosive particles may remove metal by ploughing, the forces acting on a freely-impacting grain are very different from those on a single-point tool constrained to deform the metal by an external machanism; it is not immediately apparent that such a particle can remove material by a ploughing action. Experimental investigation of the impact of single particles at ploughing rake angles was clearly needed.

2.4 Aims of this work

The work to be described had the main aims

(i) to assess the plausibility of the erosion mechanisms suggested by previous workers and

(ii) to investigate whether the process of ploughing, discussed above, might be an important mechanism in the erosion of ductile metals.

The experimental approach adopted was to study the impacts of single particles on a plane metal surface. It was considered that this would be of more value in identifying the processes of metal removal than the study of multiple impacts, which has already received much attention, or of single impacts on a previously eroded and roughened surface. Some means of producing impacts at controlled velocities and angles was needed. A technique of wide versatility was required; the ability to project comparatively large ($\sim$10mm) specimens at stationary particles was desired

for the study of angular particle impacts, while the facility to accelerate particles as small as ~50 μm would enable size effects to be studied. Explosive methods of acceleration were ruled out for reasons of convenience and safety; a compressed-gas gun was built which provided the desired facilities. The design and performance of this gun is described in the next chapter.

Chapter Three

The Gas Gun

3.1 Introduction

All single-stage gas guns consist of a reservoir, initially containing gas at a high pressure, separated by a valve from a barrel, containing the projectile at rest. The projectile is accelerated by the pressure difference across it once the valve is opened. The simplest theory of gun performance assumes a constant pressure difference across the projectile during its travel down the barrel; although it seriously overestimates the muzzle velocity of the projectile, this theory is worth considering in detail since it highlights the more important factors involved in the design of such a gun.

3.2 Constant pressure theory

We consider the one-dimensional motion of a projectile under the action of a constant driving pressure P. The projectile is a perfect frictionless fit in a cylindrical barrel of diameter d and length l. The equation of motion of the projectile is:

$$m\ddot{x} = \tfrac{1}{4}P\pi d^2$$

where m is the mass of the projectile. We assume that the projectile starts from rest at x = 0; then at the muzzle where x = l, $\dot{x}$ = v given by:

$$v = (\tfrac{1}{2}\pi d^2 l)^{\frac{1}{2}}(P/m)^{\frac{1}{2}}$$

So for any gun with l and d defined, the muzzle velocity will be proportional to $(P/m)^{\frac{1}{2}}$.

If we consider a cylindrical projectile of length 2d and density n, then $m = \tfrac{1}{2}\pi n d^3$ and

$$v = (lP/dn)^{\frac{1}{2}}$$

The muzzle velocity is therefore dependent on the ratio l/d which is a geometrical factor, and upon P/n. It is seen that geometrical scaling of such a gun will not change its muzzle velocity, provided that the projectile is similarly scaled.

The influence of some other factors may be inferred from their effect upon the assumption of constant driving pressure. For example, the volume of the reservoir, provided that it is large compared with the volume of the barrel, will have little effect on the muzzle velocity. At projectile velocities low compared with the sonic velocity of the driving gas, "relativistic" effects in the gas will be of little consequence, but at higher velocities these effects may become of major importance. The limiting velocity at which a pressure discontinuity can propagate down the barrel is the shock wave velocity corresponding to that pressure; clearly this theory predicts no such limit. Similarly, the opening time of the valve, and any resistance to gas flow which it may offer when open, will tend to invalidate the quasi-static assumption of constant driving pressure. Some idea of the limitations of this model may be gained from the results of Taylor and Davies (1942). They applied the constant pressure theory to a compressed air gun used at low velocities, and found a discrepancy of 10% between theory and practice for a velocity of 150ms^{-1}. We shall see later that at higher velocities the discrepancy is much greater.

3.3 Discussion of valve design

The most important single part of a gas gun is the valve which permits the reservoir gas to flow down the barrel. Ideally, such a valve should open instantaneously, offer no resistance to gas flow when open, yet provide a perfect seal when closed. Many different techniques have been used in the past; no single design of valve has a clear advantage over the others.

One possibility, which provides a negligible opening-time, is to use the projectile itself as a valve. Barnsley, Meredith and Robinson (1968) used an electro-mechanical clamp to hold the projectile at the breech until firing; Fowles et al. (1970) describe a

breech in which the projectile seals off the firing pressure until it is pushed forward a short distance by a small firing impulse. These techniques, however, demand a good seal between the projectile and barrel, which in turn requires extreme accuracy of the projectile dimensions and barrel bore.

Mechanical valves have been widely used: Miles and Pearson (1974) describe a fast-acting pneumatic valve for use with a gas gun; however, the opening time of this valve is about 5 ms, which is comparable with the transit time of a projectile in the gun used in this work. Perfect (1966) has used a similar valve, but experienced serious practical difficulties with it. Thunborg, Ingram and Graham (1964) used a pneumatically controlled gate valve, but this took 65 ms to open fully, and could therefore only be used at low velocities.

Perhaps the simplest valve is a single diaphragm, interposed between reservoir and barrel. The pressure in the reservoir is slowly increased until the diaphragm bursts, allowing the gas to accelerate the projectile. Such a valve has been used by Taylor and Davies (1942), but has the disadvantage that the bursting pressure of the diaphragm is only certain to within 5%. The technique is greatly improved by the introduction of a second diaphragm; the resulting valve has a very short opening time and negligible impedance to gas flow when open. The two diaphragms are separated by a small volume which may be pressurised independently from the main reservoir. If it is desired to use a firing pressure of P, diaphragms are selected which have bursting pressures between P/2 and P. The interdiaphragm space is charged with gas to a pressure of P/2, and the reservoir to a pressure P. The valve is stable in this state, a pressure difference of P/2 across each diaphragm being insufficient to burst it. In order to open the valve, the gas between the diaphragms is allowed to escape to the atmosphere, whereupon the rear diaphragm, now having a pressure difference of P across it, bursts. The front diaphragm, immediately behind the projectile, is then subjected to the full reservoir pressure, and it too bursts. Fowles et al. (1970) and Thunborg, Ingram and Graham (1964) have used this technique with success; Perfect (1966) modified it slightly, by applying a transient high

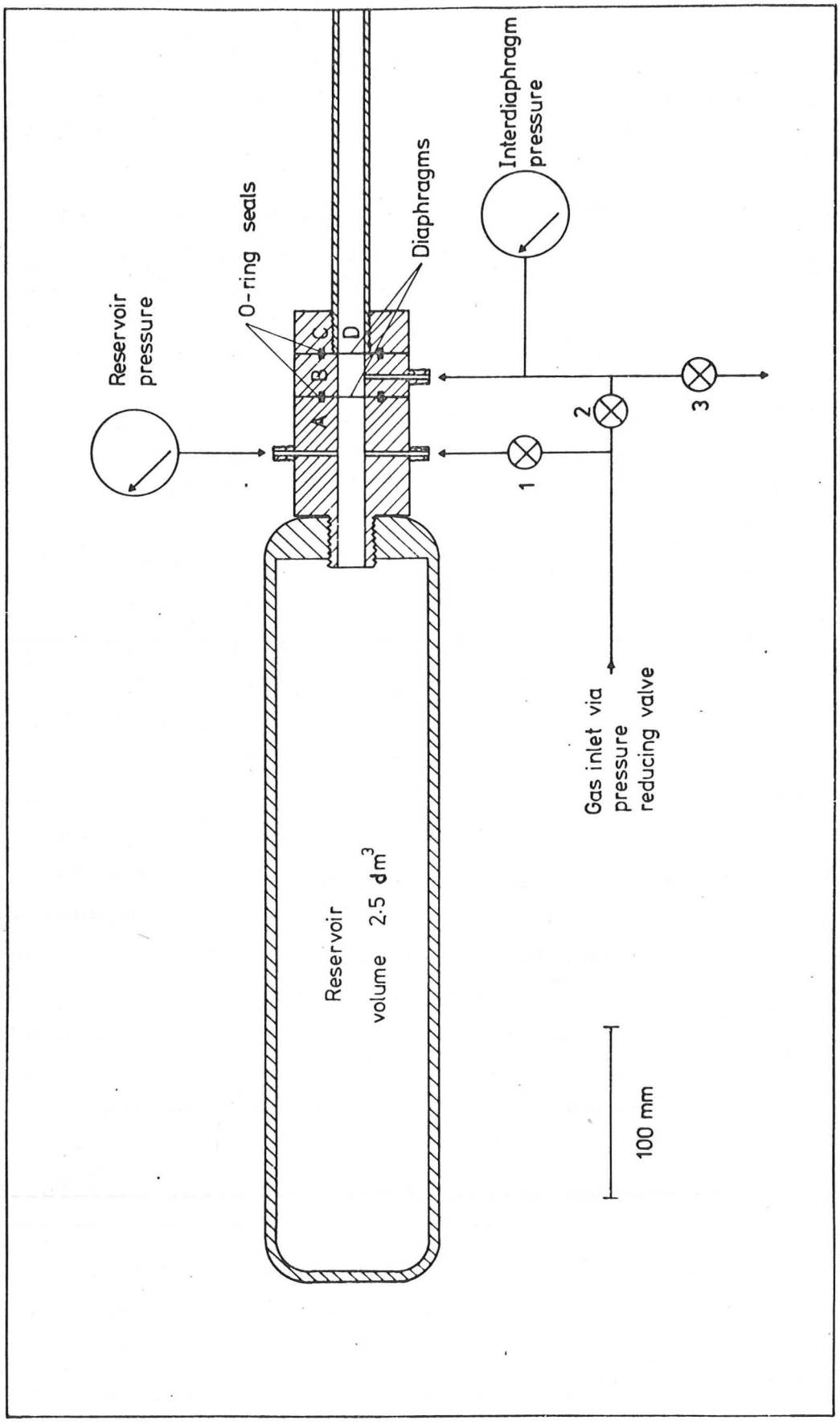

Figure 3.1
The gas gun, breech end, showing control system.

pressure to the interdiaphragm space in order to fire the gun. This method would appear less satisfactory, since the front diaphragm must burst before the rear, leading to an interrupted pressure rise at the projectile. Other methods of causing a single diaphragm to burst at a known pressure, such as puncturing with a stylus or fusing with an electric current, have been used, but lack the simplicity of the double diaphragm method.

3.4.1 Description of gas gun

The requirements of this work were met with a gun of calibre 16 mm, barrel length 1.03 m and maximum working pressure 3 MPa. The main features of the design are shown in figure 3.1. The reservoir is a steel gas cylinder, with a volume some ten times that of the barrel. In order to minimise the opening-time of the valve, the double diaphragm technique described above was used.

The breech separates easily into three sections, labelled A, B, and C in the diagram. The projectile is loaded into the barrel at D, and the diaphragms are placed between sections A and B and B and C. The breech is clamped together by six bolts which pass through sections B and C into A. Gas-tight seals are effected around the diaphragms by rubber O-rings on each side of the joint. The complete reservoir and breech assembly has been tested at a pressure of 10 MPa.

Figure 3.1 shows the control system in use with the gun; gas from a large cylinder flows via a pressure-regulating valve into the reservoir through valve 1 and into the interdiaphragm space through valve 2. In practice both reservoir and interdiaphragm space are pressurised together to half the required firing pressure; valve 2 is then closed and the pressure in the reservoir raised further. To fire the gun, valve 3 is opened, allowing the pressure between the diaphragms to drop. The pressure in the various parts of the system is monitored on gauges.

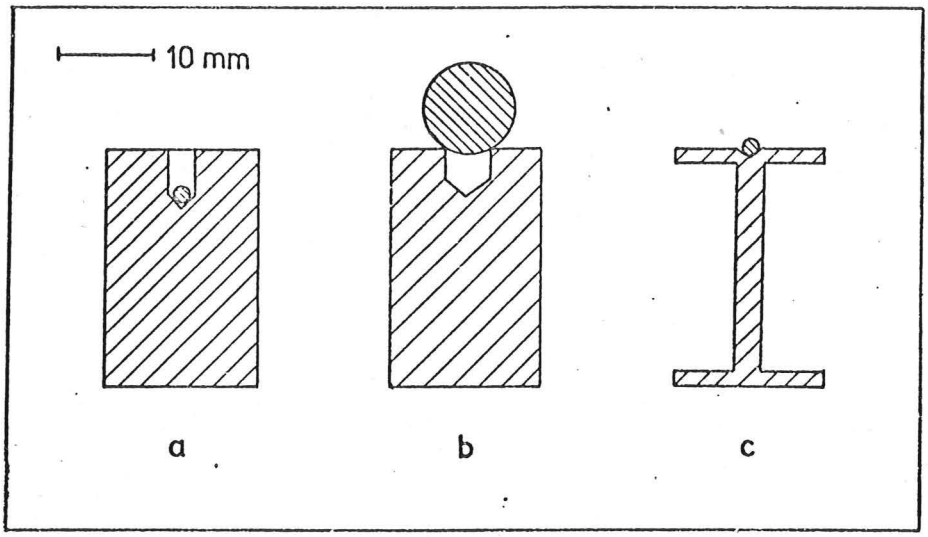

Figure 3.2
Sabots used to accelerate spherical particles of various sizes with the gas gun.

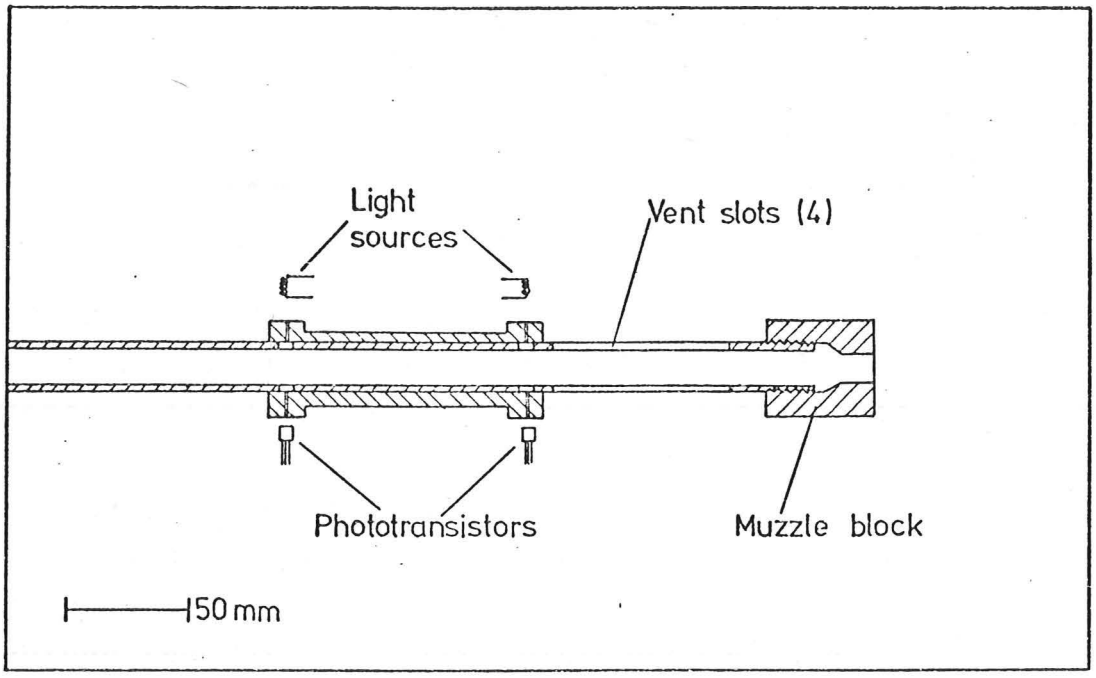

Figure 3.3
The muzzle end of the gas gun, showing the arrangement of the velocity timing components and the steel muzzle block used to stop the sabot.

3.4.2 Diaphragms

Using the double diaphragm system, the range of pressures used in this gun, from 0.1 to 3.0 MPa, may be covered with a small number of diaphragms. The types used and their average bursting pressures are listed in table 3.1.

Table 3.1

Diaphragm	Thickness / μm	Bursting pressure / MPa
Polythene	1 x 25	0.10
Copper	1 x 25	0.20
Aluminium	1 x 25	0.25
Copper	2 x 25	0.40
Aluminium	2 x 25	0.55
Aluminium	3 x 25	0.80
Copper	1 x 50	1.00
Copper	1 x 75	1.55
Copper	1 x100	2.40

The pressure at which any diaphragm will burst is uncertain to within 5% or so; this uncertainty must be allowed for in selecting diaphragms for a given reservoir pressure.

3.4.3 Projectiles

Since the bore of the barrel (16 mm) is larger than the particles which it is desired to accelerate, sabots are used to carry the particles down the barrel. A sabot (French - clog) is an expendable projectile which is a good fit in the barrel, and which is decelerated at the muzzle, allowing the particle to continue in free flight. Typical sabots used with this gun for accelerating spheres of different sizes are illustrated in figure 3.2. They are machined from high density polythene rod, and are a loose sliding fit in the barrel. The polythene provides low frictional drag during acceleration.

At the muzzle the sabot strikes the block shown in figure 3.3. The particle continues forward through the hole in the block, while the sabot is retained at the end of the barrel and prevents any debris (such as fragments of diaphragm) from following the particle. The muzzle block

screws onto the end of the barrel and may be easily detached for removal of the sabot. The vent slots milled in the barrel behind the muzzle block allow the gas to escape from behind the sabot.

3.5 Measurement of projectile velocity

3.5.1 Introduction

A photoelectric device was developed to measure the velocity of the projectile at the muzzle. The physical arrangement of the apparatus is shown in figure 3.3. Two pairs of holes in the barrel allow light beams, defined by 2 mm diameter apertures, to traverse the barrel. These light beams fall onto phototransistors connected into the circuit shown in figure 3.4. The time interval between the restoration of the light beams after they have been obscured by the projectile is displayed on a digital timer with an accuracy of $\pm$ 1 μs. Knowing the separation of the light beams, the mean velocity of the sabot over the timing distance may be calculated.

3.5.2 Description of electronic circuit

The circuit is composed of two identical channels; a logic gate which combines the signals from these channels supplies a single pulse to the timer. One channel and the logic gate are shown in figure 3.4.

The light from a 50 W tungsten-halogen bulb crosses the barrel and strikes the phototransistor (type BPX 29). In this state the phototransistor is fully conducting and the voltage at point A is about 4.8 v. As the projectile cuts off the light the current through the phototransistor drops. The voltage at the input to the monostable multivibrator (type 74121) falls almost to zero. When the rear of the projectile uncovers the light, the phototransistor switches on and the potential at the monostable input rises again. The waveform at point A resulting from these events is shown in the figure. Since the monostable, as used here, will trigger only when its input rises in potential, no output pulse appears at B until the rear of the sabot passes the light. The timing capacitor connected to the monostable

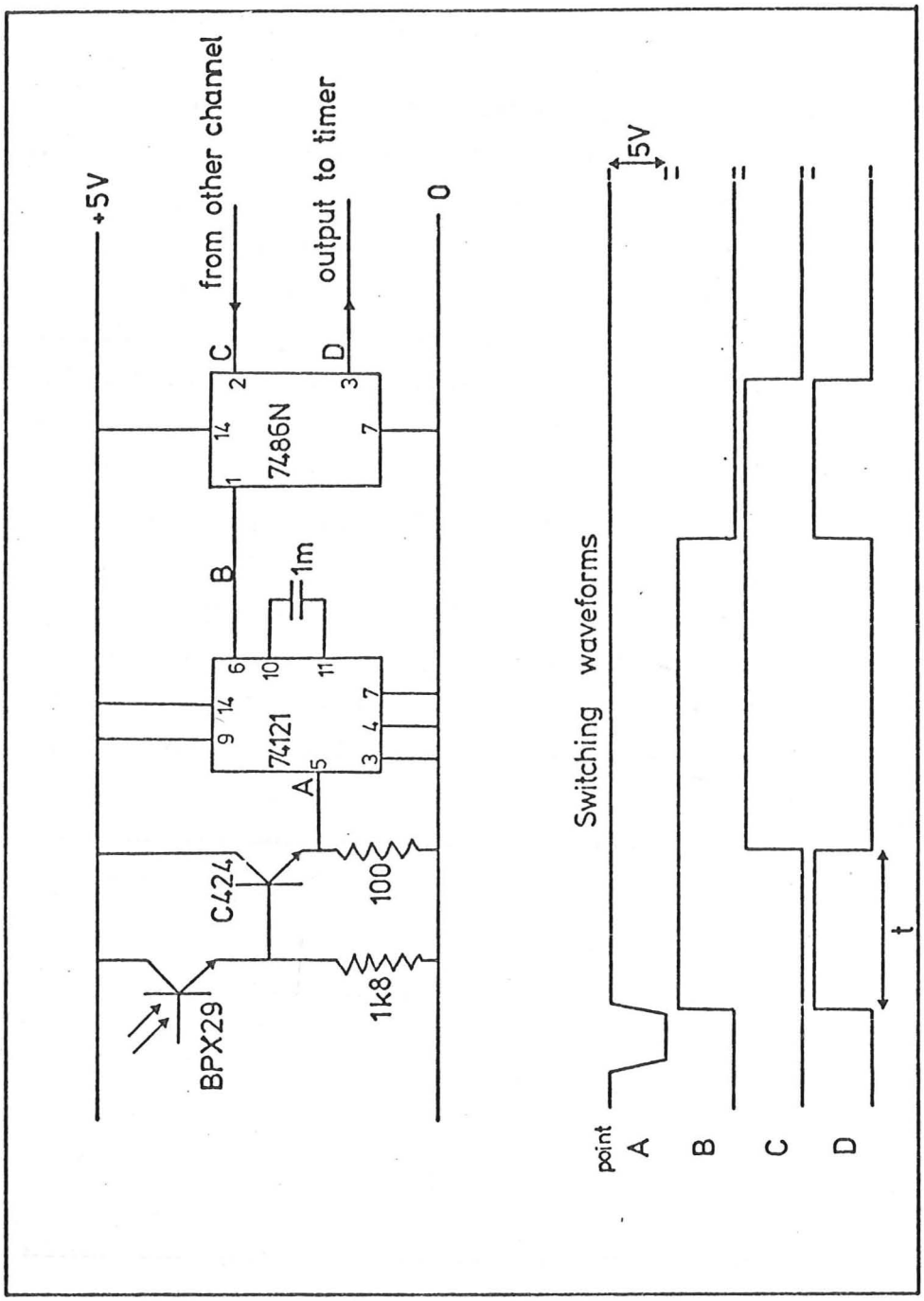

Figure 3.4
Circuit of photoelectric velocity timer used with gas gun.

is chosen to provide an output pulse length of ~1.5 s; during this time any further pulses at the input A have no effect upon the signal at the output B. The output pulses from the monostables in both channels are combined in an exclusive-OR gate (type 7486) which provides an output pulse at D of length equal to the time interval (t) between the triggering of the two channels. The second output pulse at D is suppressed by the timer, which will only accept one pulse until manually reset.

The long time constant chosen for the monostables effectively prevents any interference from fragments of diaphragm which may follow the projectile down the barrel. The decision to trigger the timer from the rear of the sabot was made to avoid interference from shock fronts which will form at high projectile velocity, and also took advantage of the shorter "switch-on" time than "switch-off" time of the photransistors.

The circuit has operated reliably and reproducibly for projectile velocities from 50 to 635 ms^{-1}, and has a high intrinsic accuracy. However, since the timing points are located on the barrel and the projectile will still be accelerating as it passes between them, the velocity at the muzzle will be somewhat higher than that calculated from the physical separation of the timing points and the measured time interval. Calibration experiments were therefore performed to check the correction needed to compensate for this effect.

3.5.3 Correction of velocity measurements

If we assume that the projectile accelerates uniformly in the barrel, we can calculate the correction needed to allow for the effect discussed above. As we shall see later, this calculation yields an upper limit for the correction, since the acceleration in fact decreases with increasing velocity.

Taking the total length of the barrel to be l, the physical separation of the timing points to be d and the distance of the timing point nearest the muzzle from the muzzle to be x, we find that the muzzle velocity v is given by :

$$v = \frac{2}{t} \cdot l^{\frac{1}{2}}((l - x)^{\frac{1}{2}} - (l - x - d)^{\frac{1}{2}})$$

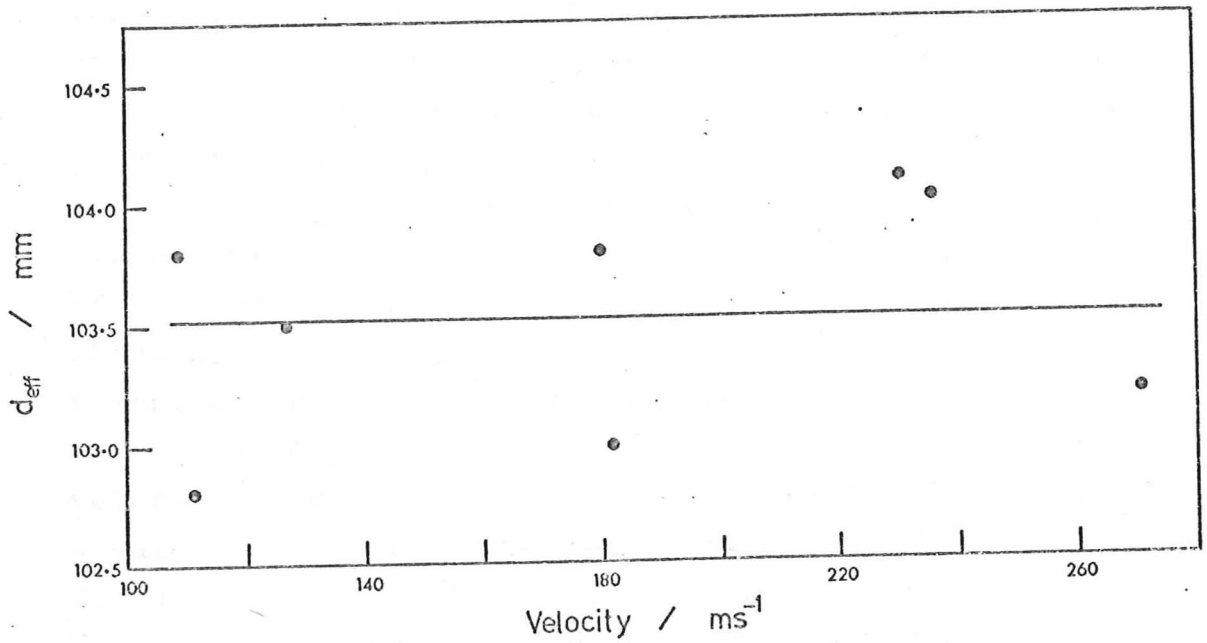

Figure 3.5
The effective separation of the timing points, d_{eff}, measured by the breaking-wire technique and plotted against velocity. No systematic variation is seen - the mean value of d_{eff} = 103.5 mm was used to compute velocities.

where t is the time interval measured at the timing points. We can therefore calculate the muzzle velocity from t by replacing the true separation d by an effective separation d_{eff}, where

$$d_{eff} = 2\, l^{\frac{1}{2}}((1 - x)^{\frac{1}{2}} - (1 - x - d)^{\frac{1}{2}})$$

For this gun, l = 1.035 m, x = 0.060 m and d = 0.100 m giving a value for d_{eff} of 105.8 mm. We could therefore take a value of 103.0 mm for d_{eff} for practical calculations and be sure that the possible error would be less than 3%, since it is inconceivable that the acceleration of the projectile would increase with velocity.

A more accurate measurement of d_{eff} was made experimentally. The projectile was allowed to pass out of the muzzle and break two thin (100μm) copper wires about 200 mm apart. These wires were used to trigger a timer, accurate to ± 1 μs, and the true muzzle velocity was measured in this way to within 0.5 %. From this velocity, and the time interval recorded photoelectrically, a value of d_{eff} could be calculated. The results of several measurements at different velocities are plotted in figure 3.5. The scatter in the points, 0.5 mm, probably results from slight variations in the separation of the wires, which were prestrained before use so that they would fracture at a very small extension. No dependence of d_{eff} on velocity is seen in figure 3.5. Velocity measurements were therefore calculated from the times measured photoelectrically using the mean of the values of d_{eff} in figure 3.5, i.e. a value of 103.5 mm. It is felt that the velocity determined in this way is certainly known to ± 1% and probably to ± 0.5%; the major source of uncertainty is not the measurement of the time interval, but the value of d_{eff}.

3.6. Performance of the gun

3.6.1 Introduction

The experimentally determined velocity characteristics of the gun are shown in figure 3.6. The velocity has been found to depend primarily on the ratio of reservoir pressure to projectile mass, as predicted by the constant pressure theory, with little dependence of velocity on pressure or mass alone. As may be seen from the curves, the velocities attained using helium as the driver gas are always appreciably higher than those with nitrogen. This effect is not predicted by the constant pressure theory, but it may be argued qualitatively that the lower viscosity, density and higher sonic velocity of helium must lead to greater efficiency.

3.6.2 Comparison with Seigel's theory.

A theory of gas gun performance, which takes into account the finite amplitude pressure waves propagating in the system during firing, has been published by Seigel (1965). This theory predicts a dependence of muzzle velocity upon P/m, but also incorporates the effects of reservoir volume, sonic velocity in the propellant gas, and the ratio of its specific heats (γ). Figures 3.7 and 3.8 show the performance of the gun over the lower part of the velocity range, and for comparison, the predictions of the constant pressure theory and that of Seigel. It is seen that with nitrogen propellant, the constant pressure theory overestimates the muzzle velocity by some 50% when the actual velocity is around 300 ms^{-1}. The error is not so great with helium, but Seigel's model gives a rather more accurate estimate for both gases. The discrepancy between performance and Seigel's theory is nevertheless appreciable, and it is instructive to consider possible reasons.

Seigel's basic theory ignores the retarding effect of the air in the barrel in front of the projectile; the correction due to this resistance forms a large part of the discrepancy between theory and practice. Although Seigel has not incorporated the effect into his model, he has given a simple correction term which is shown in figure 3.9 (solid curve). The correction is expressed as v, the actual

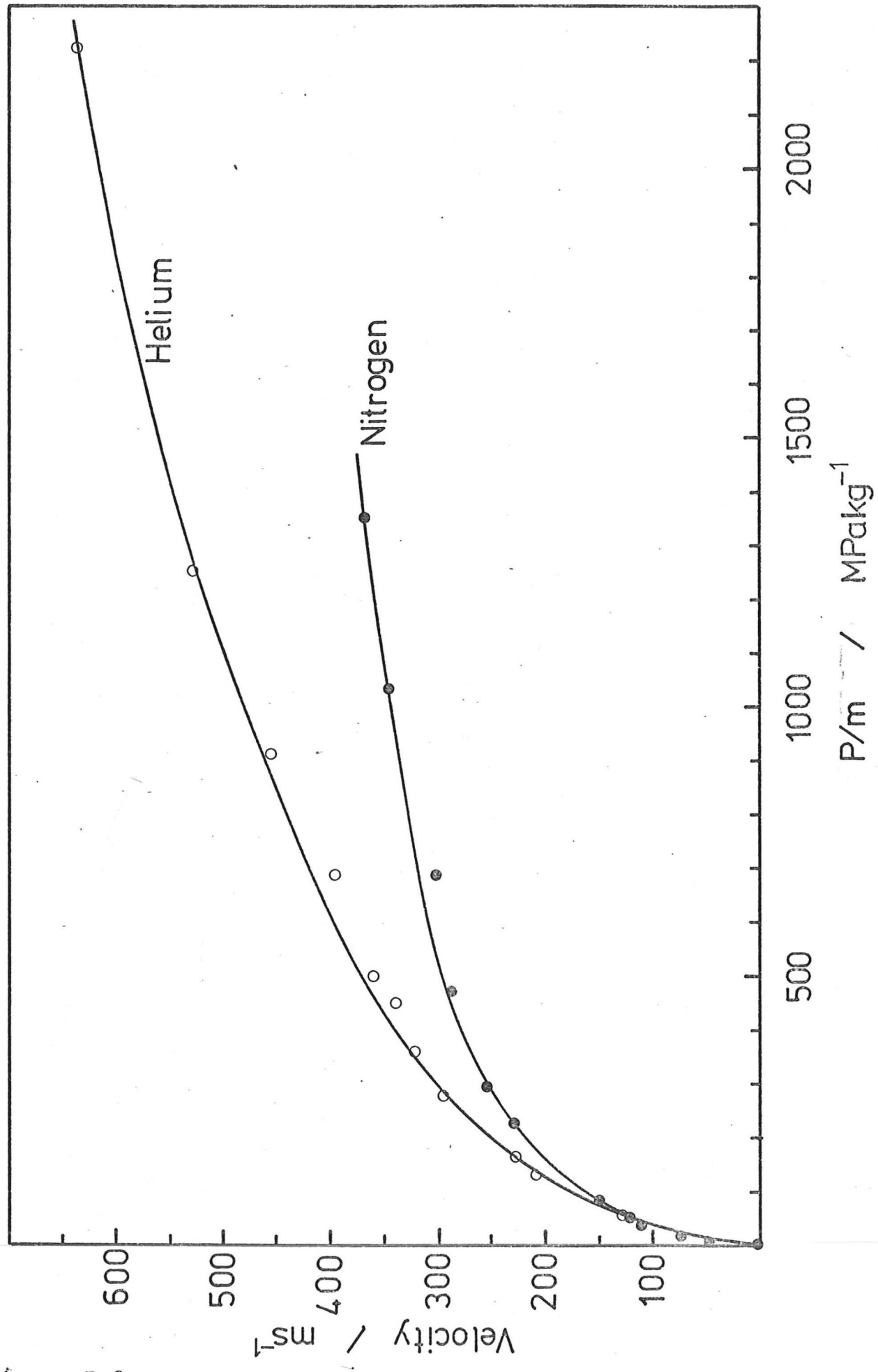

Figure 3.6

Performance curve of the gas gun for helium and nitrogen propellant gases.

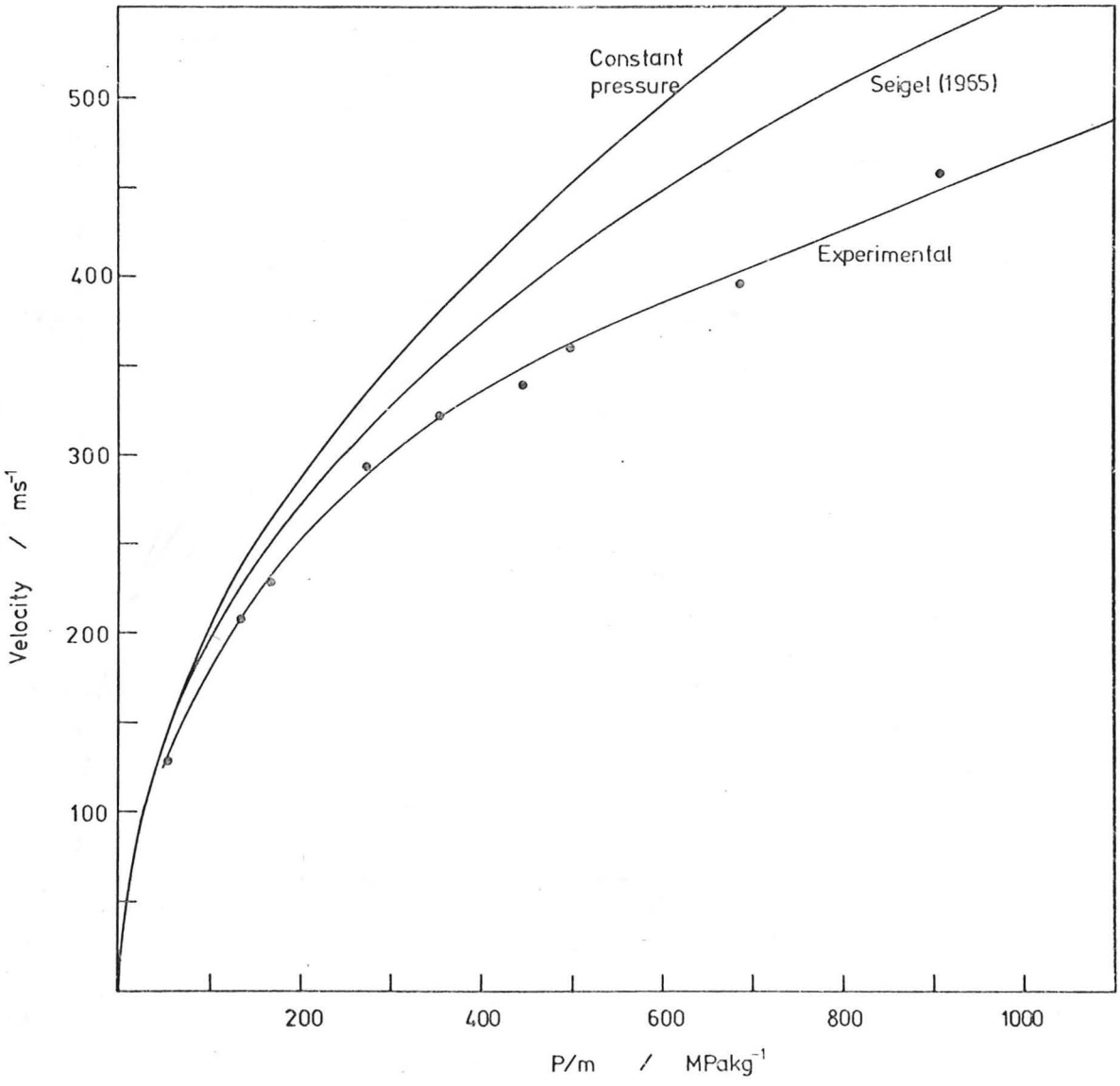

Figure 3.7
Performance of the gas gun using helium propellant gas. The predictions of Seigel (1965) and of the constant pressure theory are shown for comparison with the experimental points.

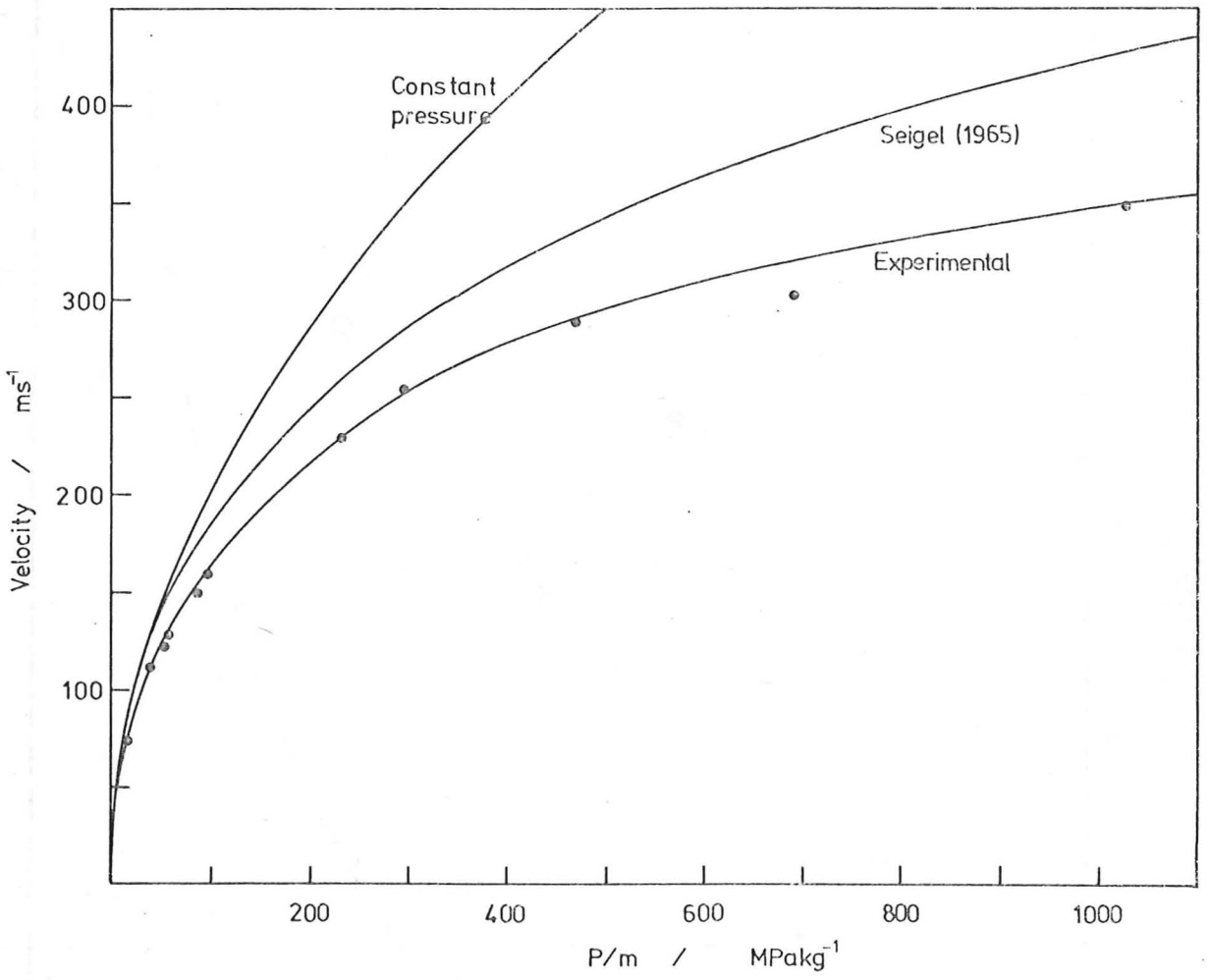

Figure 3.8
Performance of the gas gun using nitrogen propellant gas. The predictions of Seigel (1965) and of the constant pressure theory are shown for comparison with the experimental points.

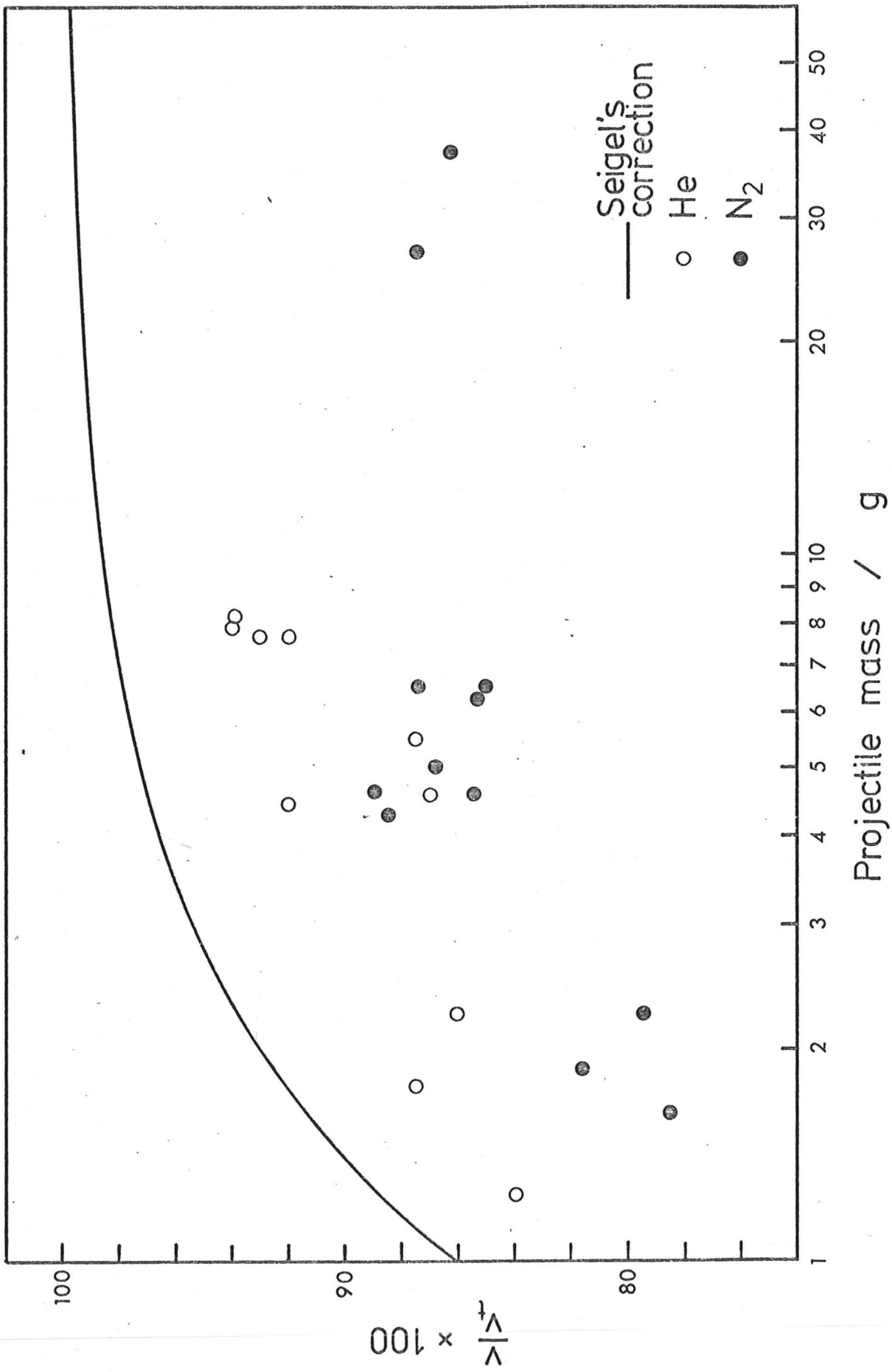

Figure 3.9
Seigel's correction to allow for the air in front of the projectile, compared with the performance of the gun with helium and nitrogen propellant gas.

velocity, divided by v_t, the velocity predicted by Seigel's basic theory; the correction depends only on the mass of the projectile, for a given gun. With a ten gram projectile, the correction is only ~2%, but for a mass of one gram it reaches 14%. Experimental results obtained with the gun are shown for comparison. Although they all lie below the solid line, they appear to lie on curves parallel to it, suggesting that the remaining discrepancy is independent of projectile mass, and amounts to some 6% with helium and 12% with nitrogen.

The abrupt change of section of the gun between reservoir and breech (figure 3.1) is certainly responsible for part of this error; Seigel assumes a well-matched tapering transition and a smooth gas flow. The main assumptions of Seigel's theory, namely that the expansion is reversible and adiabatic, are of course erroneous, but it may be argued that the importance of irreversibility in such a system is much greater in the case of sudden compression than in the situation here of sudden expansion (Seigel 1965).

3.7 Conclusions

The gas gun described here is a versatile laboratory tool, capable of accelerating projectiles to over 600 ms^{-1}. The system of expendable sabots used enables differently shaped particles of widely varying mass to be accelerated. Using the double diaphragm breech system, firing pressures may be accurately preset, and the muzzle velocity may be confidently predicted from a calibration curve to within 5%. The photoelectric method of measuring projectile velocity gives an absolute measurement to within less than 1%.

The performance of the gun has been compared with the predictions of a simple theory and that of Seigel (1965). The simple theory overestimates the muzzle velocity by 50% at 300 ms^{-1}, while that of Seigel gives a much better fit. The discrepancy between the Seigel model and the actual performance may be accounted for by the design of the gun and by the simplifying assumptions of the theory.

Chapter Four

Qualitative Observations of Single Particle Impacts

4.1 Introduction

In this chapter a qualitative study of the removal of metal by spherical particles is presented. The particles were accelerated using the gas gun described in chapter three; for reasons of convenience, large particles (3 - 10 mm) were used. Evidence will be presented in chapter 5 that the deformation processes occurring with these large particles are fundamentally the same as those with particles as small as 90 μm. The use of these large particles permitted metallographic examination of the damage site, and microhardness measurements could be made around single impact craters. As we shall see in chapter 6, the weight loss resulting from the impact of a single large particle may be measured, and compared with the results of multiple impact experiments.

Recent work by Winter (Winter and Hutchings 1974) has shown that angular particles, impacting with large negative rake angles, may indeed remove metal by a ploughing mechanism as suggested in chapter 2. The results of this work will be summarised and compared with the results obtained with spherical particles described in this chapter.

The experimental results were obtained using spheres of hard steel (ball-bearing steel). A tough material was needed since it was desired to eliminate the effects of fragmentation; ball bearings do not deform plastically even at high impact velocities on mild steel, the first signs of damage to the ball being brittle cracking (Carrington and Gayler 1948). Such cracking was not observed in any of these experiments. Steel balls are denser than real erosive particles (almost 3 times); the effects of ball density are discussed in section 5.3.3.

The results fall into two groups. Experiments with 3 mm diameter balls on aluminium, copper and mild steel at a shallow impact angle ($18\frac{1}{2}^{o}$) were used to show that removal of metal by a single spherical particle can occur under certain conditions, and to investigate the effect on the process of the plastic behaviour of the target metal. A more comprehensive study of the variation of damage with velocity and angle was then carried out using 9.5 mm steel spheres and mild steel targets. Metallographic examination revealed the mechanism by which metal was being removed. Each group of experiments will be discussed immediately after the results have been presented.

4.2 Experimental

The 3 mm and 9.5 mm (3/8 inch) diameter steel balls were accelerated using the gas gun. The sabots used for the smaller balls were as shown in figure 3.2 (a), while the design in figure 3.2 (b) was used for 9.5 mm balls. In this case the ball was attached to the sabot during firing by a small spot of low-strength glue (Durofix). The specimens were firmly clamped to machined angle blocks screwed to the muzzle block (figure 3.3); the angle of impact was thereby determined to within 0.5^{o}. Impacts with 3 mm balls were at 18.5^{o}, those with 9.5 mm balls at various angles.

The muzzle of the gun was enclosed in a strong steel enclosure, lined with rubber sheet, to contain the ball after impact and catch any fragments of metal detached.

4.3 Specimen materials

The 3 mm sphere impacts were carried out on specimens $\sim$ 3.2 mm thick. Aluminium specimens were cut from S1C-H4 rolled sheet (B.S.1470) with a Vickers hardness of 430 MPa. Mild steel specimens were cut from 12.7 mm cold drawn rod of En1A (0.1%C) free-cutting lead-free steel, VPH_{500} 2350 MPa. Work-hardened copper specimens were taken from hard drawn, high conductivity rod to B.S.2874 C102 and had a hardness of 1100 MPa. After annealing for 1h in vacuo at $900^{o}C$, their hardness was 400 MPa.

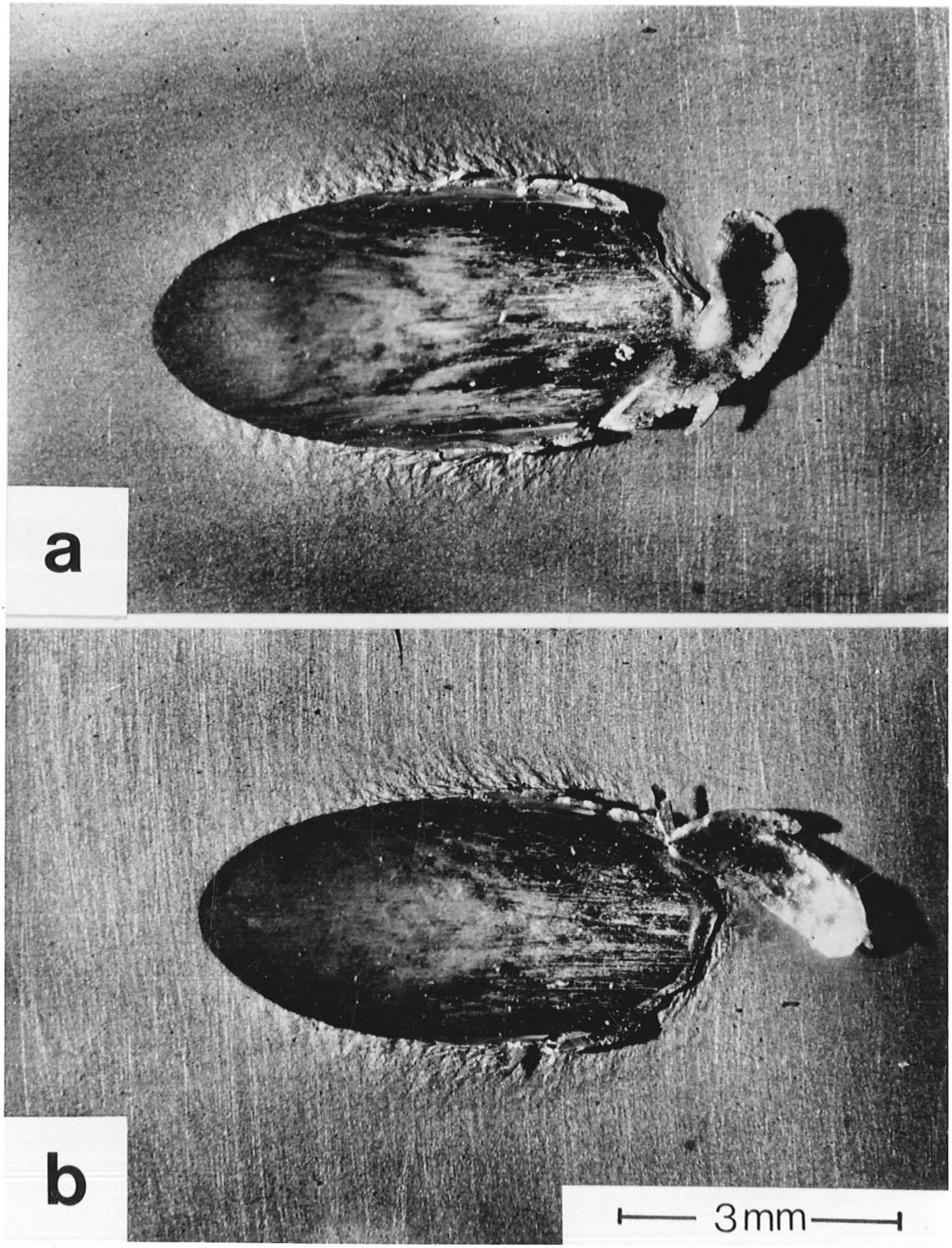
a
b
3mm

Figure 4.1
Craters formed in aluminium by the impact of 3mm diameter steel balls at $18\frac{1}{2}^{o}$. Impact velocities were
(a) 220 ms^{-1}
(b) 210 ms^{-1}.

Figure 4.2
Scanning electron micrographs of copper targets impacted by 3 mm steel balls at $18\frac{1}{2}^{o}$
(a) & (c) annealed copper, 215 ms^{-1},
(b) & (d) work-hardened copper, 220 ms^{-1}.

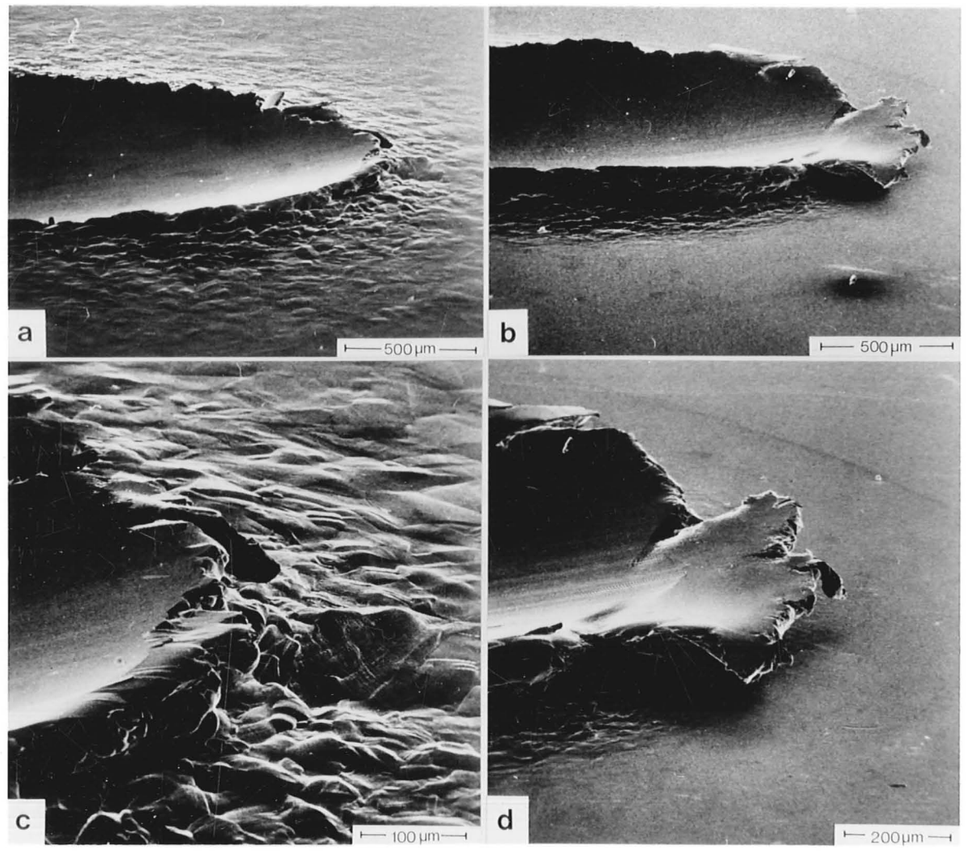

Mild steel specimens used with 9.5 mm steel balls were cut from 16 mm cold rolled square bar to En1A specification (0.15% C). The Vickers hardness was 2350 MPa. Impacts took place on the side faces of the bar, which were prepared by machining and final polishing with 600 grit silicon carbide paper.

4.4 Experiments at $18\frac{1}{2}^{o}$ impact angle

4.4.1 Results

The formation of a fragile lip at the exit end of the crater was observed in aluminium, mild steel and work-hardened copper. Figure 4.1 shows typical craters formed in aluminium impacted at 220 and 210 ms^{-1}. In both cases a lip has been formed and partially detached by the propagation of a rupture from one side of the crater to the other. The similarity of the damage in the two cases illustrates the reproducibility of the effect; although in detail no two craters are the same, the qualitative picture is very similar. At velocities above 220 ms^{-1}, the lip became completely detached by the impact.

Material removal by lip formation was also observed in mild steel. In this case, the velocity at which the lip became detached was lower ($\sim$ 180 ms^{-1}) although the size of the lip was smaller than in the case of aluminium. Lips formed in steel were observed to detach by the propagation of two ruptures, one from each side of the lip, in a manner similar to that to be described for work-hardened copper.

The copper specimens were used to investigate the influence of the plastic behaviour of the metal on the deformation process. Marked differences were noted between craters formed at the same velocity in work-hardened and annealed copper. Although , as would be expected from the hardness values, the crater in annealed copper was larger than that in work-hardened copper, the lip raised in the latter case was considerably larger than that in the former. The scanning electron micrographs in figure 4.2 illustrate this difference. Photographs (a) and (c) show the exit end of a crater formed in annealed copper; although considerable deformation is visible around the end of the crater, no lip of the type seen in figure 4.1 is seen. Work-hardened copper, on the other hand, has formed a

pronounced lip at almost the same velocity of impact (figure 4.2 (b) and (d)) and evidence of necking or rupturing is seen at the two sides of its base.

Examination of the specimens after sectioning and etching in alcoholic $FeCl_3$ solution showed the difference in depth of the two craters, and the more intensive shear deformation beneath the crater in the work-hardened copper (figure 4.3 (b)) than in the annealed specimen (figure 4.3(a)). Enlarged sections of the crater lips are seen in figure 4.4 ((a) and (c) work-hardened, (b) and (d) annealed). Not only is the work-hardened lip much larger than the annealed one, but it is much less firmly attached, being continuous with the bulk of the specimen over only a narrow neck. The lip in figure 4.4 (d) shows no overhang, and appears much more a part of the substrate.

Microhardness measurements were made on sectioned specimens to investigate the extent of the subsurface deformation. Figure 4.5 shows the hardness contours plotted for the two types of material. The deformation in the work-hardened case is more localised than in the annealed metal. This localisation may be further deduced from figure 4.2. The distortion of the previously flat metal surface beyond the end of the crater, visible in (a), is apparent up to 1 mm from the crater, whereas in the work-hardened copper (b) the surface appears undeformed immediately in front of the crater. The metal displaced at the sides of the crater follows the general trend; in the work-hardened case it piles up to a height of $\sim$200 μm, and in the annealed case, to a height of $\sim$100 μm.

In order to check that, in the annealed copper specimen studied, a lip had not in fact been formed and removed, similar targets were subjected to impacts at 51, 101, and 149 ms^{-1}. In no case was a lip raised which was at all similar to that seen in figure 4.2 (d), or larger than that in figure 4.2 (c).

The velocity at which the lip which was formed in work-hardened copper became detached during impact was found to be $\sim$250 ms^{-1}. At 270 ms^{-1} a lip weighing 1.6 mg was recovered, constituting a dimensionless "erosion" of 14.5×10^{-3} (weight loss per unit mass of impacting particles).

Figure 4.3
Etched sections through the craters formed in copper by 3 mm steel balls impacting at $18\frac{1}{2}^{o}$
(a) annealed copper, 210 ms^{-1},
(b) work-hardened copper, 220 ms^{-1}.

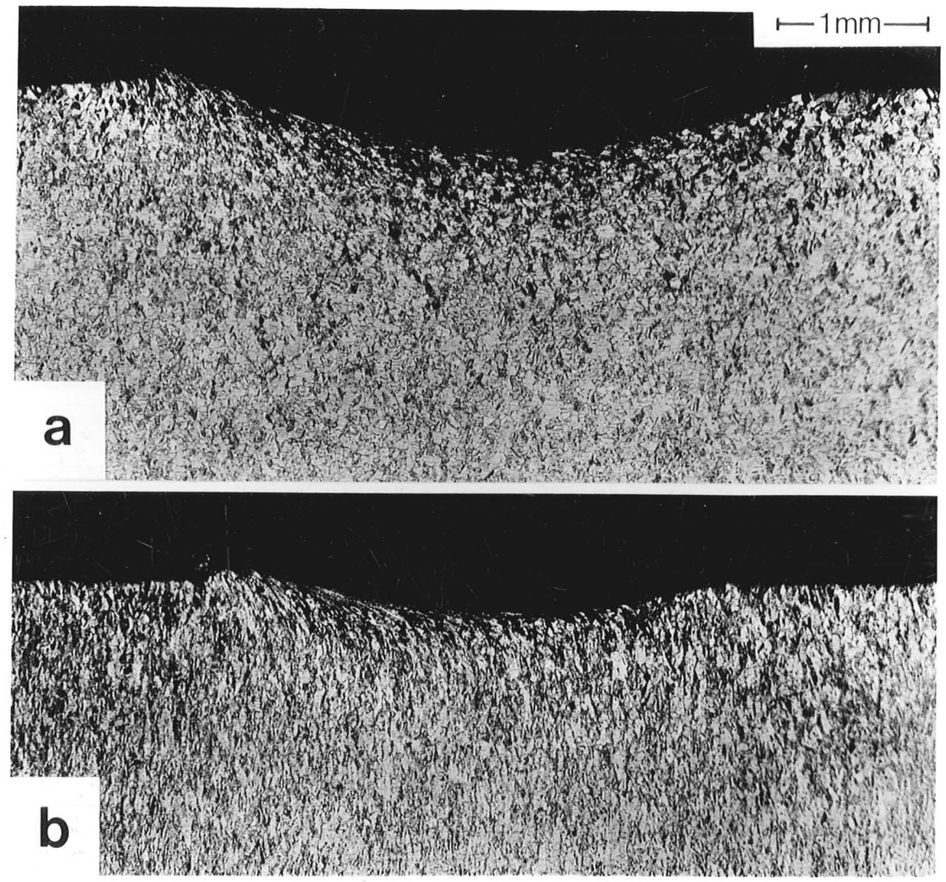

Figure 4.4
Enlarged views of the crater lips seen in figure 4.3.
(a) & (c) work-hardened copper,
(b) & (d) annealed copper.

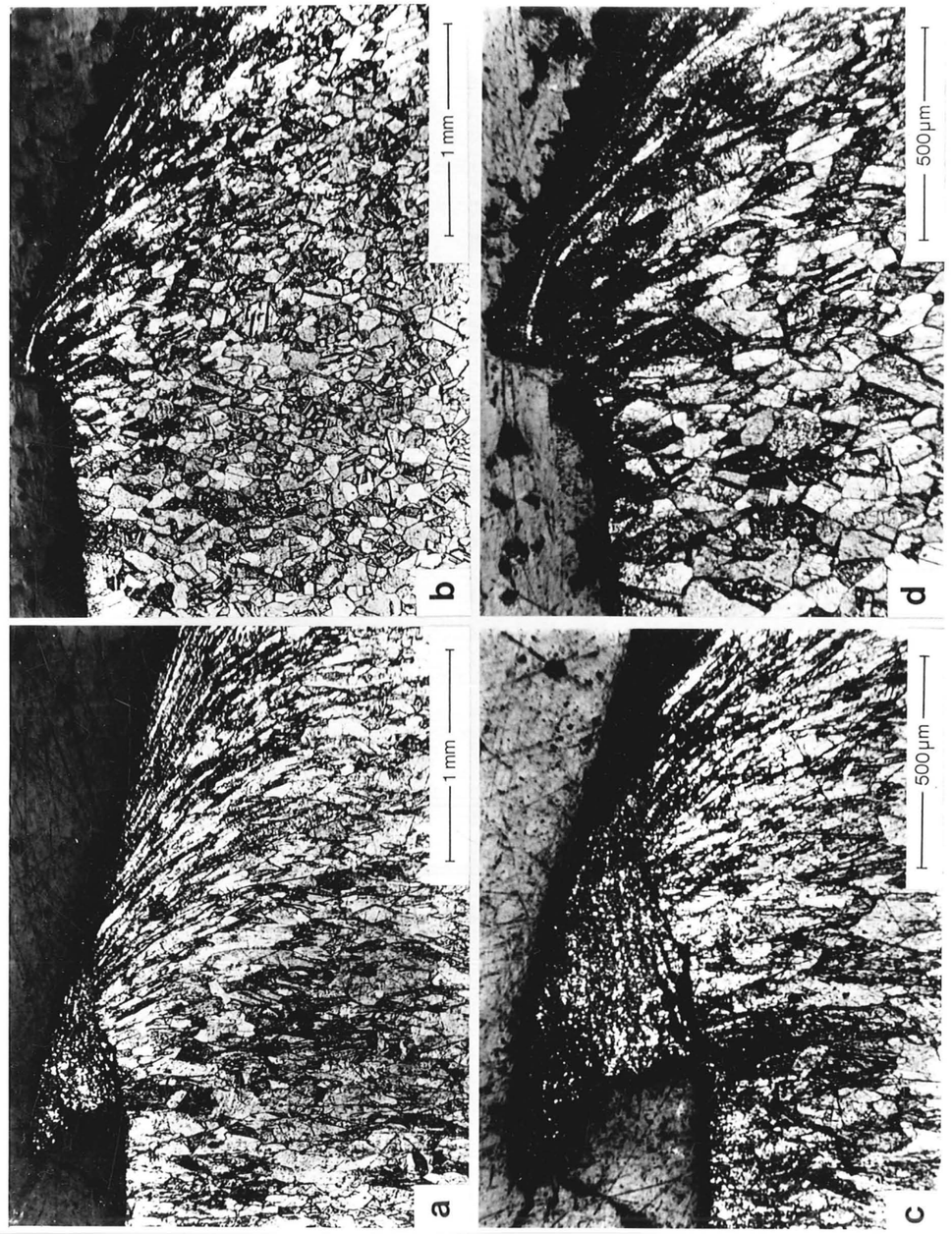

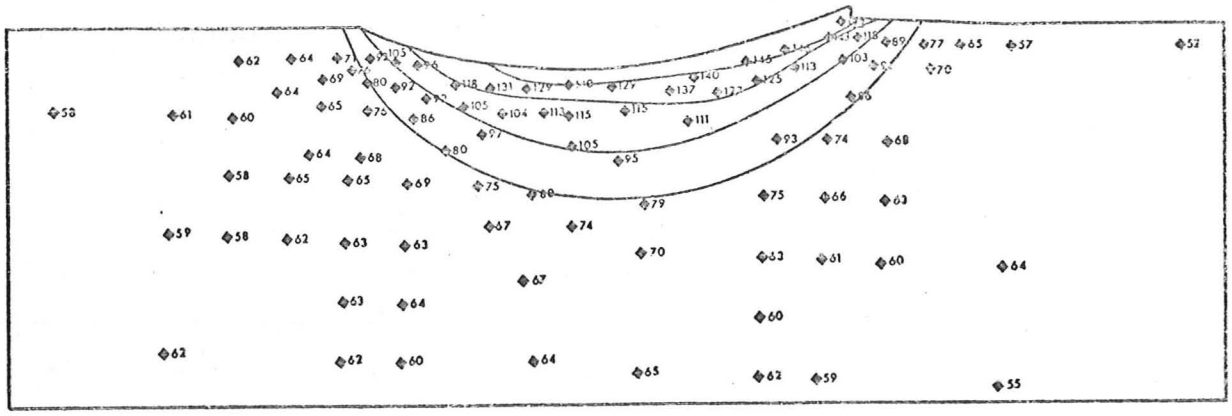

Figure 4.5a
Hardness contours (VPH_{50} in kg mm^{-2}) beneath a crater in annealed copper formed by a 3 mm steel ball impacting at $18\frac{1}{2}^{o}$ and 210 ms^{-1}. Hardness contours are shown at 80, 100 120 and 140 kg mm^{-2}.

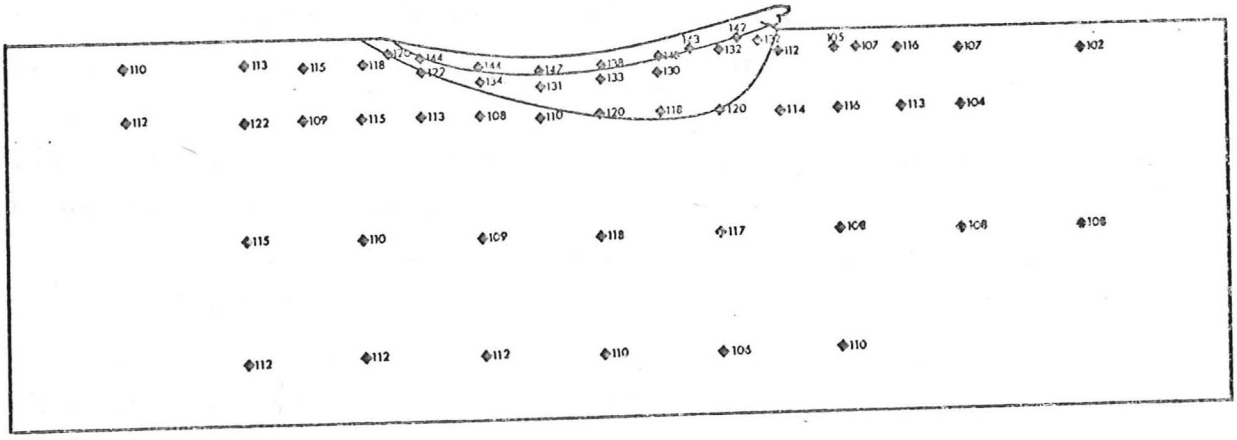

Figure 4.5b
Hardness contours beneath a crater formed in work-hardened copper by the impact of a 3 mm steel ball at $18\frac{1}{2}^{o}$ and 220 ms^{-1}. Contours are plotted at 120 and 140 kg mm^{-2}.

4.4.2 Discussion

These results indicate that metal can be removed by a single spherical particle impacting at a shallow angle on the three metals tested (aluminium, copper and mild steel). The mechanism by which the lips are formed and, at sufficiently high velocity, removed, appears to be the same in all three metals. Detailed examination of the specimens indicated that the lips are composed of material from near the surface of the metal which has been sheared in the direction of travel of the ball. Frictional forces between the surface and the sliding ball probably play an important role in the formation of these lips. At a critical velocity detachment of the lip occurs. For the well-defined impact conditions described here this velocity depends upon the target material.

The formation of larger, more fragile lips in work-hardened copper than in annealed copper can be explained by the different degrees of localization of the deformation in the two cases. Fully work-hardened copper approximates to perfect plastic behaviour: it deforms elastically until its flow stress is reached and then deforms plastically with little further increase in stress. Annealed copper, on the other hand, strain-hardens considerably. Tabor (1951) has shown that for quasi-static normal indentations in a fully work-hardened metal, the plastic deformation is localized and produces "piling-up" of metal around the indenter, whereas the widespread nature of the deformation in an annealed metal causes "sinking in". As an indenter is pressed into the surface, the annealed metal in the immediate vicinity of the indenter deforms first, but in so doing work-hardens, rendering its further deformation more difficult. The effective size of the indenter is increased by this shell of strain-hardened metal, and as the indenter penetrates deeper into the metal, material further and further from the indenter becomes strain-hardened. The deformation is spread over a large volume, and the level of the surface immediately around the indenter is depressed. It is suggested that a similar explanation is probable here. The spreading of the deformation which occurs in the annealed copper causes the plastic work done by the impacting ball to be dissipated over a large volume,

explaining the surface disturbance observed beyond the crater end, and the hardness contours in figure 4.5. The localization of shear deformation in the work-hardened metal results in intense shear in the surface layers, causing the formation of the large fragile lip at the end of the crater.

4.5 Experiments with 9.5 mm balls

4.5.1 Results

Figure 4.6 shows impact craters formed by 9.5 mm steel balls in mild steel at an impact velocity of 270 ± 5 ms^{-1}. The angle of impact varied from 10^{o} to 40^{o}. It is seen that both the size and nature of the impact crater are critically dependent on the impact angle. Overhanging lips can be seen at the exit end of the craters formed at angles of 10^{o}, 15^{o} and 20^{o}. At 25^{o} and 30^{o}, the lips have been completely removed, tearing with them part of the floor of the crater; the surface over which detachment has occurred may be clearly seen. Fragments of metal which had been detached were recovered in many cases. At 40^{o}, the lip has remained attached to the specimen; it is considerably larger than those formed at the lower angles.

The appearance of craters formed at different velocities but at the same angle is illustrated in figure 4.7. The lip formed at the exit end of the crater is seen to become larger with velocity until at a critical velocity, which for this angle lies between 174 and 178 ms^{-1}, it is detached during the impact. At higher velocities the lips are removed and increasing volumes of metal displaced.

Pronounced surface colouration was observed on the surface of many craters formed in steel at about 270 ms^{-1} and at angles varying from 20^{o} to 40^{o}. The colouring was intense at the exit end of the crater, and on the fragments of lip which were recovered. The phenomenon is visible in figure 4.8; the strong blue marking on the crater is rather more pronounced than the colour on the lip fragment.

Sectioning and etching (2% nital) of the specimens revealed deformation patterns very similar to those seen in work-hardened copper (see section 4.4.1). Figure 4.9

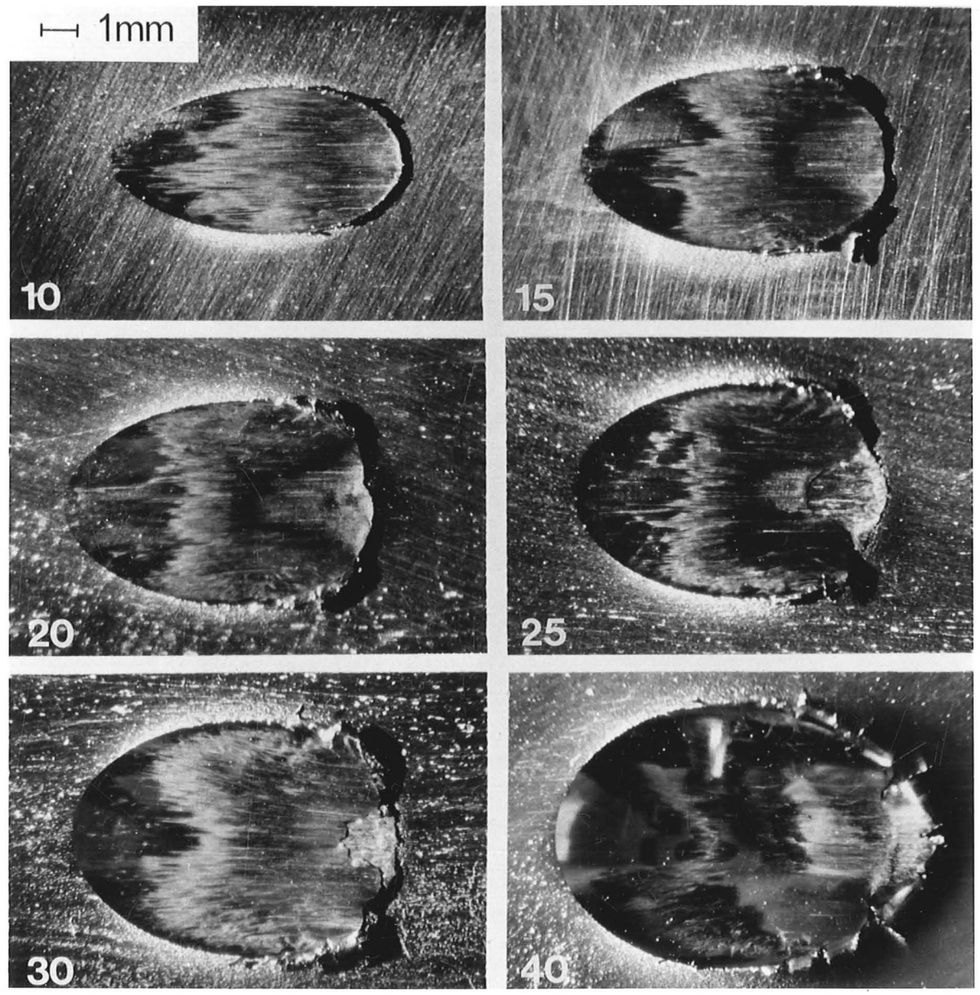

Figure 4.6
Impact craters in mild steel formed by 9.5 mm steel balls at 270 $\pm$ 5 ms^{-1}. The impact angle is marked on each photograph in degrees.

Figure 4.7
Impact craters in mild steel formed by 9.5 mm steel balls at an impact angle of 30^{o}. Impact velocities are marked on the photographs in ms^{-1}.

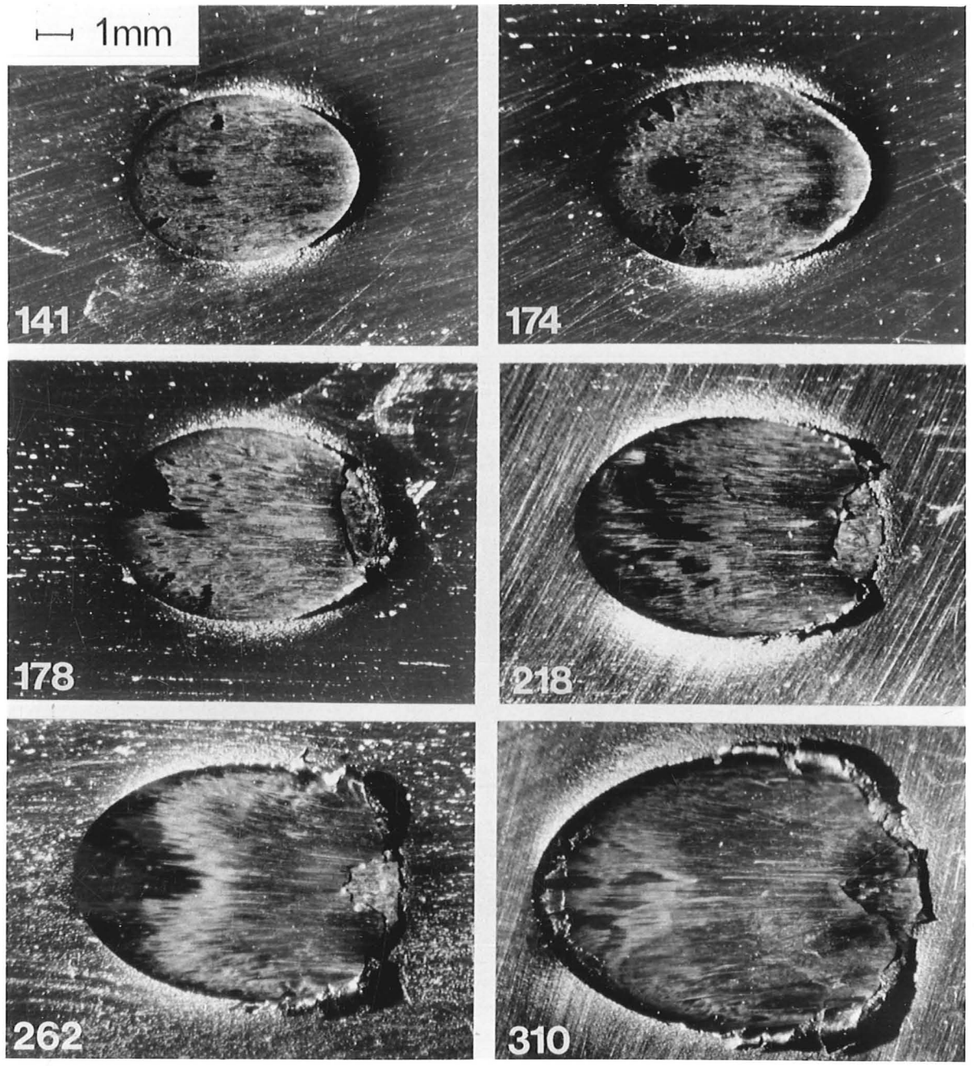

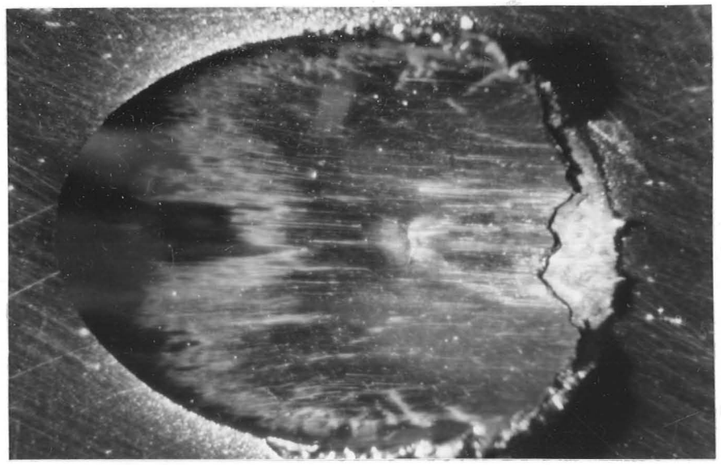

Figure 4.8a
Surface colouration on a crater formed in mild steel by a 9.5 mm diameter steel ball at 30^{o} impact angle and at 274 ms^{-1}.

Figure 4.8b
Two fragments of lip detached from the crater shown above during impact.

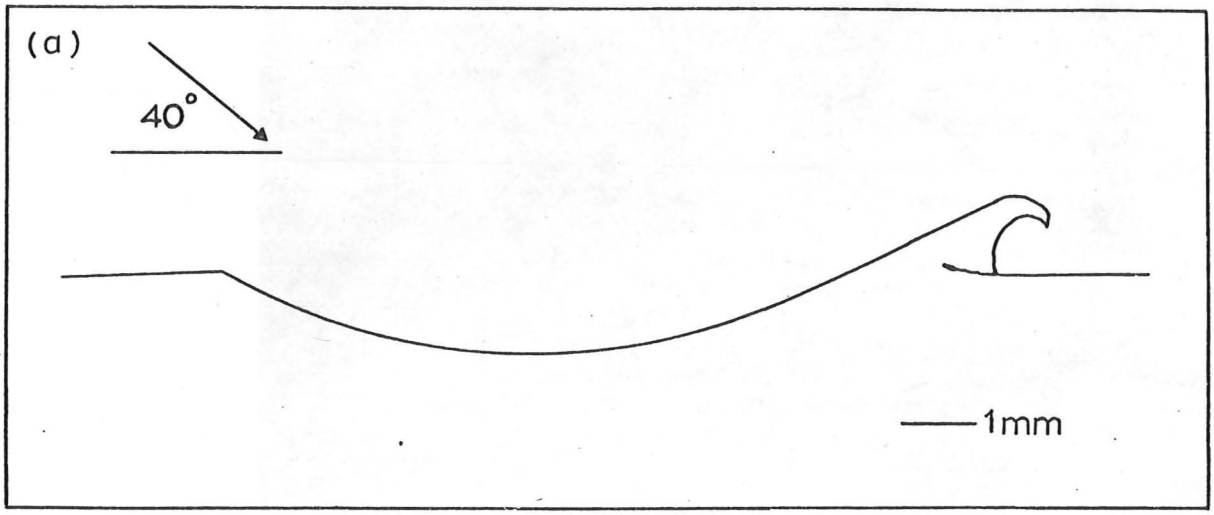

Figure 4.9

(a) Section through a crater formed in mild steel at 40^{o} and 270 ms^{-1} by a 9.5 mm steel ball; note the scale of the lip in relation to the size of the crater.

(overleaf)

(b) Etched section of the lip in (a). S indicates a band of intense shear at the base of the lip; vv is a void - the lip is attached to the bulk of the specimen over a small region only.

(c) Enlarged view of the shear band.

(d) Elongated grains in the shear band, typically ~1 μm wide.

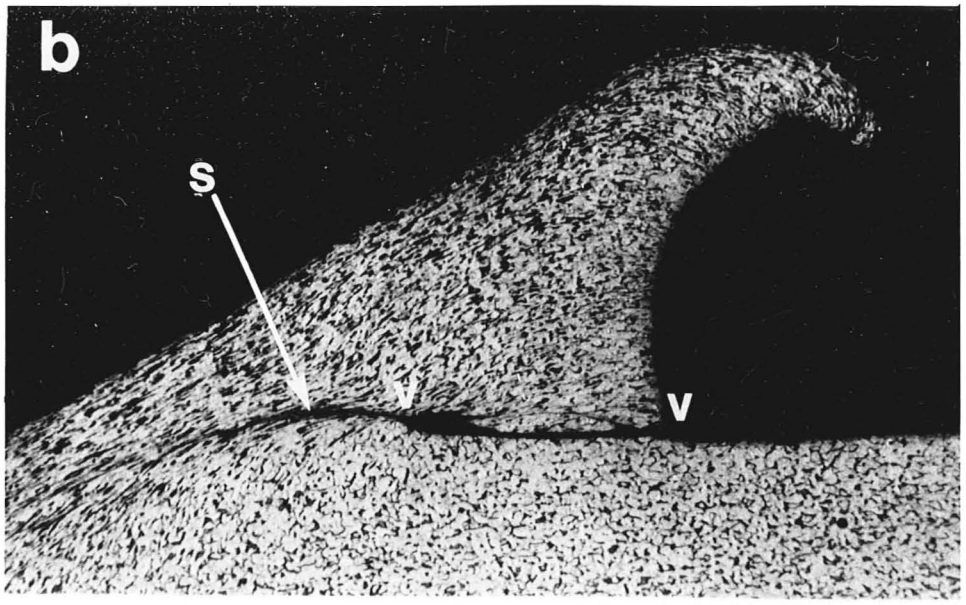
b
S
V

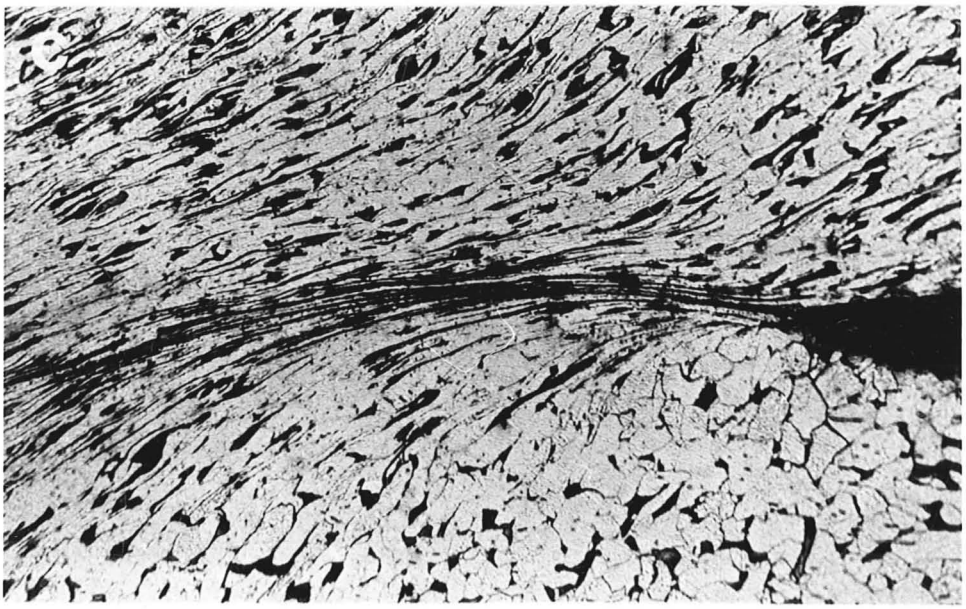
c

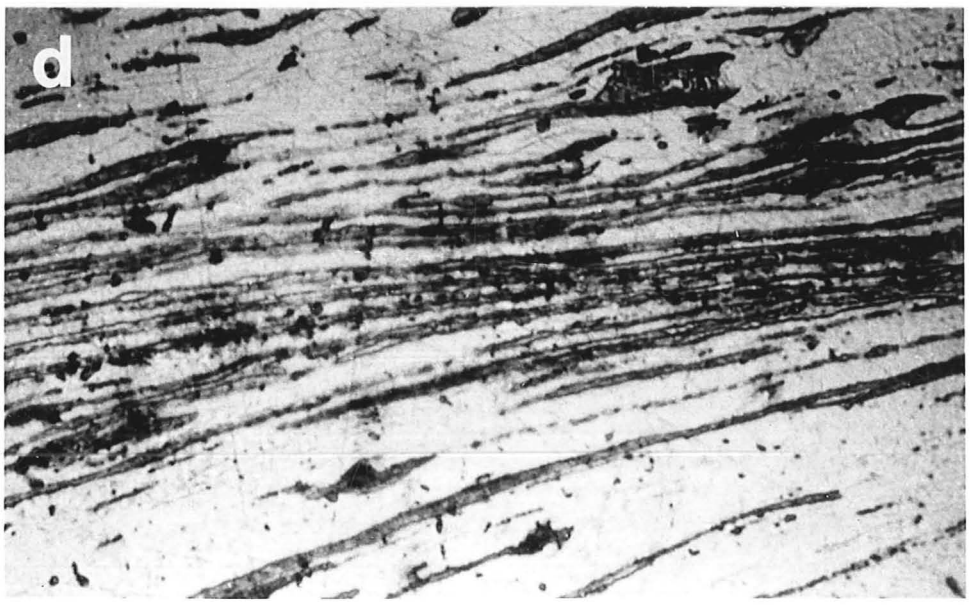
d

Figure 4.10
Etched sections through a crater lip formed in mild steel by the impact of a 9.5 mm diameter steel ball at 30^{o} and 174 ms^{-1}. (b) & (c) show the shear band at higher magnification.

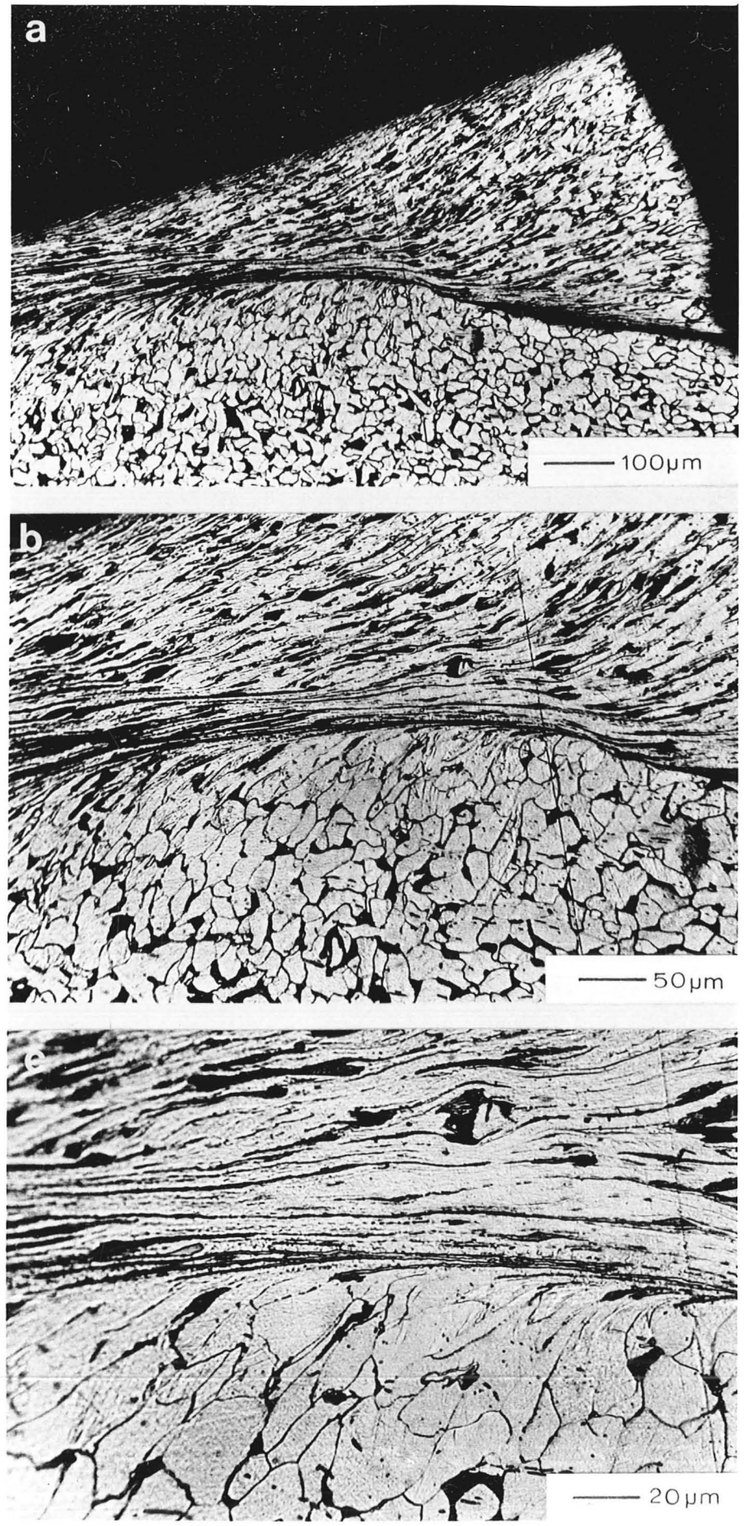

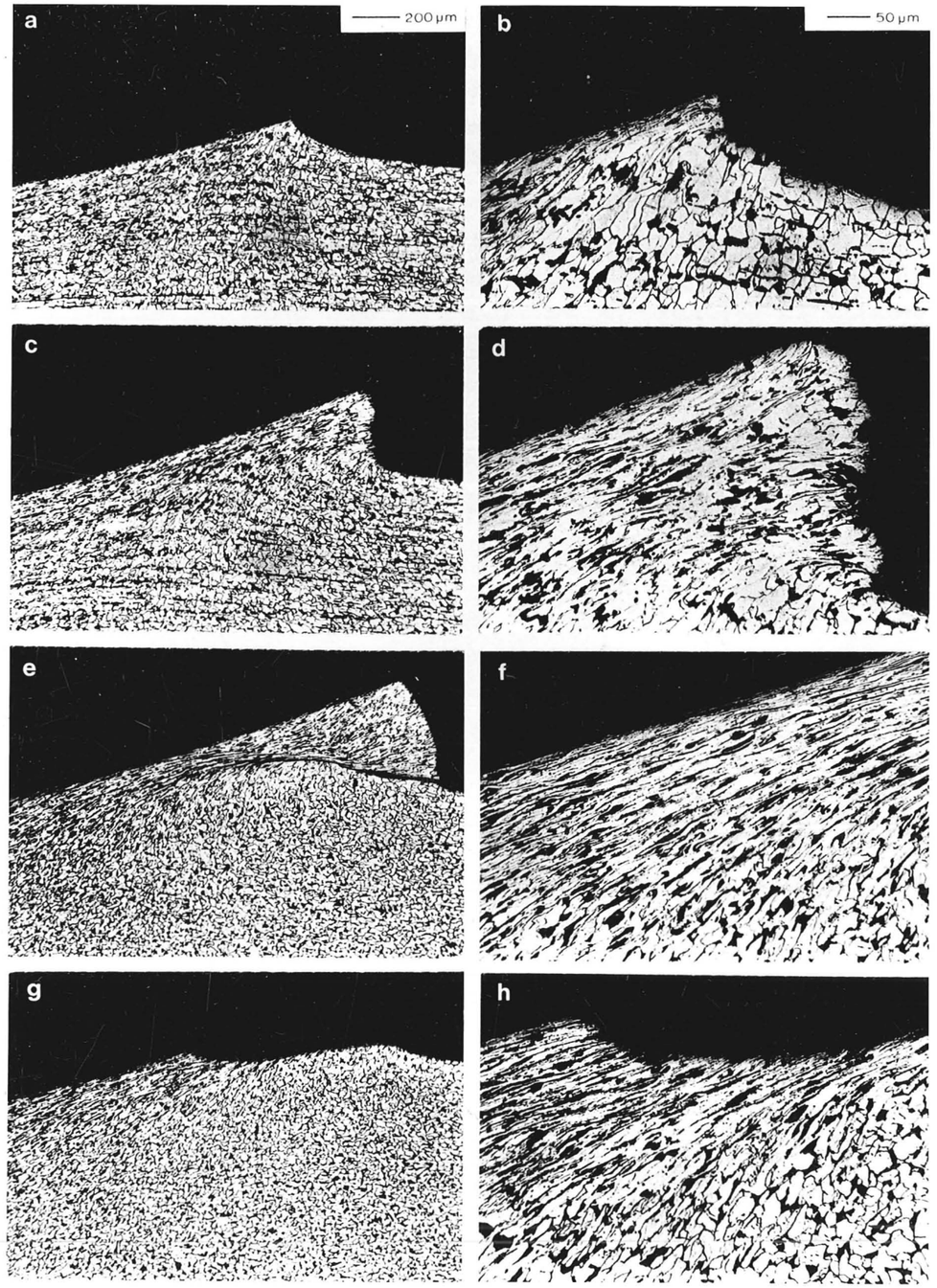

Figure 4.11
Etched longitudinal sections through craters formed in mild steel by the impacts of 9.5 mm diameter steel balls at 30^{o} and
(a) & (b) 90 ms^{-1}
(c) & (d) 143 ms^{-1}
(e) & (f) 174 ms^{-1}
(g) & (h) 178 ms^{-1}.

shows a crater formed at 40° and 270 ms^{-1}; the scale of the lip in relation to the whole crater may be seen in (a). The lip (b) is folded over onto the undisturbed metal, being separated from it by the void vv. The region over which the lip is attached to the bulk of the specimen is small, and contains a region of very highly strained metal (s). This shear band is shown further magnified in figure 4.9c and d; the overall width of the band is ~20 μm; individual ferrite grains have been deformed to a thickness of ~1 μm, whereas undeformed grains in the bulk of the metal are approximately equiaxed and ~25 μm across. Shear bands of this type were seen in sections of many craters; figure 4.10 shows details of a crater lip formed by an impact at 30° and 174 ms^{-1}. The ferrite grains in the band (figure 4.10c) are even thinner than those in figure 4.9d.

At a sufficiently high velocity, the lip at the exit end of the crater is detached during the impact; examination of craters from which the lip has detached reveals that detachment occurs within a shear band of this type. Figure 4.11 shows the lips formed by steel balls impacting at 30° and at velocities between 90 and 174 ms^{-1} (a - f). It is seen that the lip size increases rapidly with velocity; the shear band first appears at some velocity between 143 and 174 ms^{-1}. At 178 ms^{-1} (figure 4.11 g and h) the lip is detached during the impact. Comparison of sections g and h with e and f indicates that the lip has become detached along the line of the shear band.

Several detached lips were examined by sectioning; they all consisted of metal which had undergone considerable deformation, the grains being elongated and sheared by large strains. Figure 4.12 shows a section, etched in Nital, of a lip detached by an impact at 30° and 264 ms^{-1}. The lip is similar in shape to that in figure 4.9 and is composed of extensively deformed grains. Figure 4.12b shows an enlarged view of the lower surface of the lip, which would have formed a part of the shear band had the lip remained attached to the target. On the edge of this section are visible a number of very small grains, ~1 μm across; similar microcrystallites are visible on both sides of the tail of the lip in figure 4.12 c.

Transverse sections of craters formed at oblique angles of impact showed that the lips formed at the sides of the craters were more firmly attached to the bulk of

Figure 4.12
Etched section through a lip detached from mild steel by the impact of 9.5 mm steel ball at 30^{o} and 264 ms^{-1}.
(b) shows an enlarged view of the lower surface of the lip.
(c) shows the tail end of the lip at the same magnification as (b).

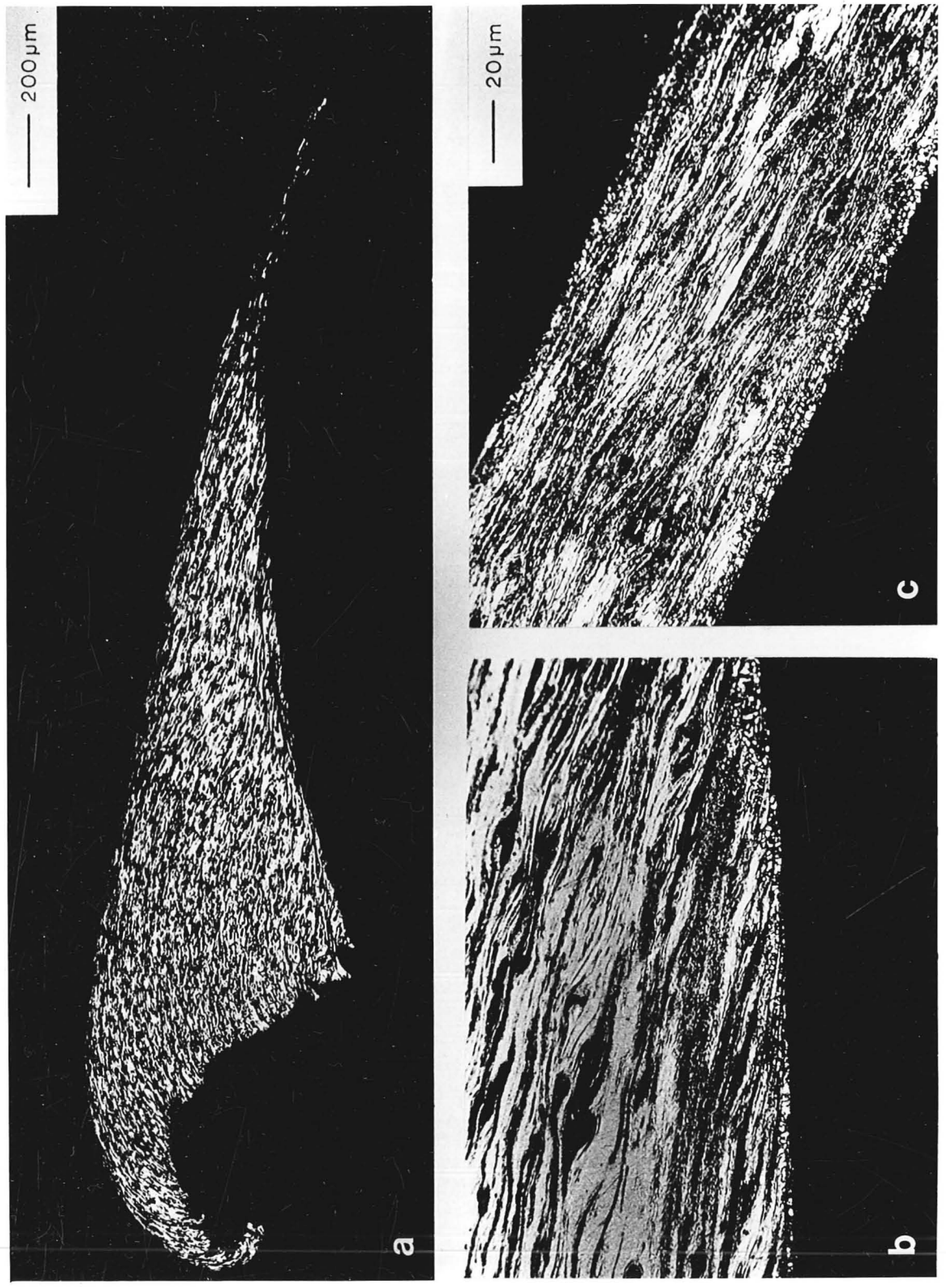

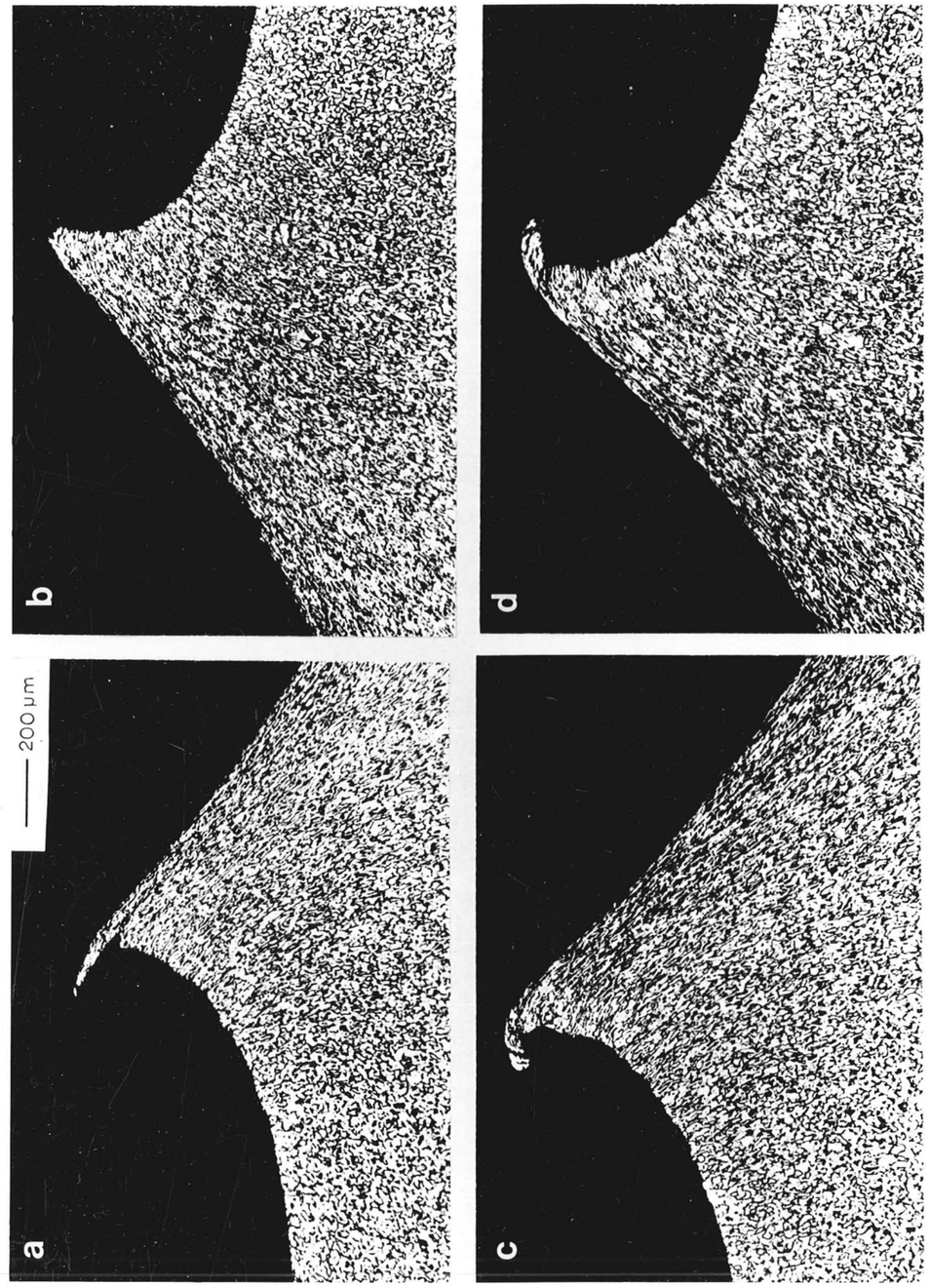

Figure 4.13
Lips raised at the sides of craters in mild steel by the impact of 9.5 mm steel balls (transverse sections).
(a) and (b) impact angle 30^{o}, velocity 263 ms^{-1}.
(c) and (d) impact angle 40^{o}, velocity 266 ms^{-1}.

the metal than those formed at the ends of the craters. No bands of shear or "folding-over" of the raised material were observed. Typical photomicrographs are seen in figure 4.13; although the main bulk of the lip is not heavily deformed, in most cases a small fragment of metal at its tip appears fragile and highly strained. Comparing figure 4.13b with 4.13a we see that such a fragment has probably been removed in the former case. Very similar lips are seen around craters formed at normal impact; sections are illustrated in chapter 8.

4.5.2 Discussion of mechanism of lip detachment

From the observations described above, it is possible to identify the mechanism by which the lip becomes detached during impact. The evidence of figure 4.11 indicates that the lip separates from the bulk of the target along the line of a band of intense shear; in all cases where the lip detaches at a critical velocity, sections of craters formed below that velocity reveal a similar shear band below the lip. The band is probably formed by the phenomenon of adiabatic shear; it is unlikely that any geometrical constraints to the deformation would yield such a narrow band, and there is ample evidence of high temperatures associated with the band, such as one would expect to find if it arose from adiabatic shear.

Adiabatic shear bands were first reported by Zener and Hollomon (1944); in the high-speed punching of hard carbon steel, they found narrow (~30 μm wide) bands which etched white with nital, and in which no structure could be resolved optically. They attributed their formation to localized thermal softening of the metal; at high rates of strain, the deformation would be effectively adiabatic, and if the rate of thermal softening outweighed the effects of strain hardening and the increase in shear strength with strain rate, catastrophic failure in a narrow band would ensue. The effect has been studied by several other workers. Wingrove (1971) has shown the structure of the bands to be martensitic, as originally speculated by Zener and Hollomon; the high temperature generated by plastic flow in the bands is sufficient to cause local transformation

of the structure of the steel to austenite, which is then quenched by the surrounding metal to form martensite.

The shear strain within the band shown in figure 4.9, for example, may be estimated from measurements of the elongation of individual grains. A simple calculation, assuming that all the work associated with the deformation is instantaneously converted into heat within the shear band, yields a temperature rise of some 4000 K. This must be an overestimate, since heat will be rapidly conducted away by the surrounding metal, but the thermal mechanism suggested above is clearly a feasible explanation for the formation of these bands. The shear bands observed in these experiments are, however, not martensitic, nor optically irresolvable; the ferrite grains and pearlite regions within the bands are very elongated, but are still discrete, indicating that the transformation to austenite has not taken place. The temperature needed for the complete transformation with a steel of this composition is ~1150 K, the transformation starting at ~990 K; this therefore puts an upper limit on the temperature which may have developed in the band. However, this may well be sufficiently high for thermal softening and preferential shear in the band to occur. Campbell and Ferguson (1970) have shown that at strain rates of ~4 x 10^4 s^{-1} the yield stress of mild steel decreases by over 40% as the temperature is raised from 300 to 700 K.

The surface colouration seen in figure 4.8 lends further support to the theory that localized heating occurs in the shear bands. The colours arise from optical interference within thin films of iron oxide (Fe_2O_3 and FeO) formed on the surface of the steel; such oxidation is conclusive evidence of high temperatures having been reached by the surface. The colours of oxide films on iron have been studied by Constable (1928), who tabulated the thickness of film corresponding to the different colours. The sequence of colours differs somewhat from the normal sequence of interference colours seen, for example, in a soap film (Newton 1704), because the oxides are strongly dispersive and absorbent. For the same reasons the colours of thicker films, formed by second and subsequent orders of

interference, are not distinct, so that the thickness of the film is defined uniquely if it appears of a strong, well-defined colour. The sequence of colours listed by Constable is: straw, reddish yellow, brownish red, purple, violet and blue; beyond blue the sequence is very dull. Constable found the thickness of a straw coloured film to be 46 nm, and that of a blue, 72 nm. It is noteworthy that the range of film thickness for which distinct colours are seen is small; it is therefore not surprising that the bright colours seen in these experiments only occur within a small range of impact conditions, and disappear at higher velocities.

There are three possible sources of heat which may have caused the surface oxidation:

(i) plastic deformation of the bulk of the metal around the crater, associated with the formation of the crater,

(ii) localized plastic deformation within the shear band discussed above and

(iii) frictional heating caused by the ball sliding over the crater surface.

The well-defined boundary of the blue area suggests that (i) cannot be the only source of heat, although it may well be responsible for the general straw colouration visible over most of the crater floor in figure 4.8a. The abscence of any colouration on the surface of the steel ball examined after impact, over a range of velocities, suggests that (iii) is not the cause; slow heating of a ball and a steel target in air resulted in identical oxidation colours on both surfaces. We must therefore conclude that the intense colouration in figure 4.8a and on the lip fragments in figure 4.8b results from heat developed in the localized shear band. This band is seen in figure 4.9 and 4.10 to be close to the surface at the base of the crater lip; heat developed in the band will be rapidly conducted to the surface.

The small undeformed crystallites seen in figure 4.12b and c on the surface of the detached lip appear to have formed by recrystallization; however, no similar small undeformed grains were seen in the shear bands formed beneath undetached lips. It must be concluded that

the extra temperature rise needed to permit the growth of these grains arose as a result of the detachment process; a probable explanation is frictional heating between the lip and the target during detachment. The temperature rise in the shear band of an undetached lip is limited by the shear deformation which has occurred in the band; when fracture occurs along the shear band the lip may continue to slide over the underlying surface for some time, resulting in a further rise in its surface temperature. This sliding of similar metals under a heavy load may account for the torn appearance of the region from which the lip has become detached, visible in figures 4.6 and 4.7.

4.6 Impacts of single angular particles

Winter (Winter and Hutchings 1974) has studied the mechanisms by which metal may be removed by the impact of single angular particles. The particles were of millimeter dimensions and were accelerated using the gas gun described in chapter 3.

The mode of deformation at shallow impact angles was found to depend on rake angle in the way discussed in chapter 2. Attempts to model a "cutting" situation, in which the particle has a positive rake angle and cuts a chip from the surface in the way envisaged by Finnie (see section 1.4.2), failed. Although large lips were raised by the impact, they remained firmly attached; the particles tended to roll on the surface and in no case was the lip removed by a single particle which did not fragment. It therefore appears that the process assumed by Finnie as a basis for his theory seldom occurs in practice.

Experiments at large negative rake angles (-70^{o}) did cause ploughing deformation; surface material was sheared in the direction of motion of the particle, and a shallow curved crater was formed, very similar to those formed by spheres and described above. A lip was raised at the end of the crater, and metal was also displaced to the sides.

An interesting feature of the lips raised at the end of the crater in the experiments with "cutting" geometry was the prescence of narrow shear bands; these

bands, very similar to those described above, were found passing through the bulk of the undetached lip. It seems likely, therefore, that adiabatic shear may play an important role not only in the ploughing deformation produced by spheres and particles impacting with large negative rake angles, but also in the cutting situation envisaged by many workers as being the most important mechanism of erosion.

Chapter Five

Effects of Particle Size and Density

5.1 Introduction

In an experimental study of single particle impacts, it is desirable to know the effects of particle size and density on the impact process. It is frequently useful to model the impact by using larger particles, which are not of the same density as the original erosive particles. In chapter 4, information on the process of metal removal was gained from sections of the impact sites, but such sectioning is only possible when the particles are larger than a few millimeters. It will be seen in chapter 6 that weight losses and crater volumes may be measured directly from single impact sites when the particles are larger than ~10 mm in diameter, but reducing the particle size to, say, 1 mm diameter diminishes the weight and volume loss by a factor of 1000, and renders them impossible to assess with accuracy.

In this chapter, the errors introduced by these scaling processes will be investigated. A simple model of the normal impact process, assuming a constant mean pressure under the indenting sphere, yields information about the effects of particle size and density on the strain rate involved in the impact. This will be discussed in section 5.2. An experimental study of the scaling laws has been made, and is presented in the rest of the chapter.

5.2 Constant dynamic yield pressure model

In this section we shall analyse the normal impact of a rigid sphere on a rigid, perfectly plastic half-space, making the simplifying assumption that the mean pressure under the indenting sphere is a constant, P. The problem has previously been discussed by Tabor (1951), who showed that these assumptions are reasonable for indentations in a fully work-hardened metal.

We consider the sphere to have mass m and radius r, and to strike the surface normally with initial velocity v. The volume of the indentation formed during impact may be simply deduced; since the retarding force on the sphere for any area of indentation A is given by PA, the work done by the ball in coming to rest is

$$\int_0^{x'} PA \, dx$$

where x' is the final depth of the indentation, x being its instantaneous depth. This work will be equal to the initial kinetic energy of the ball; hence

$$\tfrac{1}{2} mv^2 = \int_0^{x'} PA \, dx = PV \qquad (5.1)$$

since the volume V of the indentation is given by:

$$V = \int_0^{x'} A \, dx$$

We see therefore that

$$V = \tfrac{1}{2} \frac{mv^2}{P} = \tfrac{2}{3} \frac{\pi \rho r^3 v^2}{P} \qquad (5.2)$$

where ρ is the density of the sphere.

This simple model predicts that the volume of the crater will be proportional to the kinetic energy of the sphere; hence to the cube of its radius and directly to its density.

In a dynamic indentation, the effects of inertia of the deforming metal and of strain rate would be expected to influence the value of P ; we can extend the analysis further and examine, at least on an order-of-magnitude basis, the effects of r and ρ on the mean rate of strain during the indentation process.

If the chordal radius of the indentation formed at time t is a, and the depth of the indentation is x, then the projected area A is given by

$$A = \pi a^2 = 2\pi rx - \pi x^2 \qquad (5.3)$$

To simplify the analysis, we assume that $x \ll r$, so that we can put $\pi a^2 = 2\pi rx$, and the force decelerating the sphere becomes $2\pi Prx$. Its equation of motion is therefore:

$$m\ddot{x} = -2\pi Prx \tag{5.4}$$

whose solution for these boundary conditions is:

$$x = \frac{v}{\omega} \sin \omega t \tag{5.5}$$

where

$$\omega = (2\pi Pr/m)^{\frac{1}{2}} = \frac{1}{r}(3P/2\rho)^{\frac{1}{2}} \tag{5.6}$$

The sphere stops moving when $\dot{x} = 0$, that is, when $\omega t = \pi/2$; the time T taken to form the crater is therefore given by

$$T = \pi/2\omega \tag{5.7}$$

and is therefore independent of the initial impact velocity. The final depth of the indentation, x', is

$$x' = \frac{v}{\omega} \tag{5.8}$$

and so its chordal radius a is given by

$$a = (2rx)^{\frac{1}{2}} = (2rv/\omega)^{\frac{1}{2}} \tag{5.9}$$

Tabor (1951) has shown that a representative strain may be associated with the imprint of a spherical indenter, given approximately by

$$\varepsilon = 20\ a/r \tag{5.10}$$

where ε is the percentage strain. This relationship is empirically deduced for quasi-static indentations, and does not hold rigorously for values of a/r approaching unity, but we may assume that some similar relation, perhaps with a different constant of proportionality, will hold for the dynamic indentations we are considering. If we assume that the strain ε% is

developed in the time T, the strain rate may be approximated by $\varepsilon/100T$ i.e.

$$\dot{\varepsilon} \simeq 20\ (2rv/\omega)^{\frac{1}{2}} . \frac{2\omega}{100\pi r} \qquad (5.11)$$

Substituting for ω from equation 5.6 we find that

$$\dot{\varepsilon} \simeq \frac{2\sqrt{2}}{5\pi} . \frac{v^{\frac{1}{2}}}{r} . \sqrt[4]{\frac{3P}{2\rho}} \qquad (5.12)$$

While this equation must, from its assumptions, be very approximate, it illustrates the influence of v, r and ρ upon $\dot{\varepsilon}$. The radius of the particle, r, has the largest effect on the strain rate: reducing the size of the particle by a factor of ten increases the rate of strain tenfold. The influence of impact velocity and particle density is less pronounced; if we suppose that we take two spheres, with density differing by a factor of four, and with the initial velocity scaled by a factor of two to maintain a constant value of ρv^2, we find that the strain rate associated with the faster sphere is two times that with the slower. A numerical example will illustrate the influence of scaling. If we take v = 200 ms^{-1}, r = 50 μm and ρ = 3 Mgm^{-3} for a typical erosive particle, and P = 2 GPa for mild steel, we find that the rate of strain given by equation 5.12 is $\sim 1.6 \times 10^6$ s^{-1}. Suppose that the particle is scaled up and represented by a steel ball of radius 5 mm; since the density of steel is $\sim$8 Mgm^{-3}, we must use a velocity of $200 \times (3/8)^{\frac{1}{2}}$ ms^{-1} in order to maintain ρv^2 constant. Thus v = 122 ms^{-1} and $\dot{\varepsilon} \simeq 1 \times 10^4$ s^{-1}. Scaling the process by a factor of 100 in linear dimensions and replacing the material of the particle by steel has decreased the strain rate by a factor of $\sim$160.

Equation 5.12 would not be expected to hold for oblique impact, since equation 5.10 will not be valid, but a simple argument establishes the effect of particle size on strain rate for such impacts. Suppose the crater formed in the impact to be considerably longer than it is deep (say, 10 : 1, corresponding to an impact angle of $\sim 20^{\circ}$ - Finnie 1958). We assume that craters formed at the same velocity, by particles of the same density but of different sizes, are geometrically similar. The

pattern of deformation around the crater, ignoring the effects of inhomogeneity of the metal, will also be geometrically similar, and the "representative strain" for all sizes of particle will be a constant. The time taken to form a long shallow crater is proportional, we argue, to the length of the crater, divided by the particle velocity (constant). The mean strain rate associated with the formation of the crater is therefore inversely proportional to the length of the crater, and hence inversely proportional to the particle size. The same dependence on r is predicted by equation 5.12; it is therefore reasonable to assume that this relationship will hold for all angles of impact. The dependence on v and ρ at oblique impact angles is not easily argued; we would expect, however, that $\dot{\varepsilon}$ would increase in some way with v at all angles.

5.3 Effects of particle density

5.3.1 Experimental

It has been shown (section 5.2) that for normal impact at least, a simple model predicts that spherical particles of the same size and kinetic energy (i.e. constant ρv^2) will produce craters of the same size. Since the strain rate is not a function of ρv^2, but of ρ and v separately, it is not clear to what extent this simple picture will be valid.

Experiments were performed to test these assertions for the case of oblique impact, and in particular to investigate the effect of varying the density of the sphere upon the shape and size of the crater lip.

Spheres of diameter 3.17 mm (1/8 inch) were used for these experiments, since spheres of different materials were readily available in this size. The materials used were ball-bearing steel (mass of ball 130.4 mg), synthetic sapphire (67.1 mg) and sintered tungsten carbide (249 mg). The densities ranged from 4.0 Mgm^{-3} for sapphire to 14.9 Mgm^{-3} for tungsten carbide.

The particles were accelerated using the gas gun described in chapter 3, with sabots as shown in figure 3.2a. Specimens were cut from 12.7 mm diameter cold drawn mild

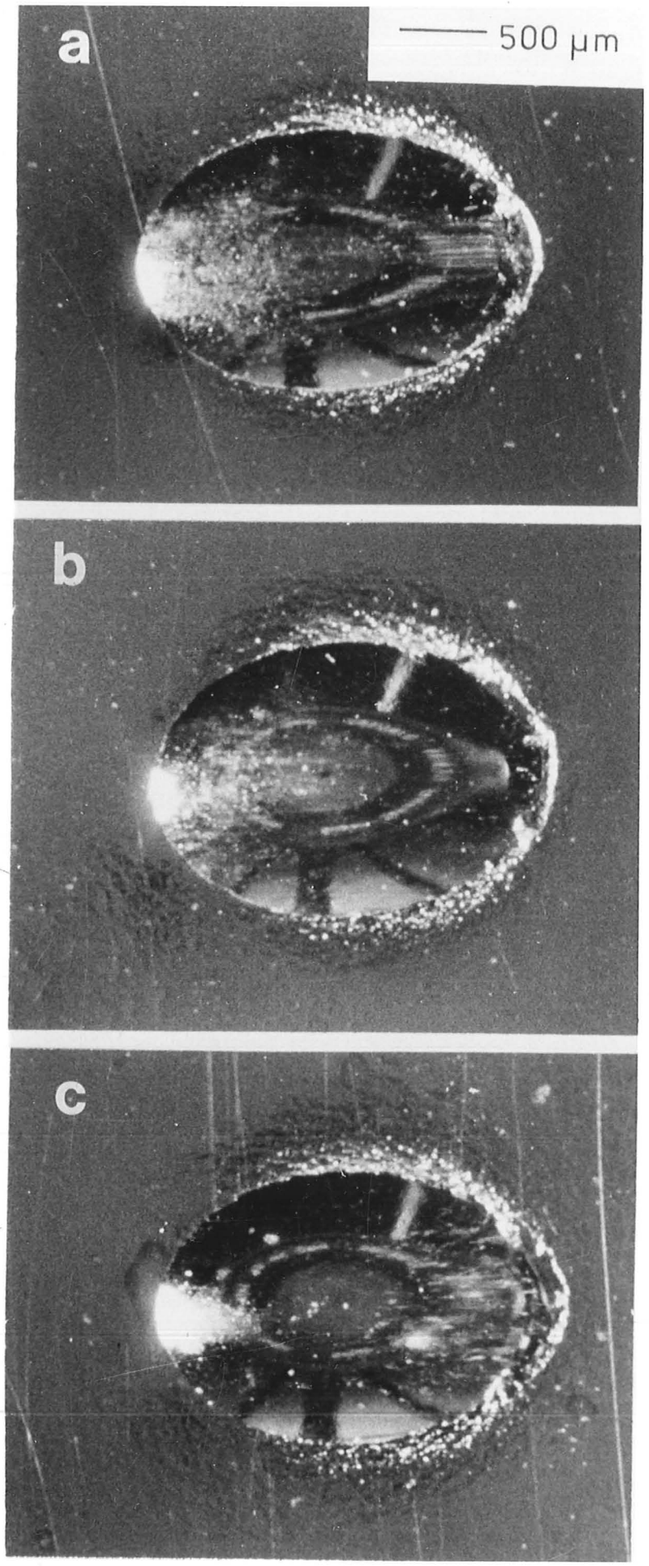

Figure 5.1
Impact craters formed in mild steel by 3.1 mm balls of different density and velocity at 25^{o} impact angle.
(a) Tungsten carbide ball, K.E. 1.89 J.
(b) Hard steel ball, K.E. 1.92 J.
(c) Synthetic sapphire ball, K.E. 1.85 J.

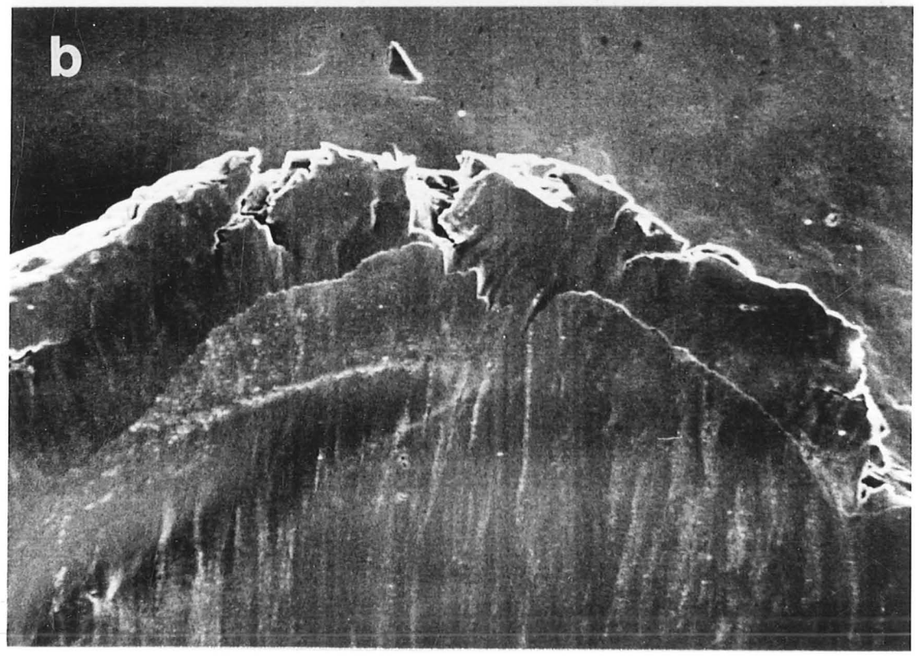

Figure 5.2
Scanning electron micrographs of the lip ends of craters formed in mild steel at 25^{o} impact angle by

(a) a 3.1 mm tungsten carbide sphere, energy 1.89 J and

(b) a 3.1 mm sapphire sphere, energy 1.90 J.

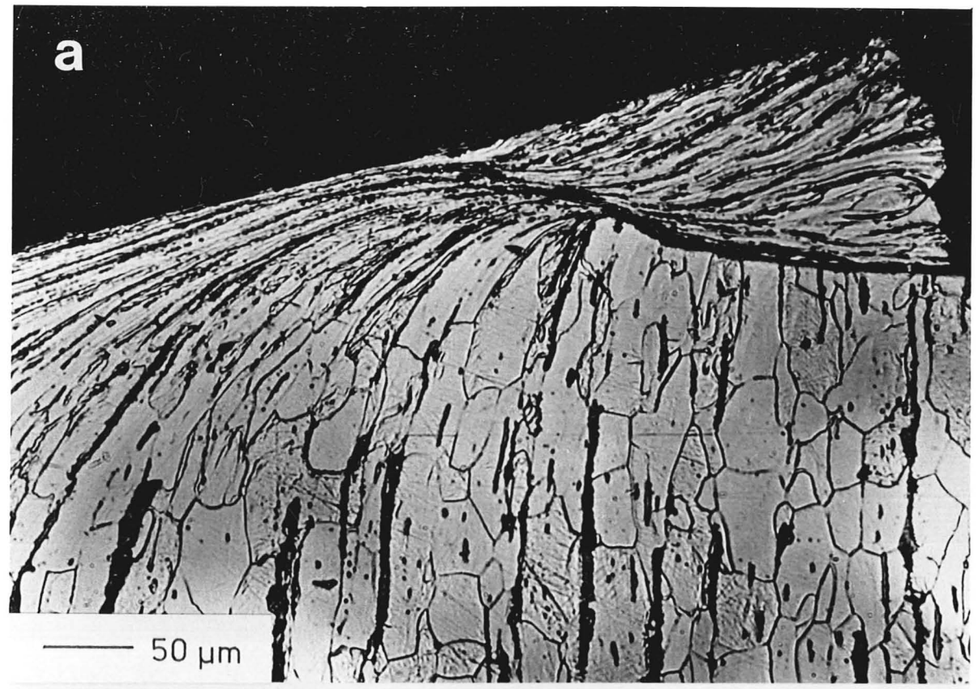

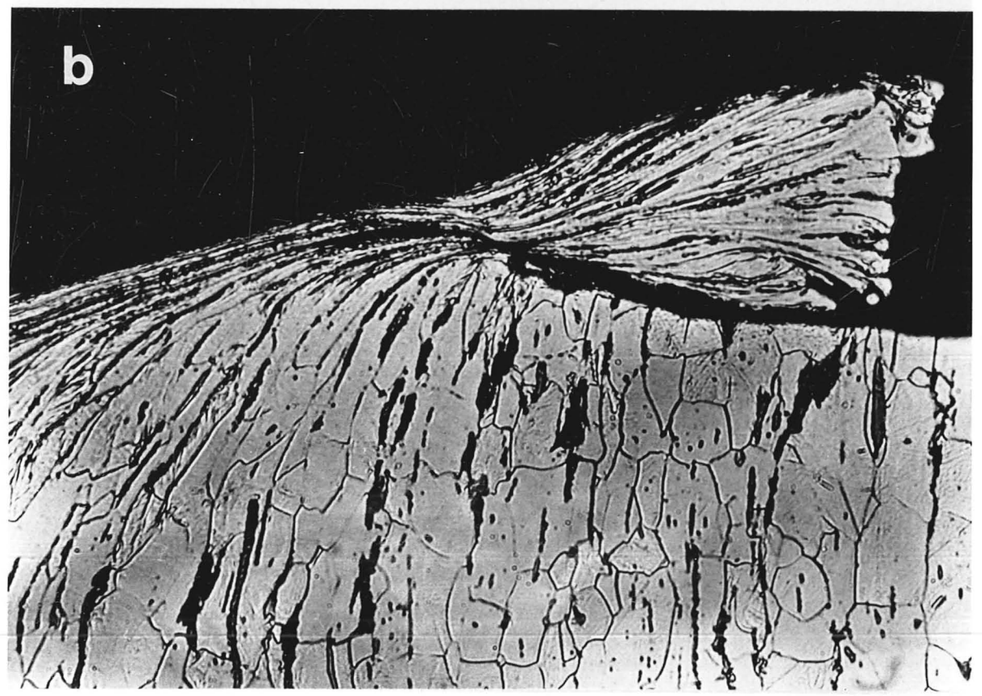

Figure 5.3
Etched longitudinal sections through the lips of craters formed in mild steel by the impact of 3.1 mm balls at 25°.
(a) tungsten carbide ball, energy 1.89 J
(b) sapphire ball, energy 1.90 J.

steel rod (En1A) and polished. They were clamped onto an angle block at the muzzle of the gun, the impact angle being held constant throughout the experiments at 25°.

5.3.2 Results

To study the lip morphology, an angle and velocity of impact known to give a pronounced, folded-over lip was chosen. This corresponded to a kinetic energy of the sphere of ~1.9 J; for the tungsten carbide sphere, the impact velocity was ~120 ms^{-1}, for the steel sphere, ~167 ms^{-1}, and for the sapphire sphere, ~233 ms^{-1}. The impact velocity therefore varied by about 2:1 between the sapphire and tungsten carbide balls.

Several impacts were made with balls of each material, to eliminate the possible effects of specimen inhomogeneity. In no case was deformation of the ball (plastic or brittle cracking) detectable after impact. The craters formed appeared superficially very similar. Figure 5.1 shows typical craters formed by the three types of ball; for ease of comparison, the kinetic energy of the ball is given in each case. No systematic variation of crater dimensions with ball density could be detected although there were differences of up to 3% in linear dimensions between individual craters.

Closer examination in a scanning electron microscope revealed differences in surface condition; figure 5.2 shows the lip ends of craters formed by tungsten carbide (a) and sapphire (b) balls with the same initial kinetic energy. There are signs of surface smearing, perhaps localised melting, in (b) which are absent in (a). Numerous microcracks and fissures are seen in the surface of the crater in (a) which were not seen in the crater formed by the sapphire ball (b).

The craters were sectioned longitudinally, and etched in 2% nital. Figure 5.3 shows the crater lips. The two photographs are very similar, both lips being of nearly the same size, and being separated from the bulk of the metal by a pronounced shear band, very similar to that described in section 4.5.1. The lip formed by the sapphire ball (figure 5.3 b) is perhaps less firmly attached than that formed by the tungsten carbide ball (figure 5.3a).

An estimate was made of the critical velocity at which the lips formed with the different balls became detached during impact. The values found were for the tungsten carbide balls, 155 $\pm$ 5 ms^{-1}, for steel, 205 $\pm$ 1 ms^{-1} and for sapphire 260 $\pm$ 3 ms^{-1}. The kinetic energies corresponding to these velocities are 3.00 $\pm$ 0.20 J, 2.74 $\pm$ 0.03 J and 2.27 $\pm$ 0.05 J, which are not the same within the limits of experimental error.

In several experiments with sapphire balls at various velocities, traces of metal were found adhering to the ball after impact. Care was taken to ensure that the ball had not struck any metal surface during deceleration after its initial impact on the target; the area of the metallic film was comparable with the contact area during impact. The metallic nature of the deposit was confirmed by a micro-chemical test. Phosphomolybdic acid ($H_3PO_4.12MoO_3$) in concentrated aqueous solution provides a non-specific test for metals (Feigl 1954). The reagent solution is a pale yellow; on contact with any metal a very intense "molybdenum blue" colour is produced. A small drop of this reagent applied to the surface of the ball showed the silvery deposit to be indeed metallic.

5.3.3 Discussion

The results of these experiments indicate that changing the density of an impacting sphere, but maintaining its kinetic energy constant, has little effect on the size and shape of the crater and lip formed during impact. The sections in figure 5.3 of craters formed by balls differing in density by a factor of four show no gross differences; it would appear that when the lips are removed, they would comprise nearly the same volume of material. Increasing the velocity, and hence the rate of strain (section 5.2) by two times has had little effect on the deformation process.

Differences are however visible on the surface of the craters (figure 5.2); the indentation formed at the higher velocity by the sapphire ball shows signs of much more surface flow and smearing than the low-velocity crater. Several microcracks or fissures are seen on the surface in figure 5.2a which are either not present or have been obliterated by surface flow in figure 5.2b.

The surface flow is directly associated with the higher sliding velocity; Bowden and Persson (1961) observed similar flow in a study of friction at high speeds under impact loading. A rise in temperature sufficient to cause softening in a thin surface layer has occurred; the abscence of any obviously melted droplets visible in the neighbourhood suggests that any actual melting which may have occurred will have been very localised. The difference between the craters formed by tungsten carbide and sapphire balls is probably not only caused by the difference in velocity of impact: sapphire has an appreciably lower thermal conductivity (1.9 $Wm^{-1}K^{-1}$) than tungsten carbide (4.5 $Wm^{-1}K^{-1}$), which would tend to increase the temperature rise at the sliding interface. The two materials may well have different coefficients of friction during the impact as well.

We have seen that craters formed by spheres of the same size and kinetic energy are very nearly identical in size and are surrounded by similar patterns of deformation. This would suggest that the distribution of strains around the crater, and especially at the base of the crater lip, is constant. The energy of the sphere at which the lip becomes detached during impact is not, however, constant, indicating that the lip does not detach when a critical strain is reached at its base. It seems likely, and may be argued from these observations, that a critical rate of strain is needed for detachment of the lip. Although strain and strain-rate are clearly not single-valued quantities for these complex deformation patterns, the way in which the energy of the sphere at which the lip detaches increases with sphere density suggests that strain rate might be important. We have seen in the previous chapter the importance of adiabatic shear in the mechanism of lip detachment. Clearly the temperature rise in a narrow shear band from which conduction is taking place will depend not only upon strain but also upon strain rate.

While the observation of metallic transfer to the sapphire balls during impact has little bearing on the question of scaling effects, it does illustrate one of the mechanisms of erosion suggested by Smeltzer et al.(1970). Smeltzer envisaged molten metal adhering to a rebounding particle; although the metal in this case has probably

not been melted, softening and surface flow has occurred, and the ball has plucked a certain amount of metal away from the surface. Similar adhesion and transfer is commonly observed in sliding, especially at high loads (Bowden and Tabor 1950), but it is doubtful whether such transfer of metal can account for more than a very small fraction of observed erosion rates. Certainly in this case the volume of the crater lip is many times that of the thin film transferred to the ball.

5.4 Effects of particle size

5.4.1 Experimental

It has been shown by several workers (see chapter 1) that the erosion caused by many particles does depend to a certain extent on the size of the erosive particles; we would not therefore expect in this study to find a weight loss directly proportional to the mass of the particle over a wide range of sizes. The purpose of this work was rather to establish that the deformation occurring in the impact of large spherical particles (of millimeter dimensions) was qualitatively the same as that produced by small spheres of size similar to those found in practical erosion situations.

Spherical particles of the same material which are harder than mild steel are not available in a wide range of sizes; the effect of size scaling was studied with tungsten carbide spheres of 3.1 mm and 356 μm diameter, and tungsten spheres of 89-104 μm diameter (sieve sizes). The particles were accelerated with the gas gun described previously, and their velocities were measured photo-electrically. The velocity and angle of impact were chosen to give a raised lip at the end of the impact crater of the type observed in the first part of this chapter; the velocity was scaled, using the results of that part, to maintain a constant value of ρv^2 for the spheres of different density. The targets were of cold-worked mild steel (En1A) and were clamped to an angle block at the muzzle of the gas gun.

Figure 5.4
Scanning electron micrographs of craters
formed at 25^{o} impact angle by
(a) a 3.1 mm tungsten carbide ball at 117 ms^{-1}
(b) a 356 μm tungsten carbide ball at 117 ms^{-1}
(c) a 89 - 104 μm tungsten ball at 99 ms^{-1}.

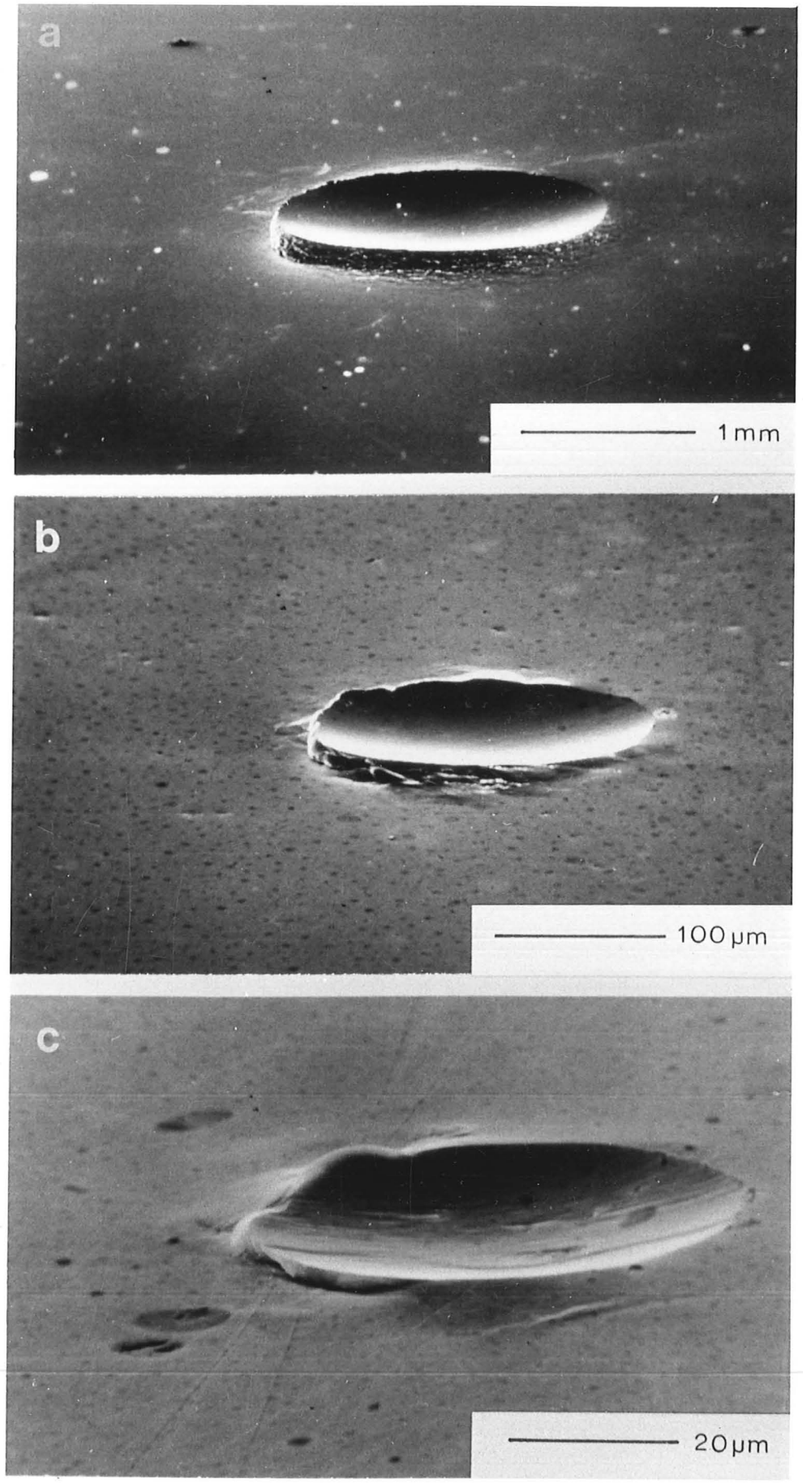

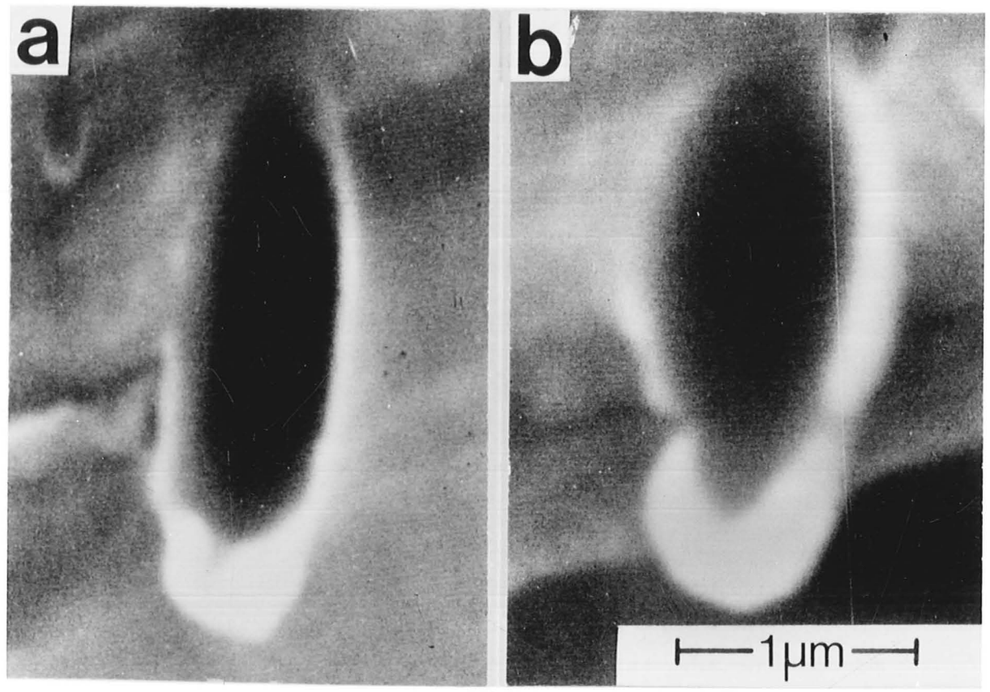

Figure 5.5
Impact sites in indium formed by carbonyl iron particles (round) of ~1 μm diameter accelerated electrostatically to ~150 ms^{-1}
(a) 15^{o} impact angle
(b) 25^{o} impact angle.
(from Winter 1971)

5.4.2 Results

Figure 5.4 shows scanning electron micrographs of craters formed by the 3.1 mm, 356 μm and 89 - 104 μm spheres at velocities of 117 ms^{-1} (tungsten carbide balls) and 99 ms^{-1} (tungsten balls) at a constant impact angle of 25°. The overall lengths of the craters formed by the three different sizes of ball were 1.83 mm, 199 μm and 54.5 μm.

5.4.3 Discussion

It is seen in figure 5.4 that the general form of the craters and extruded lips is very much the same over this range of particle size. Figure 5.5 shows scanning electron micrographs of craters formed in indium by iron spheres of ~1 μm diameter (Winter 1971); prominent lips are formed at the exit ends of the craters, and the general form of the deformation differs little from that seen with 9.5 mm diameter balls in chapter 4.

One difference to be seen in figure 5.4 is the increase in irregularity of the crater outline with decreasing particle size. The lip formed in figure 5.4c is rather more irregularly shaped than that in figure 5.4a. This may be directly attributed to the finite grain size of the steel target material, the ferrite grains of which were typically 25 μm across. While the crater in figure 5.4a will have extended over many grains, and the metal may be regarded as effectively homogeneous, the deformation in figure 5.4c will have occurred in only a few grains, and differences in grain orientation will have produced local inhomogeneity in the metal. As the crater size becomes appreciably smaller than the grain size, it is expected that the material will behave in a more homogeneous manner again; the crater outlines in figure 5.5 are quite smooth in shape.

From the measurements of the craters in figure 5.4, the validity of linear scaling may be assessed. Although the sizes of the 3.1 mm and 356 μm particles are known with accuracy, there is an uncertainty of some 10% in the size of the particle which formed the crater in figure

5.4c. The lengths of the craters, expressed as fractions of the ball diameter, d, are then 0.58d, 0.56d and 0.56 $\pm$ 0.06d. We see that the deformation scales well, as predicted by the model in section 5.2; this might be expected, since large increases in indentation hardness only occur when the deformed volume approaches micrometer dimensions (see for example Gane and Cox 1970).

It is therefore concluded that the scaling of the ploughing impact process which is employed in this work does not introduce gross changes in the crater and lip formed in the impact. While the extrapolation of quantitative results may not be justified, the physical processes of metal removal by ploughing would be expected to remain unaffected by the scaling of particle size over the range involved in erosion.

The conclusions of this chapter may be expressed in the following way. It has been shown that for a fixed angle of impact, α, and radius of the sphere, r, the volume of the impact crater, V, is some function of the product ρv^2. Further, it has been shown that for a constant value of ρv^2, and of impact angle, the volume of the crater is proportional to r^3. We may therefore describe the volume of the crater by

$$V(r,\rho,v,\alpha) = r^3.f(\rho v^2).g(\alpha) \qquad (5.13)$$

where f and g are as yet unspecified functions.

Chapter Six

Measurements of Weight Loss in Single Impacts.

6.1 Introduction

While the qualitative results presented in chapter 4 give some idea of the way in which erosion by single spheres varies with impact angle and velocity, quantitative information is desirable for comparison with the results of multiple impact erosion tests, and with the predictions of the theories. In chapter 1 it was shown that although most theoretical treatments of erosion predict a dependence of weight loss upon the kinetic energy of the impacting particles, the experimentally determined velocity exponent is always greater than 2.0 and usually between 2.3 and 2.5. Information on the velocity exponent in single particle impacts will determine whether the flaw in these theoretical approaches lies in their assumptions about the single impact, or in their extrapolation to the case of multiple impacts.

Sheldon and Kanhere (1972) have measured weight losses resulting from single impacts of spheres; however, they have not made a quantitative comparison of their results with those of multiple impact (erosion) experiments, nor have they investigated the variation of weight loss with angle. Kleis (1969) has published the results of multiple impact experiments with round iron shot ($\sim$1mm diameter) on mild steel targets. The work to be described was carried out at suitable angles and velocities to enable a comparison with Kleis' results to be made.

6.2 Experimental

The specimen material used in this study was work-hardened mild steel (0.15% C, En1A, VPH 2.35 GPa), cold rolled in 16mm square section. The specimens were impacted on the side faces of the bar, prepared by final polishing with 600 grit silicon carbide paper. The spheres, 9.5 mm (3/8 inch) diameter, of ball-bearing steel, were accelerated using the gas gun described in chapter 3;

sabots as shown in figure 3.2b were used. The specimens were clamped to machined angle blocks at the muzzle of the gun. The angle of impact was thereby determined to within 0.5^{o}.

The target specimens were weighed before and after impact, and the mass of material removed in the impact was determined to within 0.1 mg. The volumes of the craters were measured in the following way. The lips raised around the crater were machined down to the level of the undisturbed metal, and the crater filled to this level with modelling material (Plasticine). The Plasticine (density 1.94 Mgm^{-3}) was then removed from the depression and weighed. The accuracy here was $\pm$ 7% in the worst case (the smallest volume measured); the method was found, with care, to give results reproducible in most cases to $\pm$ 3%.

6.3 Results

As shown in chapter 4, for some impact angles and velocities, no lip is detached in the impact, while at others, a lip is detached and recovered in one or two fragments. In such cases the lip fragments have been weighed and found to constitute 90-99% of the total weight lost by the specimen.

In figure 6.1, the weight losses resulting from the impact of single spheres impacting at 270 ms^{-1} are plotted against impact angle (solid line). The weight loss measured has been divided by the mass of the ball to yield a dimensionless parameter which can be directly compared with erosion values published by other workers. Although no large lip was detached at angles above 40^{o}, a detectable weight loss occurred, increasing slightly with impact angle. The scatter in experimental points at 25^{o}, 30^{o} and 35^{o} cannot be explained by uncertainties in velocity or impact angle; it must therefore be due to inhomogeneity of the target metal.

The erosion caused by spheres impacting at 30^{o} is plotted against velocity in figure 6.2. Again the weight loss is expressed as the dimensionless parameter. Below a critical velocity of $\sim$175 ms^{-1}, no weight loss could be detected, and the crater lip was still attached to the specimen. Above this velocity, lips were detached during

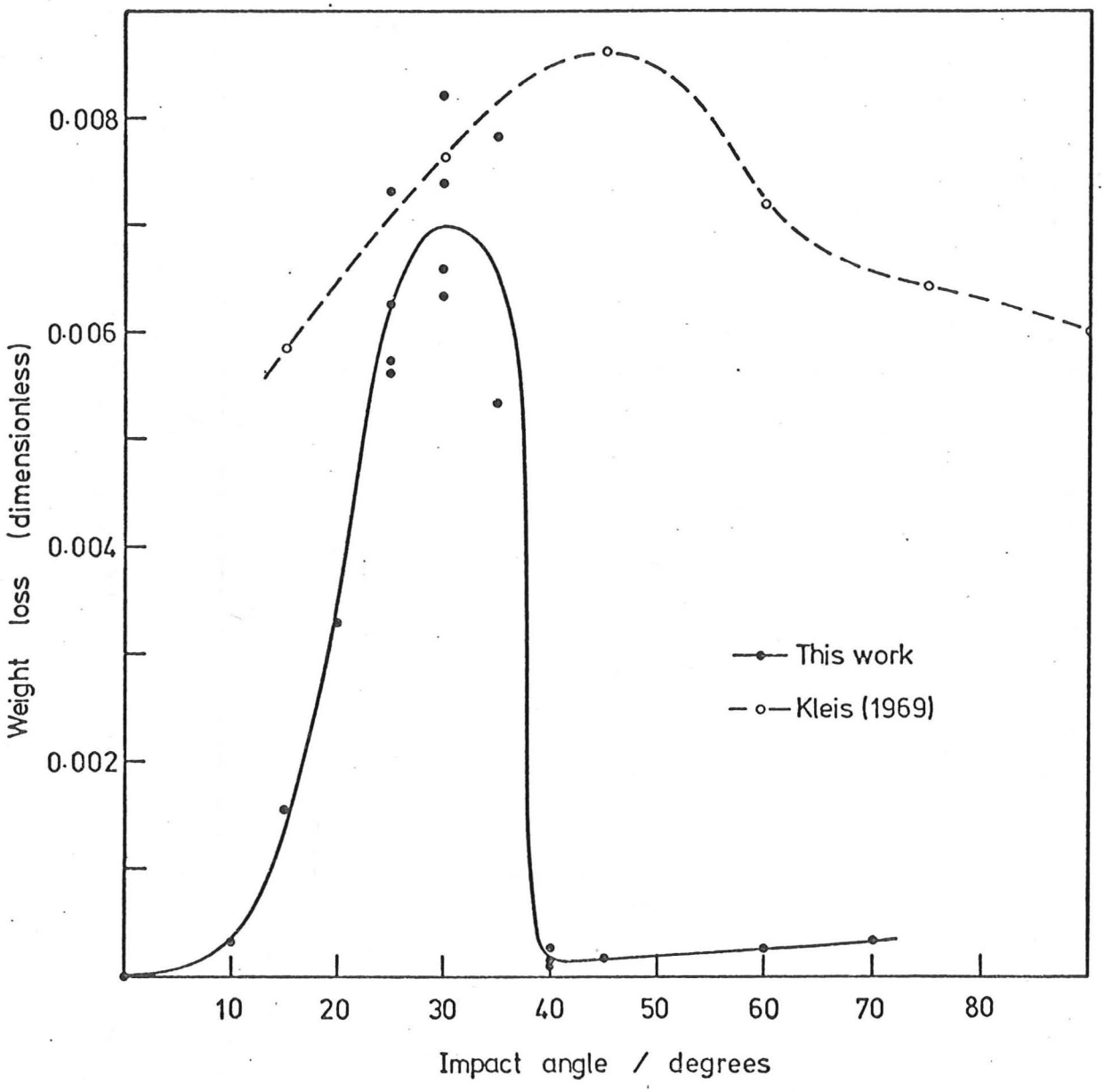

Figure 6.1
Weight loss in single impacts at 270 ms^{-1} plotted against impact angle (solid line). Kleis' results (Kleis 1969) for multiple impact erosion (dashed line).

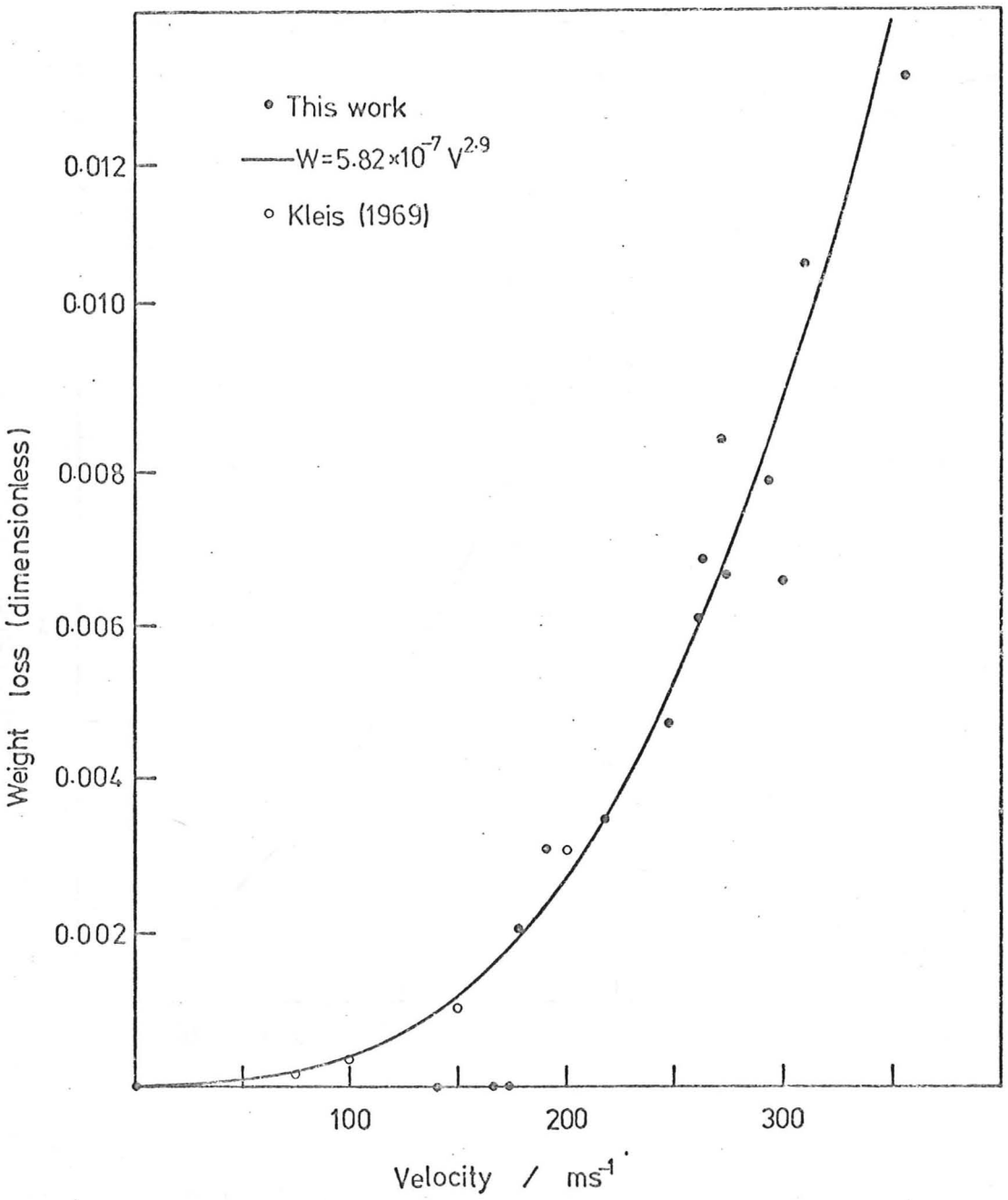

Figure 6.2
Weight lost in single impacts at 30° impact angle plotted against velocity of impact. 9.5 mm steel ball on mild steel. The actual weight loss has been divided by the weight of the ball to give the dimensionless parameter for comparison with Kleis' multiple impact results (open circles).

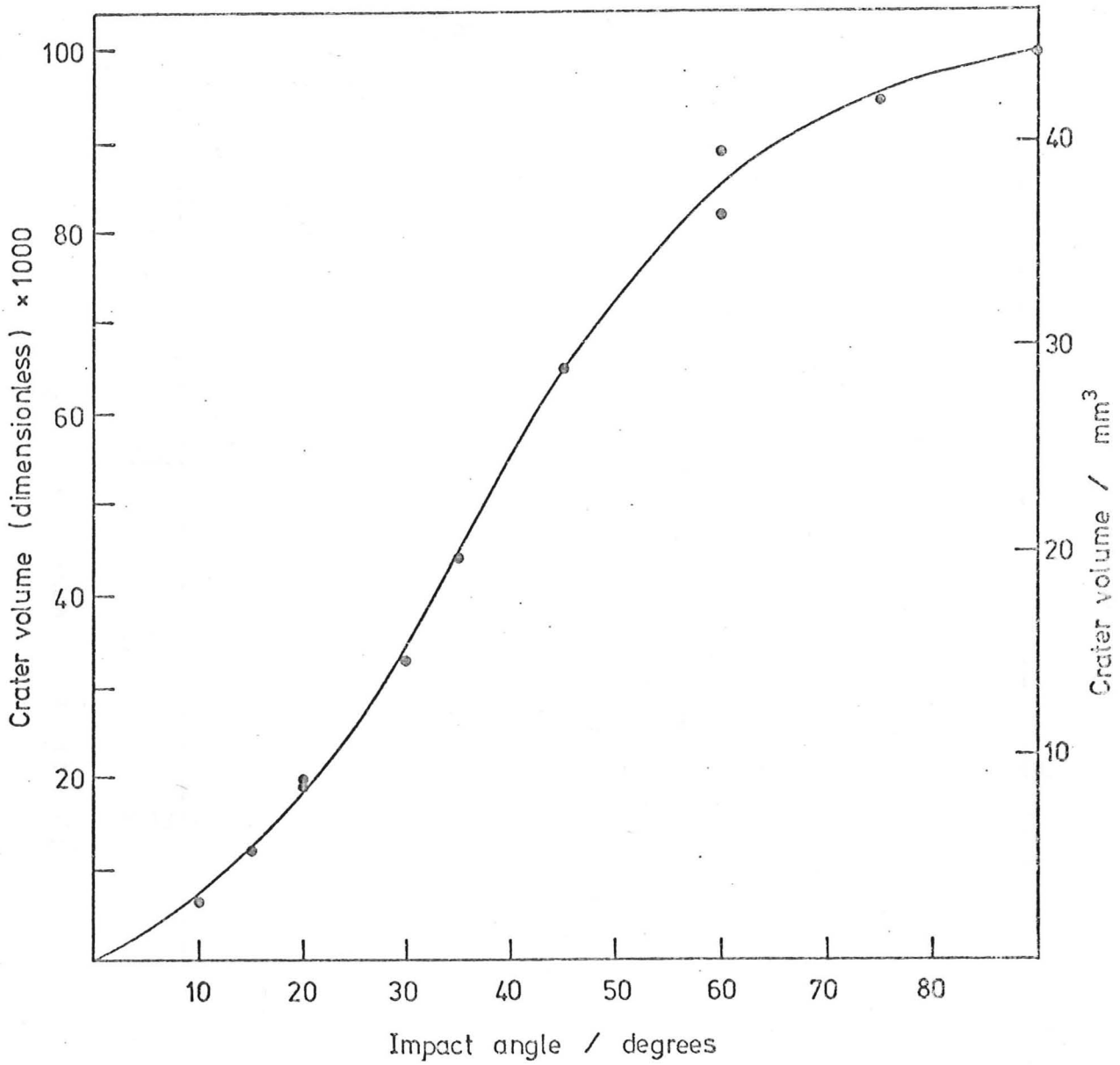

Figure 6.3
Crater volume plotted against impact angle for 9.5 mm steel balls striking mild steel at 270 $\pm$ 5 ms^{-1}.

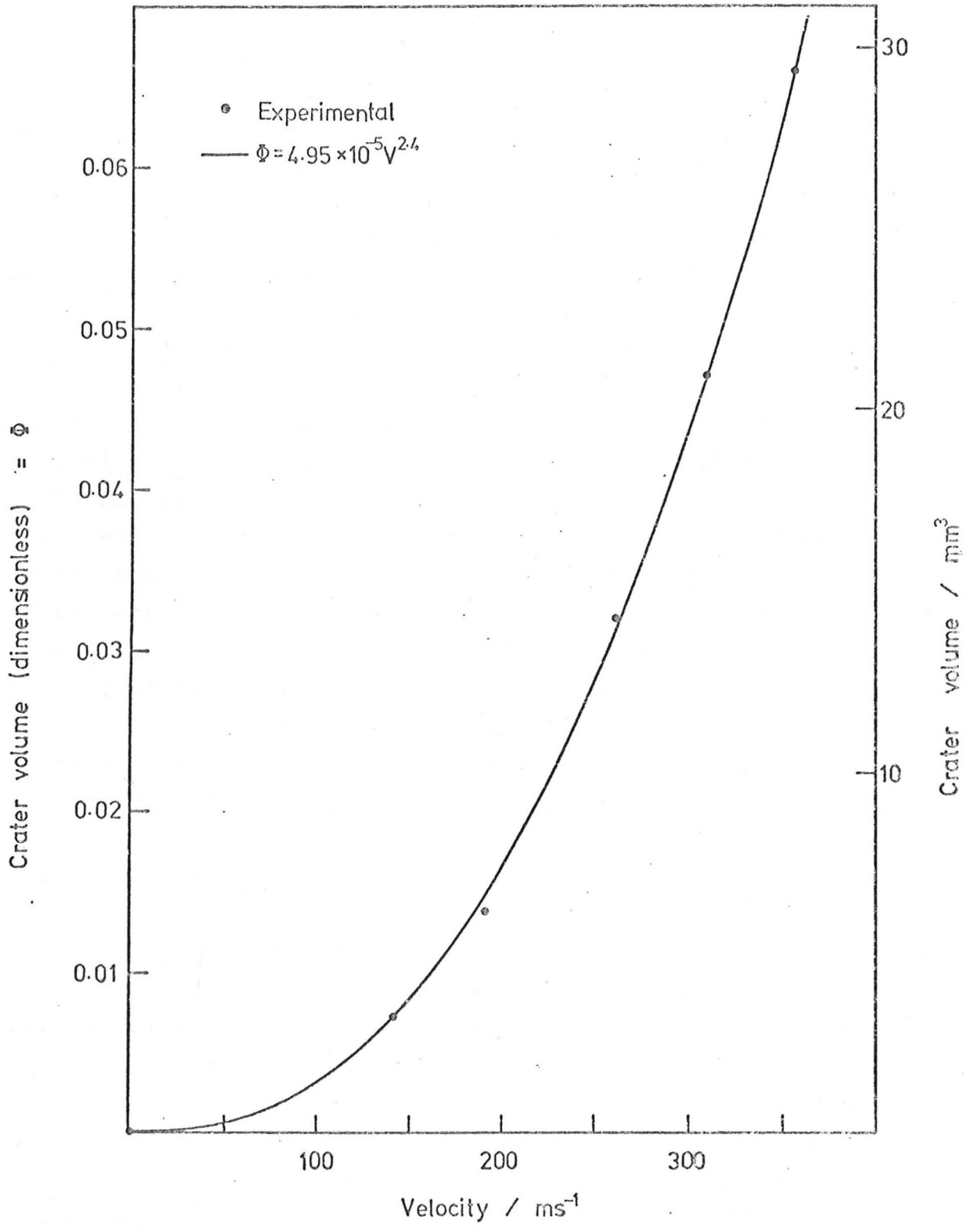

Figure 6.4
Crater volume plotted against impact velocity - 9.5 mm diameter steel balls striking mild steel at 30° impact angle.

impact, and measurable weight losses were recorded. The points on the graph corresponding to velocities above 175 ms^{-1} were plotted on a log/log scale, and found to lie close to a straight line of gradient 2.9. The solid line in figure 6.2 represents the relationship

$$W = 5.82 \times 10^{-7} v^{2.9}$$

where W is the dimensionless erosion parameter and v the velocity of impact (ms^{-1}).

The volumes of the craters formed at 270 ms^{-1} and various angles are shown in figure 6.3, and rise with increasing angle to a maximum at 90^{o}. The right-hand ordinate of this graph shows the volume in mm^3; on the left, this volume has been multiplied by the density of the specimen material and divided by the mass of the ball to yield a dimensionless volume parameter which can be compared directly with that plotted in figures 6.1 and 6.2. The variation of crater volume with velocity at a constant angle of impact of 30^{o} is shown in figure 6.4. The units of the ordinates are the same as in the previous figure. An empirical power-law equation may be fitted to these points; it is shown as the solid line and has the equation:

$$\Phi = 4.95 \times 10^{-5} v^{2.4}$$

where Φ is the dimensionless volume parameter and v is the impact velocity (ms^{-1}).

6.4 Discussion

Figures 6.1 and 6.2 illustrate the concept of critical angle and velocity discussed in chapter 4. For this specimen material, impacted at 30^{o} by 9.5 mm steel balls, the critical velocity is 175 $\pm$ 5 ms^{-1}, while for an impact velocity of 270 ms^{-1} there is a critical angle between 35^{o} and 40^{o} above which the crater lip is not removed. Separate experiments have shown that the critical angle and velocity are interdependent; as the ball velocity increases, the critical angle rises, and as the angle of impact is increased, so the critical velocity increases.

It was shown in chapter 4 that lips formed during the impact of spheres at oblique angles on mild steel tend to be separated from the bulk of the material by comparatively narrow and fragile necks. In multiple impact erosion, such lips could clearly be removed by the impact of other particles, even though they might not be removed

by the particle which formed them. The clearly defined critical velocity and angle observed with single impacts would not therefore be observed in multiple impact experiments. Since the masses of lips detached above the critical velocity lie close to the $v^{2.9}$ curve in figure 6.2, it is reasonable to suppose that the masses of those lips which were not detached would also lie on this curve. It is argued, then, that the multiple impact erosion results should lie on this solid curve, the velocity exponent being 2.9.

The results presented in figure 6.2 may be directly compared with the multiple impact experiments of Kleis (1969), who measured the weight loss of a 0.2% carbon steel impacted by spherical iron shot ($\sim$1 mm) at an angle of 30^{o}, using a whirling arm erosion rig. Although his results were obtained with particles of a different size, they may be directly compared with the points in figure 6.2 if they are expressed in terms of the dimensionless erosion parameter. It is seen that Kleis' results (open circles) for multiple impacts lie very close to the curve describing weight losses from single spheres. This result strongly supports the contention that single impacts might be used to assess the response of a material to multiple impacts by spherical particles.

The only published data on the angular variation of multiple impact erosion by spheres is that of Kleis (1969), who performed his experiments at a velocity of 120 ms^{-1}. Unfortunately, weight losses in single impact tests at this velocity were too small for accurate measurement. The experiments were therefore made at a velocity of 270 ms^{-1}. If it is assumed that the erosion weight loss will vary as $(\text{velocity})^{2.9}$, as shown above, and that this relationship will hold at all angles of impact, Kleis' results may be scaled up to a velocity of 270 ms^{-1}. A meaningful comparison can then be made with the results of the single impact experiments. In figure 6.1, weight losses in Kleis' multiple impact experiments, extrapolated to a velocity of 270 ms^{-1} (dashed curve) are shown for comparison with the weight losses resulting from single impacts (solid curve). In making this comparison, the lip mass rather than the mass actually removed must be considered, as discussed above. At impact angles greater than 40^{o}, lips are formed

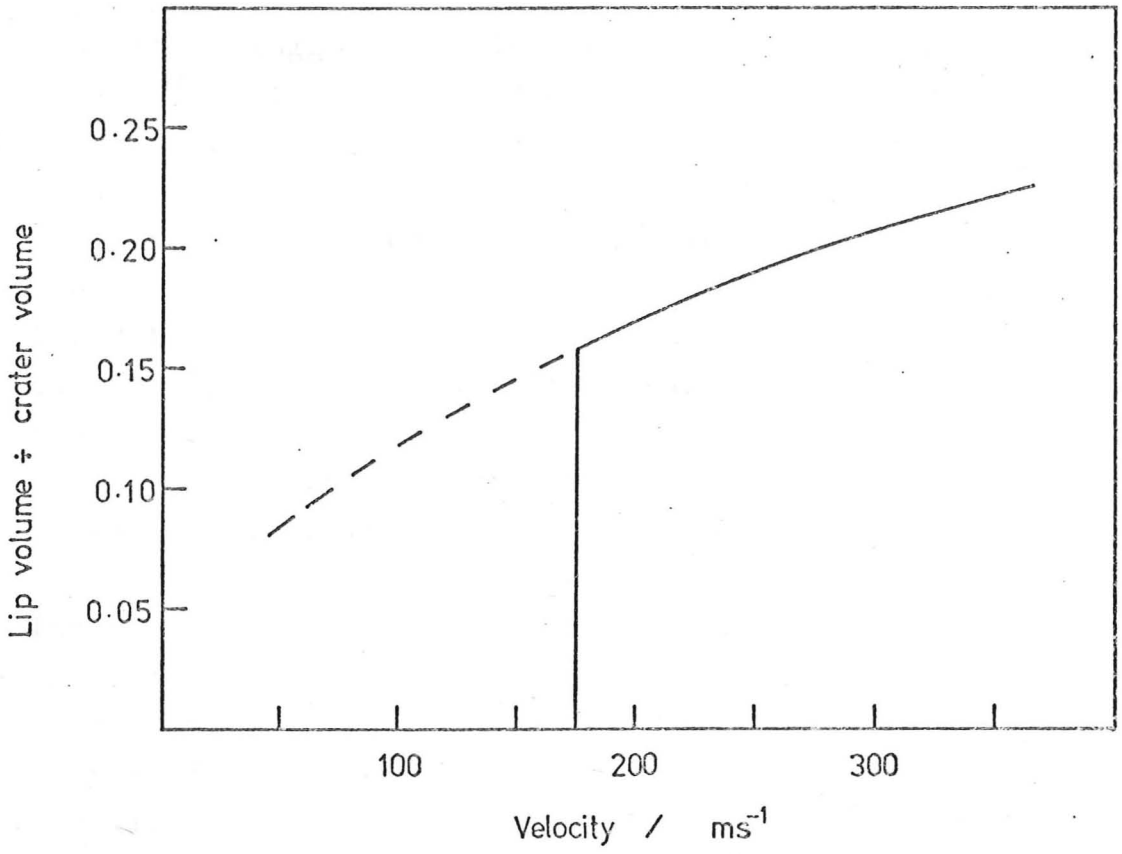

Figure 6.5
Volume of the crater lip / volume of the crater plotted against impact velocity - 9.5 mm steel balls striking mild steel at 30^{o}. The solid curve represents lips which were removed in the impact; the dashed curve is derived from the curve in figure 6.2 and represents lips which remained attached.

but not removed (see figure 4.6); it is argued that in the case of multiple impact erosion they would be removed. The single impact experiments were carried out on polished plane surfaces; in a practical erosion test, the surface would be roughened by previous impacts, and there would be a spread of impact angles due to this effect. For these reasons, it is suggested that the sharp peak observed in the single impact curve would be considerably broadened for multiple impacts; Kleis' results (dashed line) might be more closely matched.

There has been considerable disagreement among previous workers about the proportion of the material displaced by the particle which is actually removed from the target. Finnie (1958), Bitter (1963) and Sheldon and Kanhere (1972) all assumed that the whole volume of metal displaced by the particle will be removed, whereas Smeltzer et al. (1970) state that the proportion is $\backsim$0.3%. Since in these experiments both the weight loss and the volume displaced (i.e. the volume of the crater) have been measured, the ratio may be calculated. The fraction of displaced material found to be removed is plotted against velocity in figure 6.5. The broken curve shows the ratio between lip volume and crater volume for the cases where the lip remains attached. It is seen that at 50 ms^{-1} the lip volume constitutes $\backsim$1/12 of the total crater volume, and that this fraction increases to nearly $\frac{1}{4}$ of the crater volume at 400 ms^{-1}. The material displaced by the ball which is not formed into a lip causes deformation over a large volume around the crater (hinterland deformation as discussed in chapter 4).

It was considered possible that although the velocity exponent for weight loss is greater than 2, that for the crater volume might be 2.0, as predicted by the theories. Figure 6.4 shows it to be 2.4. There is therefore clearly an underlying error in the basic assumptions of the erosion theories about the process of impact.

The volume of the crater, for a constant impact velocity of 270 ms^{-1}, is seen to rise steadily with impact angle (figure 6.3) Such variation is not predicted by any of the theories; these, since they assume that a constant fraction of the crater volume is removed, must inevitably deduce that the crater volume reaches a maximum at the

same angle as the weight loss. These results show that none of the existing theories is capable of explaining the weight loss caused by the impact of a single sphere.

The results presented in this chapter indicate the nature of the functions $f(\rho v^2)$ and $g(\alpha)$ introduced in section 5.4.3. The experimental evidence that the crater volume is proportional to $v^{2.4}$ shows that $f(\rho v^2) \simeq (\rho v^2)^{1.2}$, and $g(\alpha)$ is the function depicted in figure 6.3. Equation 5.13 may now be written

$$V(r, \rho, v, \alpha) = r^3 . (\rho v^2)^{1.2} . g(\alpha)$$

6.5 Conclusions

The results of these single impact experiments compare well with those of multiple impact erosion tests, indicating that the processes of metal removal are probably the same in the two cases. It is suggested that the behaviour of a metal in single impact tests of this type may provide an indication of its performance under multiple impact erosion conditions, at least where the particles are spherical.

The velocity exponent of erosion found in this work was 2.9, and that of crater volume 2.4; the value 2.0 is predicted by all current theories of ductile erosion. The fraction of the crater volume which is removed by the impact is shown to vary substantially with velocity and angle of impact; this fraction has been assumed constant by previous theoretical workers.

It must be concluded that none of the theoretical treatments predicts the results of a single impact accurately, and their predictions cannot therefore be expected to extend to the case of multiple impacts and hence to erosion.

Chapter Seven

The Energy balance in single impacts

7.1 Introduction

It was shown in the previous chapter that the weight loss resulting from the impact of single spherical particles varies with (velocity)$^{2.9}$, and the volume of the crater with (velocity)$^{2.4}$. These results differ substantially from the variation of erosion and crater volume with velocity squared predicted by the theories. The theoretical prediction results from the assumption that a constant specific energy is required to remove unit mass of the target material, and that a constant fraction of the kinetic energy of the incident particles goes into removing material. In order to understand better the processes occurring during impact, some knowledge of the energy balance in the impact is required.

The incident sphere will have translational kinetic energy, and negligible rotational energy. During impact this energy is apportioned to plastic deformation of the target (crater formation), frictional heating due to sliding between the ball and target and kinetic energy of the ball (both translational and rotational) on rebound; a certain fraction of the initial energy will be dissipated in elastic waves in the ball and target. The final term may be shown to be negligible; Hunter (1957) has shown it to be so for the Hertzian impact of a sphere on the plane surface of a massive body, and Davis and Hunter (1960) have extended the argument to plastic impacts, provided that $T \gg d/c$. Here T is the impact duration, d is the diameter of the indentation and c is the velocity of longitudinal elastic waves in the specimen. For the experiments to be described, $d \simeq 5$ mm, and $c \simeq 5$ kms^{-1} implying that T must be much greater than 1 μs. We shall see from the photographic results that T is always greater than 20 μs, and we are therefore justified in ignoring the energy lost in elastic waves.

If we can measure the initial and final kinetic energy of the ball, we can then estimate how much energy has been lost in impact, and correlate this with the results of chapter 6. The technique of high-speed photography was used to make these measurements; although velocity may be measured in other ways, the detection of ball rotation was made very much more easily by the photographic method.

Studies were made of the energy absorbed in impact over a range of angles at 270 ms^{-1}, and over a range of velocities at 30^{o} impact angle, for comparison with the results of chapter 6. In addition, some measurements were made at other velocities and angles to provide more information about the dynamics of the impact process.

7.2 Experimental technique

The spherical particles were 9.5 mm diameter hard steel balls as used in much of the previous work, and were accelerated on polythene sabots with the gas gun described in chapter 3. The sabots were arrested at the muzzle by the block shown in figure 3.3. In some of the experiments a measurement of the angular velocity of the sphere after impact was needed; in order to provide a mark on the ball which would be visible in silhouette, a short copper tag was soft-soldered to the surface of the ball. This tag had, typically, a mass of 25 mg compared with the mass of the ball, 3.52 g. The position of the centre of gravity of the ball was therefore changed by the addition of the tag by ~35 μm, a negligible fraction of the radius of the ball (~5 mm). The heating of the ball involved in soldering the tag did not alter its properties significantly for the purpose of these experiments; after impact, no plastic deformation of the balls could be detected.

The specimens were cut from cold-rolled En1a mild steel bar (16 mm square) and polished, as described in section 6.2. In order that an unobscured view of the specimen surface could be obtained for photography, a clamping jig was constructed with this provision, which could be adjusted to hold the specimen rigidly at any

impact angle between 0 and 90°. The specimen clamp and the muzzle of the gas gun were enclosed in a thick-walled wooden protective enclosure, of internal dimensions 500 x 500 x 300 mm. This box had removable side panels for access, and 20 mm thick Perspex (poly (methyl methacrylate)) windows for photography and lighting.

A low-power helium-neon gas laser was used to align the system and to measure the angle of impact. During setting-up the beam was passed axially down the barrel of the gas gun, its central position within the barrel being ensured by passing it through small holes at the centre of removable plugs at each end of the barrel. The correct position of the specimen relative to the axis of the gun was ensured in this way. The laser beam, after specular reflection from the polished surface of the specimen struck the inside of the protective box some 300 mm away. The angle of reflection could be deduced from measurements of the position of the reflected spot; the angle of impact was measured in this way to better than 0.5°. The angle of rebound, that is, the angle between the particle velocity vector and the specimen surface, was measured in a similar way, by measuring the position of the impact scar on the inner surface of the wooden box. A similar accuracy ($\sim 0.5^{\circ}$) was obtained for this measurement.

The initial velocity of the particle was measured using the photoelectric timer described in section 3.5; it is certainly known to within 1%. The velocity of rebound of the ball was determined from measurements on the high-speed photographs which will be described in section 7.4.1.

7.3 The high speed photography

7.3.1 The camera

An "Imacon" image-converter framing camera was used for this work, at a nominal framing speed of 5×10^4 frames per second (20 μs interframe time). The principle of operation of this camera has been described by Huston (1964), and will be briefly summarised here.

A conventional optical system forms an image on

the photocathode of a special image converter tube, containing three sets of deflector electrodes. The photo-electrons emitted from the cathode are accelerated by a high voltage (~20 kV) and focused to form an image on a phosphor screen. The visible image on this screen is then focused onto a photographic film by a relay lens, or may be viewed directly for focusing the camera. Between the photocathode and phosphor screen, the electron beam may be deflected in two directions and shuttered, by means of the deflector plates, so that by applying suitably varying voltages to the plates a sequence of pictures at evenly spaced time intervals may be displayed on the screen, and hence recorded on the film. The camera has the useful facility that the waveform-generating circuitry may be triggered by an electrical signal, and the camera will then start recording pictures after only a short delay (in this case 10 μs). Few other cameras have this facility, or provide results in so short a time, since the Imacon may be used with a 'Polaroid' film back.

Two types of photograph were taken with this camera: silhouette photographs in which the light source, impact site and camera were collinear were used to obtain quantitative information about the impact, and obliquely-lit photographs provided a qualitative view of the process of lip removal. The field of view for the silhouette photographs was ~40 mm square, and in the obliquely-lit cases about 20 mm square.

The majority of the photographs were taken using Polaroid type 47 film (3000 ASA speed) to record the phosphor images. Some tests were made with Kodak type 2485 high speed negative film. This was developed in Kodak MX 257 developer to give a speed of ~3000 ASA, and was used in the hope that it would give less film grain and better definition than the Polaroid process. It was found to yield no improvement, and was used for only a few photographs.

The triggering signal for the camera was provided by a breaking wire; a thin (100 μm) copper wire was stretched across the path of the ball, some 10 mm from the muzzle block and slightly away from the axis of the gun, so that the fragments would be swept aside by the ball and not intrude into the photographs. The trigger

pulse was delayed by the circuitry described in section 7.3.3, the camera and light source being switched on at suitable times after the wire had been broken.

7.3.2 The light source

For the framing speed and field of view used in this study, and with the high intrinsic sensitivity of the Imacon camera, a conventional photographic flashgun provided adequate illumination. A Braun EF 300 flash unit was used; in the silhouette photographs a thin paper diffuser was interposed between the flash tube and subject, which were ∿300 mm apart.

The flashgun is normally triggered by closing a pair of contacts; so that it could be triggered by a voltage pulse a simple auxiliary circuit was devised. The voltage pulse, applied to the base of a transistor, drove it into conduction, in which state current passed from the emitter of the transistor into the gate of a thyristor connected across the flashgun contacts, so triggering the flashgun. Using this circuit to trigger the light source its light output was measured with a high-speed photodiode (type BPY13). The light output was found to rise to a maximum some 40 μs after triggering and remain roughly constant for a further 250 μs. The light duration was therefore sufficient for at least 10 frames to be recorded with the camera at 20 μs intervals.

7.3.3 Delay circuitry

A block diagram of the control system used with the camera is shown in figure 7.1. The first delay unit, which was triggered by the breaking wire and provided output pulses to the light source and second delay unit, was developed for this work. The second delay unit was a standard Beckman and Whitley Model 511 control unit, which provided a suitable positive output pulse to trigger the Imacon camera. This second delay generator, which provides the delay for the light source to build up to full brightness, was set to give 50 μs delay for all the experiments.

Figure 7.2 shows the circuit of the first delay generator. The breaking wire feeds the Schmitt trigger

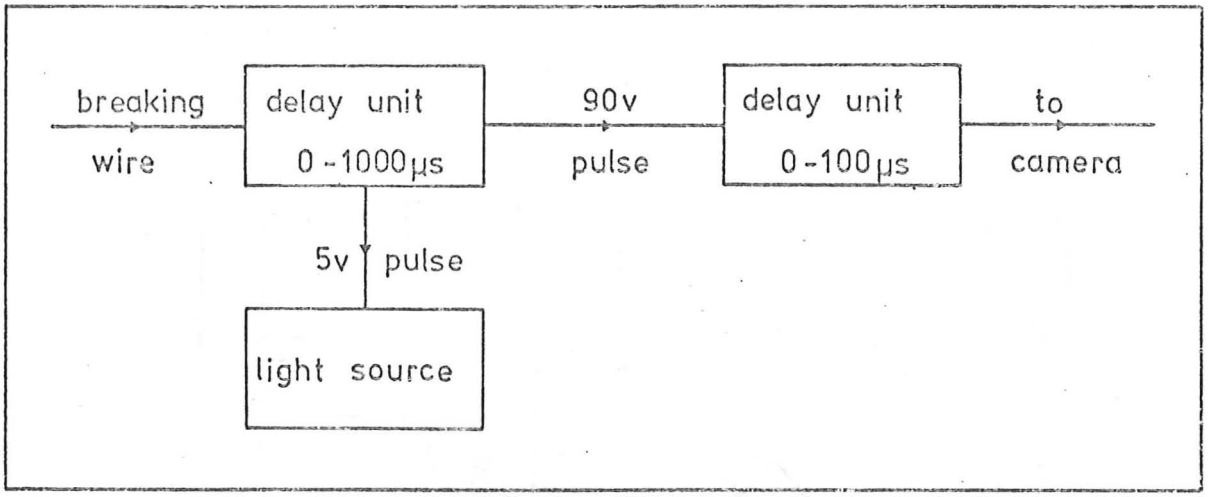

Figure 7.1
Block diagram of the control system used with the high-speed camera.

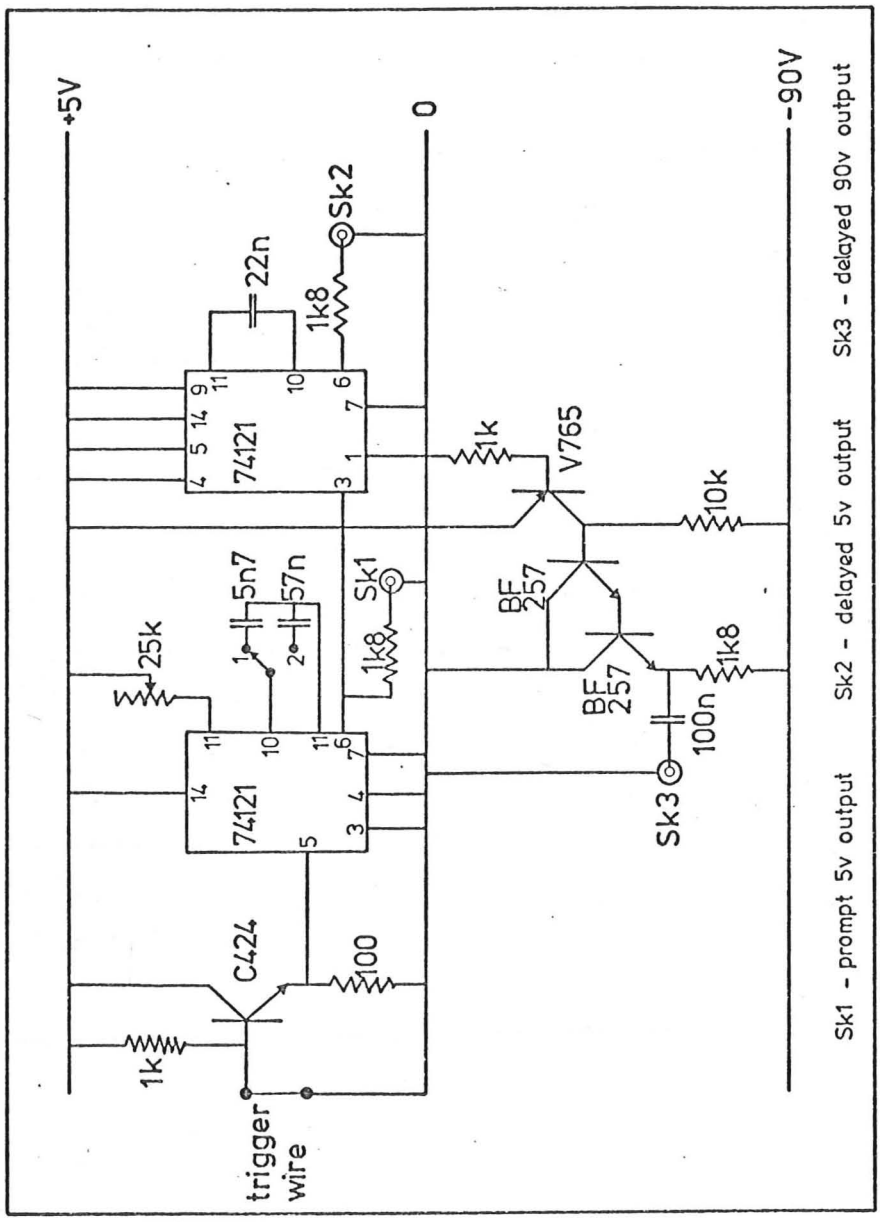

Figure 7.2
Delay circuit used to trigger the light source and camera after the breaking of a thin trigger wire in the path of the ball. The delay is variable between 0 and 1000 μs.

input of a type 74121 TTL monostable multivibrator, which provides the main timing delay. This delay is infinitely variable from 0 to 100 or 0 to 1000 μs depending on the position of the capacitor selector switch, the delay being set on a multi-turn potentiometer. The delay is repeatable to within 0.2%. After the preset delay time, the second 74121 monostable delivers a 5v, 2kΩ impedance pulse of width 35 μs to socket Sk2, and an amplified, 50Ω impedance 90v pulse to Sk3. The 5v pulse is used to trigger the flash unit, and the 90v pulse to trigger the second delay generator.

The first delay generator provides the bulk of the time interval between the ball breaking the trigger wire and the first photograph being recorded. Since the distance from the wire to the specimen surface was ~50 mm, delays of 100-500 μs were used, depending upon ball velocity.

7.3.4 Measurements from the photographs

From the silhouette photographs, measurements of the velocity of the ball after rebound and of its angular velocity were made. Typical photographs are seen in figure 7.3. Usually five to nine frames were recorded of the ball rebounding after impact. The photographs were enlarged photographically to approximately life-size, and the position of the ball measured relative to the edges of the frame to within 0.2 mm. From these x and y co-ordinates two mutually perpendicular velocity components were deduced and combined to yield the velocity of rebound. The magnification of the photographs was established from calibration photographs of a stationary graduated scale. The interframe time of the camera was measured with a timer (0.1 μs resolution) and found to differ substantially from the nominal value of 20 μs. The interval shortened slightly as the camera warmed up, but was always 19.0 ± 0.2 μs. The overall accuracy of the velocity measurements made in this way was ± 4%.

The angular velocity of the ball was measured by noting the rotation of the marker tag on the back of the ball (see figure 7.3a). This rotation was always small (~4°/frame); a realistic estimate of the overall accuracy of the angular velocity measurements would probably be ± 10%.

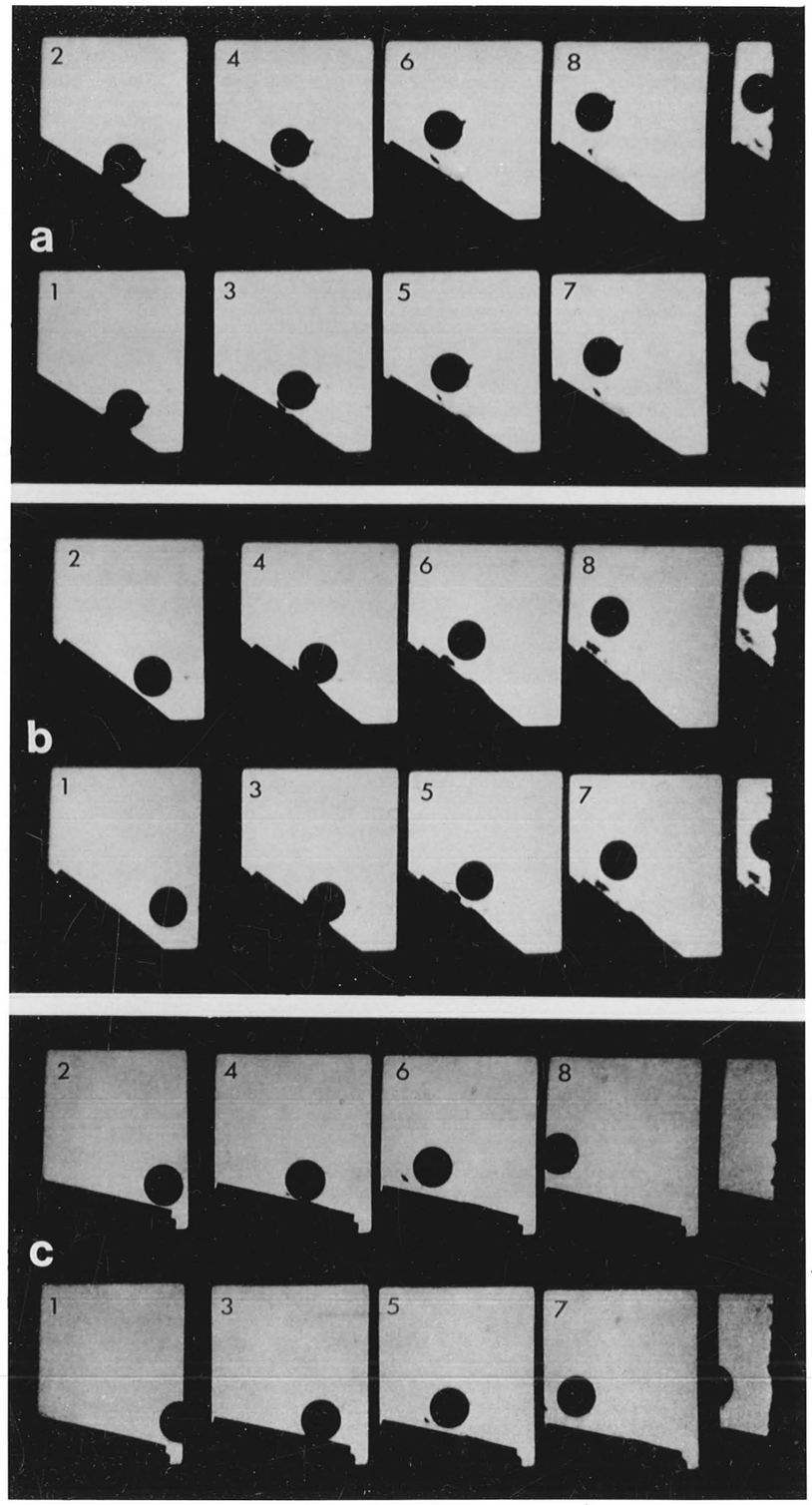

Figure 7.3
Typical sequences of high-speed photographs. Sequences (a) to (d) are silhouette photographs used for measurements of rebound velocity; (e) is an obliquely-lit sequence at a higher magnification. The diameter of the ball is in all cases 9.5 mm, the interframe interval 19 μs and the frames are numbered sequentially. Impact angles and velocities were:

(a) 30^{o}, 211 ms^{-1}
(b) 35^{o}, 274 ms^{-1}
(c) 10^{o}, 274 ms^{-1}
(d) 60^{o}, 276 ms^{-1}
(e) 20^{o}, 202 ms^{-1}.

Polaroid film was used for all these sequences.

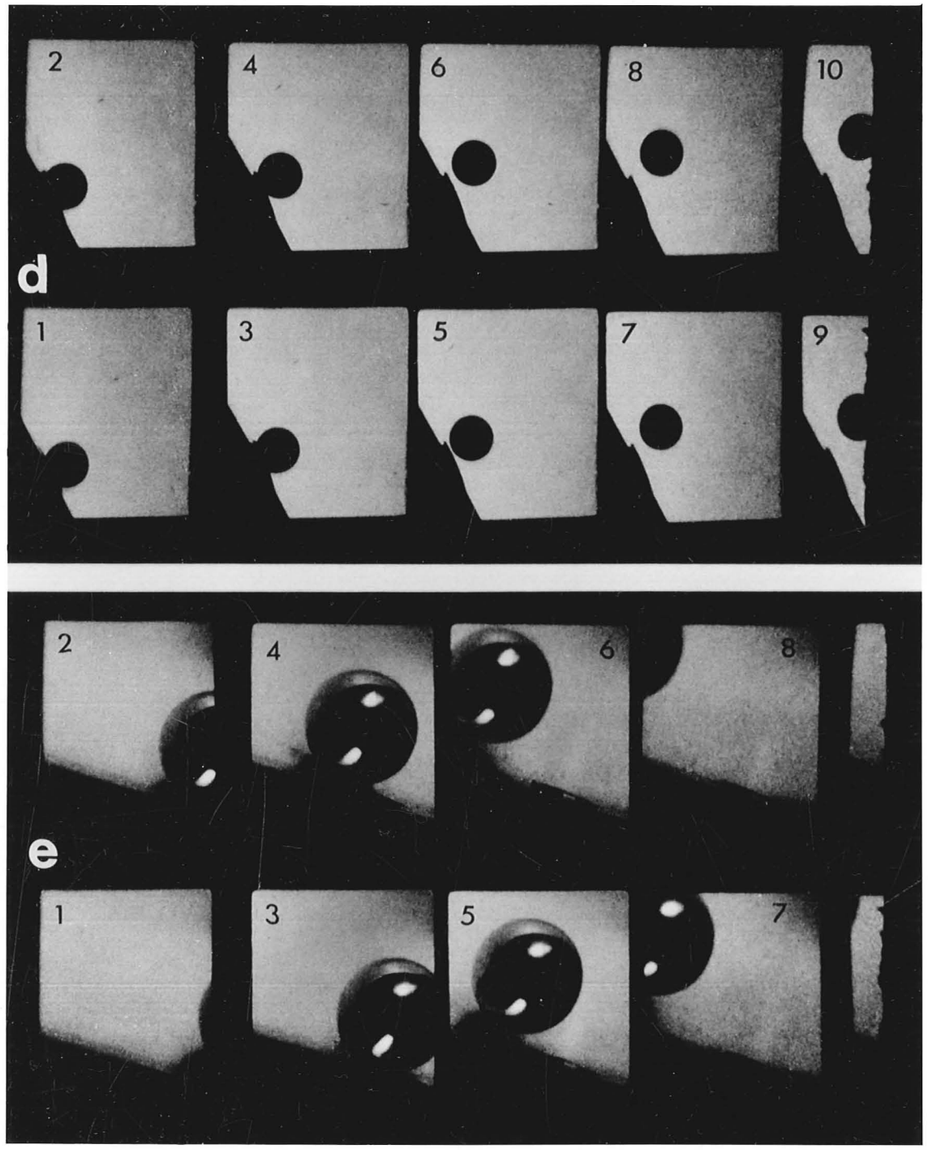
d
2
4
6
8
10
1
3
5
7
9
e
2
4
6
8
1
3
5
7

Figure 7.4
Examples of high-speed photographs obtained using oblique illumination. The ball is 9.5 mm in diameter, the film was Kodak type 2485 and the interframe time was 19 μs. The impact angle and velocity were
(a) 20^{o}, 210 ms^{-1}
(b) 20^{o}, 272 ms^{-1}.

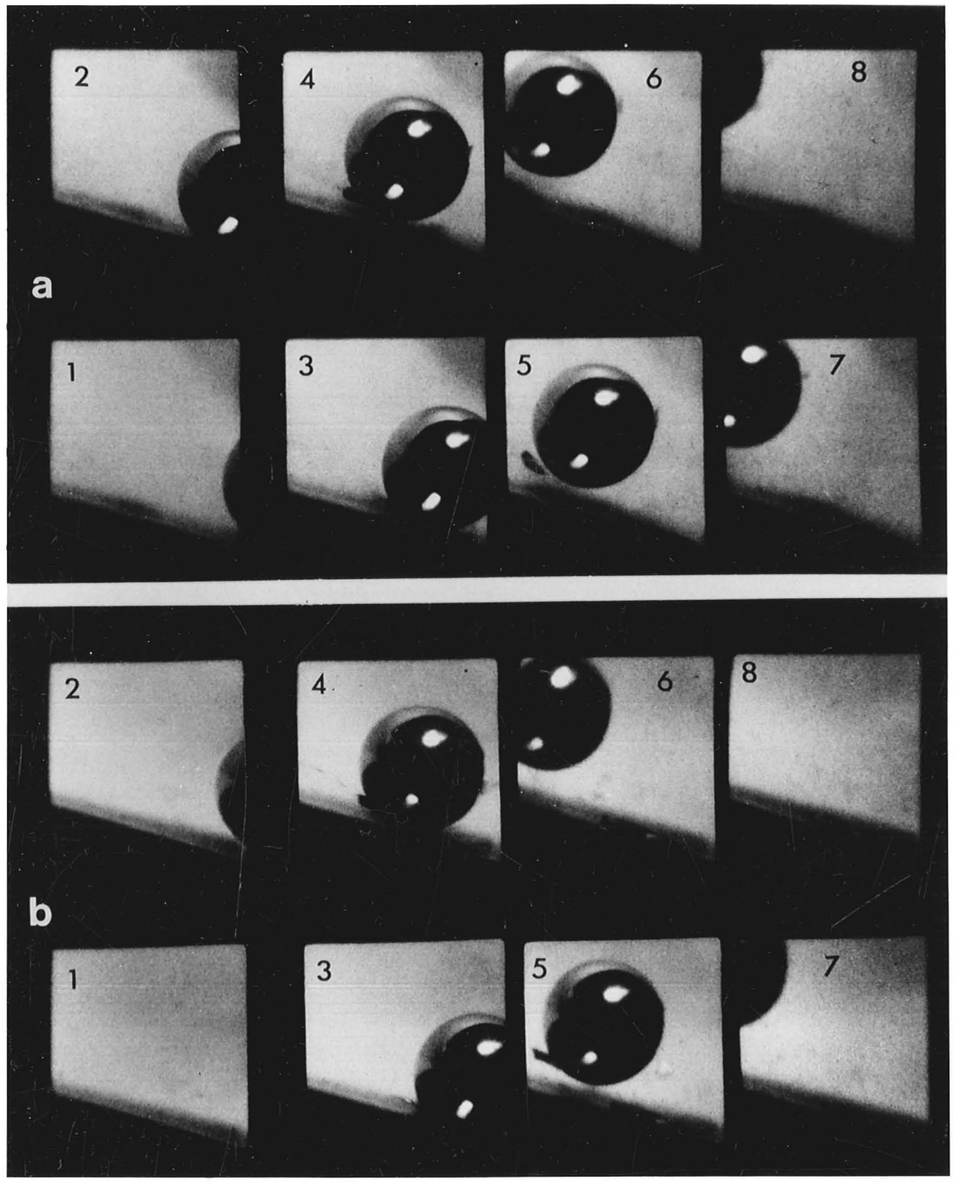

7.4 Results

7.4.1 Qualitative results

Figures 7.3 and 7.4 show typical sequences of high-speed photographs obtained with this apparatus. The light source was found to be of constant intensity for the ten frames taken, and good results were obtained with the synchronisation system used. The trigger wire was found to break in two places and the detached fragment often followed the ball through the field of view. Fragments of wire are just visible moving above the ball in sequences 7.3c and 7.3d. Experiments were made in which the trigger wire was mounted across the axis of the gun; in this case the wire stayed in front of the ball and obstructed the view of the impact site.

The Imacon camera is inherently very sensitive, and the light source therefore proved adequately powerful for the reflected light photographs at a higher magnification seen in figure 7.3e and 7.4. It is of interest to note that the definition and film grain in the photographs on Polaroid film are no worse than those obtained with 2485 negative film developed to give the same speed rating (3000 ASA); it was for this reason that Polaroid film was used for most of the sequences.

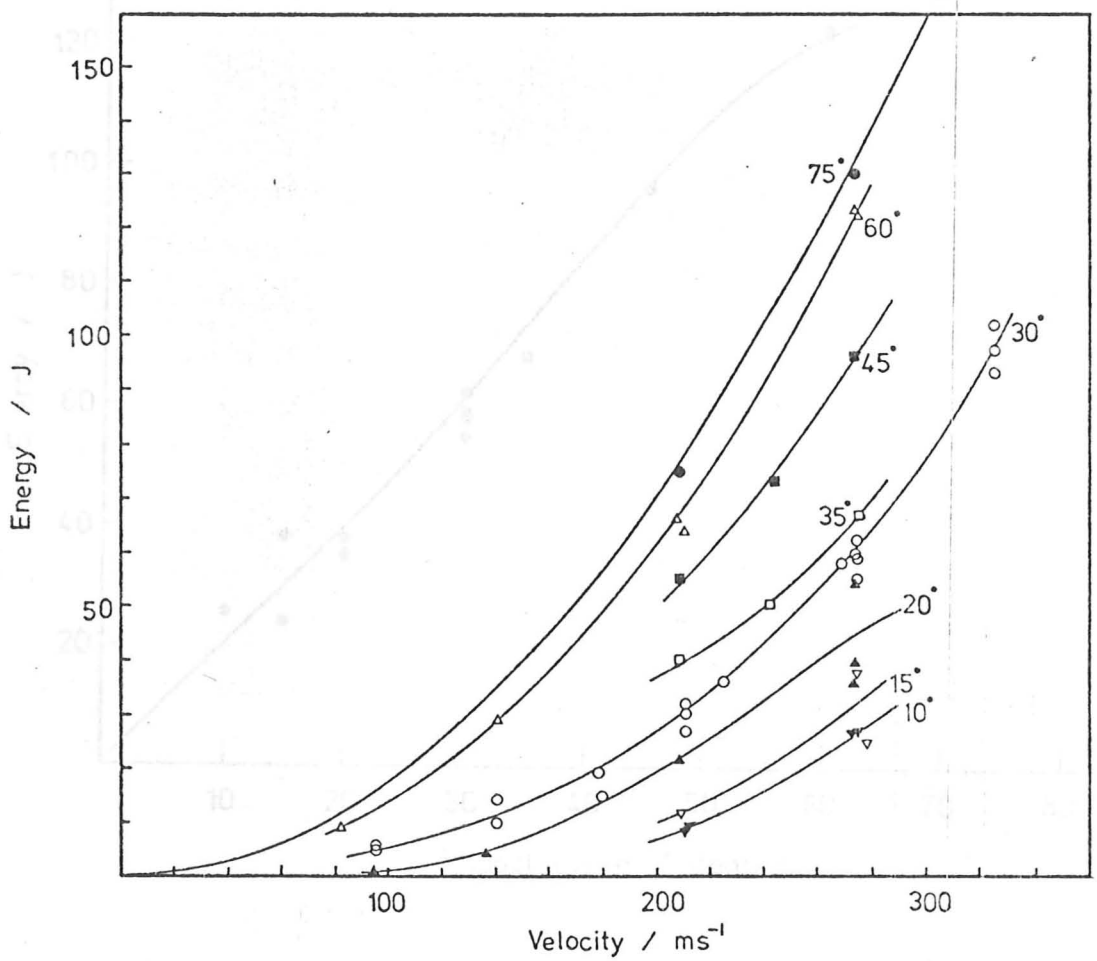

Figure 7.5
The kinetic energy lost by the ball during impact, plotted against initial (impact) velocity for the various angles of impact. The solid curve through the origin represents the total initial kinetic energy of the ball; the results of impacts at 90^{o} would lie almost on this line and are not shown.

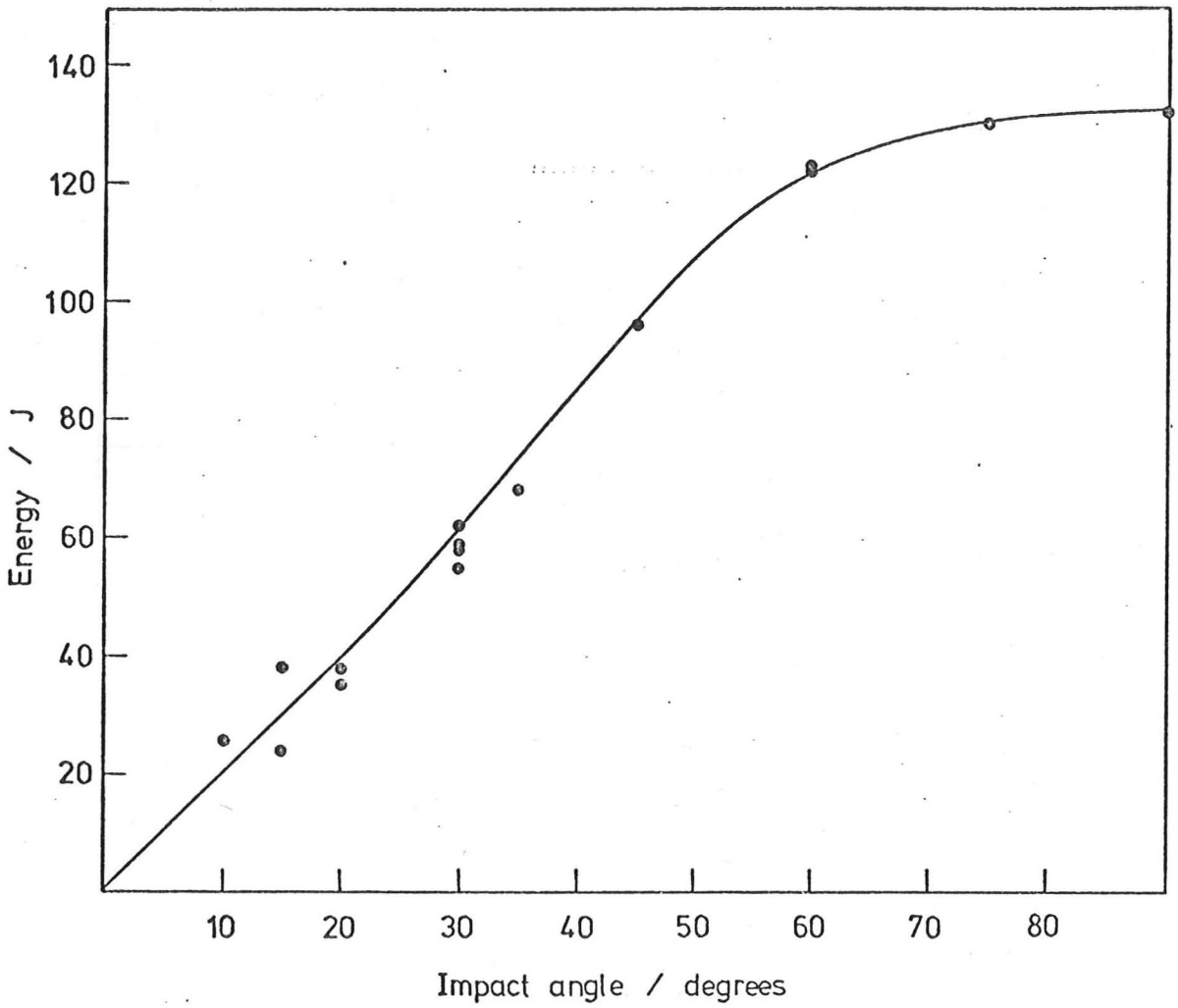

Figure 7.6
Kinetic energy lost by the ball during impact plotted against impact angle. The velocity of impact was 273 $\pm$ 3 ms^{-1}.

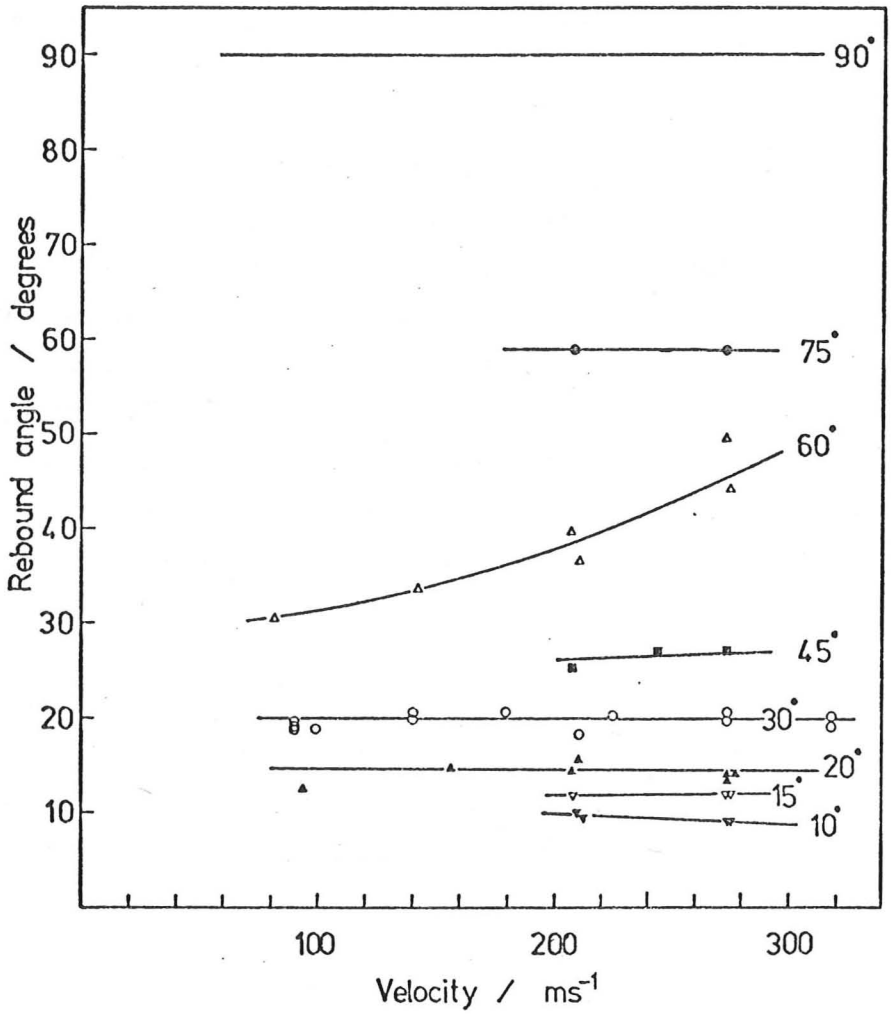

Figure 7.7
Rebound angle (β) plotted against impact velocity for the various angles of impact (α). Note that except at 90^{o}, the rebound angle is always less than the angle of impact.

7.4.2 Measurements of energy loss

The high-speed photographs were measured as described in section 7.3.4; the data available about each impact then comprised the initial velocity of the ball (u), the impact angle (α), the rebound velocity of the ball (v) and the rebound angle (β). In some cases the angular velocity of the ball after impact (ω) was also measured (section 7.4.3).

The principle aim of this work was in some way to correlate the energy lost by the ball in the impact with the information on weight loss and crater volume available from chapter 6; the kinetic energy lost by the ball during impact was therefore computed from the velocity measurements. Figure 7.5 shows the kinetic energy lost by the ball plotted against impact velocity (u) for a range of impact angles (α). The rotational kinetic energy of the ball after impact has been neglected; it was found to be always less than 1J (section 7.4.3). The solid curve passing through the origin in figure 7.5 represents the initial kinetic energy of the ball; the energy losses corresponding to the normal impact experiments would lie almost on this line, since the rebound energy at normal incidence was always less than 1.2J. Bearing in mind the relative inaccuracy of the rebound velocity measurement ($\sim$4% implying $\sim$8% in the calculated energy), the scatter of the experimental points is small.

In figure 7.6 the results obtained at impact velocities of 273 ± 3 ms^{-1} are plotted against impact angle (α). The energy lost in the impact is seen to rise almost linearly with angle to $\sim 60^{\circ}$, and then flattens off rapidly, the maximum energy loss being at normal incidence.

The angle of rebound (β) was measured for all the impacts, and was found in all cases except that of normal incidence to be less than the angle of impact (α). Figure 7.7 shows the measured rebound angles, plotted against velocity, for the various angles of incidence used. It is seen that the angle of rebound, for a given angle of incidence, is essentially independent of velocity, except in the case where $\alpha = 60^{\circ}$. For impacts at 60°, the rebound angle was found to vary significantly with impact velocity; as the impact velocity increased, so did the angle of rebound.

7.4.3 Ball rotation

In several experiments, the angular velocity of the ball after rebound was measured. A typical sequence of high speed photographs showing the marker used for these measurements is shown in figure 7.3a . The ball was loaded onto the sabot so that the marker tag would be at the rear of the ball and would not interfere with the impact process. The rotational velocity before impact was not measurable, while after impact it was never found to be more than $\sim 8^{o}$ per frame (= 7.3 krad s^{-1}). The moment of inertia of the ball was calculated to be 3.2×10^{-8} kgm^{2}; the kinetic energy of rotation corresponding to 8^{o} per frame is then 0.85 J. The rotational energy of the ball after impact was always less than 1% of the initial translational energy of the ball and was justifiably neglected in the calculation of the energy balance.

7.5 Discussion

7.5.1 Qualitative observations

The high-speed photographs in figures 7.3 and 7.4 confirm the mechanism of metal removal by ploughing deformation put forward in chapter 4. The lip becomes detached from the crater end during impact; it is seen that at the low angle of 10^{o} (figure 7.3c) a lip is still detached, while at 60^{o} impact angle (figure 7.3d), above the critical angle for this velocity, no fragments of metal are seen to be detached.

Figure 7.3a shows a sequence used for determining the rotation of the ball on rebound; the marker tag is clearly seen, and a slight rotation is visible.

7.5.2 Comparison of energy losses with weight losses and crater volumes

The points corresponding to an angle of impact of 30^{o} in figure 7.5 may be directly compared with the graphs of weight loss and crater volume versus velocity of impact (figures 6.2 and 6.4). To make this comparison, the energy lost by the ball to form unit volume of the crater lip, and unit volume of the crater, was plotted against velocity. Figure 7.8 shows these curves, which were generated by dividing the curve through the 30^{o} points in figure 7.5 by the experimental curves in figures 6.2 and 6.4. The energy to form unit crater volume at 30^{o} impact angle (left-hand ordinate) is seen to be approximately constant over the velocity range examined. The energy per unit lip volume (and hence per unit weight loss - right-hand ordinate) falls significantly with increasing velocity. This function is the same as the specific energy used in many theoretical approaches (see section 1.5); it is illuminating to note that even in the case of the single impact of a sphere, the energy absorbed per unit weight loss, at 30^{o}, is certainly not constant.

The variation of energy per unit crater volume with angle at a constant velocity may be deduced by

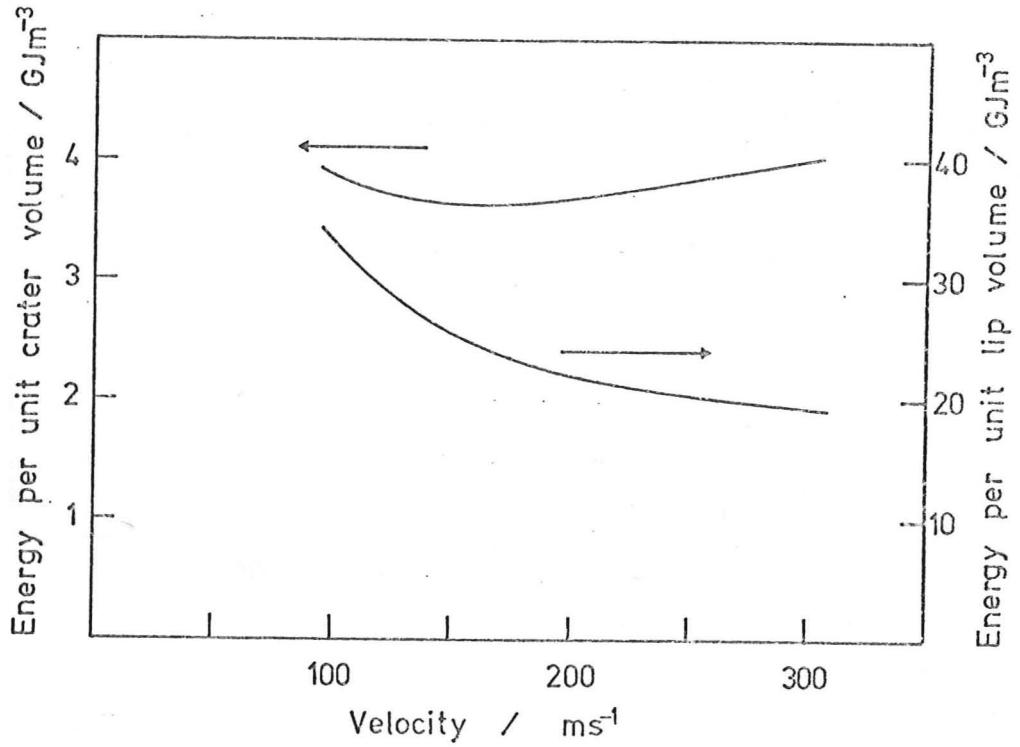

Figure 7.8
Energy absorbed in the impact for the formation of unit volume of the crater (left-hand ordinate, upper curve) and of the lip (right-hand ordinate, lower curve). The abscissa shows the impact velocity; the impact angle was 30^{o}.

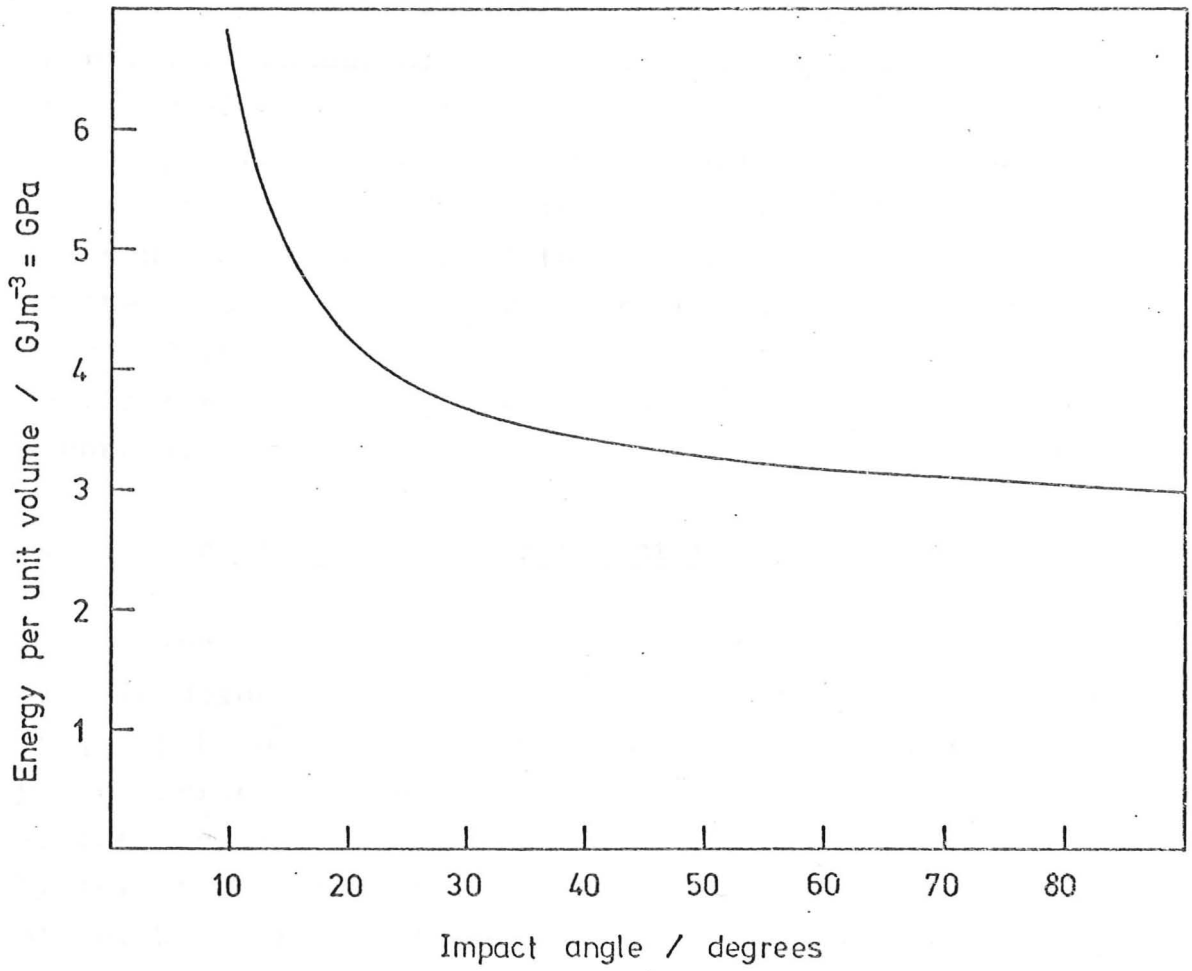

Figure 7.9
Kinetic energy lost by the ball per unit volume of the crater formed, plotted against impact angle for a constant impact velocity of 273 $\pm$ 3 ms^{-1}. 9.5 mm steel balls striking mild steel targets.

dividing the curve in figure 7.6 by that in figure 6.3. As may be seen in figure 7.9, this energy falls with increasing impact angle, the variation being very steep at shallow angles, and flattening off above $\sim 45^{\circ}$.

These measurements of energy loss show, then, that the energy required to form unit volume of the crater is nearly independent of velocity, implying that the energy absorbed in the impact varies as $(\text{velocity})^{2.4}$; this energy per unit volume, however, varies strongly with angle of impact, at 10° being twice its value for normal incidence. The volume of the crater lip, or the weight lost in the impact, is not simply proportional to the energy absorbed in the impact, nor to the kinetic energy of the incident particle, as assumed in the majority of erosion theories.

7.5.3 The dynamics of the impact process

The classical theory of impact, which allows for plastic deformation simply by a coefficient of restitution (e), may be applied to the problem of a sphere striking a plane surface (see e.g. Routh 1905). The case of a plastic sphere striking an elastic plane is not, however, distinguished by this theory from that of an elastic sphere on a plastic plane. While for small plastic deformation the classical theory will apply to both cases, at higher velocities the two will become significantly different, and the theory will no longer apply to the case of the elastic sphere on the plastic plane. A qualitative discussion of the impact process will illustrate this.

We consider the oblique impact of a sphere on a plane; the initial velocity and angle of impact are u and α, and the final velocity and angle of rebound are v and β. The ball has no initial angular momentum, and the coefficients of friction and restitution are μ and e respectively.

At sufficiently low impact velocities, the sphere and the plane both deform elastically. For normal impact, no energy is lost by the ball, all the energy stored in elastic deformation during impact being restored to the kinetic energy of the ball on rebound. $\alpha = \beta = 90^{\circ}$, and $v = u$. When $\alpha \neq 90^{\circ}$, the frictional forces between the ball and the plane come into play, giving a rotational

impulse to the ball during impact. Depending on the values of u and α, the ball may or may not stop sliding during impact; its final horizontal velocity component, v cos β, will as a result of the dissipation of energy in sliding be less than u cos α. The final vertical component, v sin β, will result from the elastic energy stored in the impact, as in the case of normal impact, and will thus be equal to u sin α. A certain amount of energy is dissipated in frictional heating, and we see that β will be greater than α.

At higher velocities, when the collision becomes plastic, e is less than 1, and energy is lost by the ball in plastic work. The vertical component of rebound velocity, v sin β, is now equal to eu sin α, and the horizontal component is less than u cos α because of frictional dissipation. At high velocities of impact, e will be small, and the angle of rebound may then be less than the angle of impact. The quantitative predictions of this simple theory will not be derived in detail; Routh (1905) derives them fully, and a readable discussion of their application has been presented by Daish (1972). The results, however, will be given.

Two cases may be identified: that in which the ball slides throughout impact (case I) and that in which the ball rolls off the surface (case II). The condition for rolling to occur, for the situation considered here, is that

$$(1 + e)\ \mu \tan\alpha \geq 2/7$$

We shall see later that $\mu \leqslant 0.05$ in the impacts being considered (section 7.5.4), and e is much less than 1. If we take $\mu = 0.05$ and neglect e, we find that rolling will only occur at impact angles higher than $\backsim 80^{\circ}$; for all the impacts studied, except at 90°, the equations pertaining to case I will apply. These are:

$$v \sin\beta = eu \sin\alpha \qquad (7.1)$$

$$v \cos\beta = u(\cos\alpha - (1+e)\ \mu \sin\alpha) \qquad (7.2)$$

and hence $$e \cot \beta = \cot \alpha - \mu (1 + e) \qquad (7.3)$$

When the results described in section 7.4 are analysed using these equations, it becomes apparent that the assumptions of this simple theory cannot be valid. Let us consider the impact of a ball at 30^{o} and 270 ms^{-1}. The coefficient of restitution, e, may be deduced from the rebound velocity at normal impact (see chapter 8) and is roughly 1/6 for the vertical velocity component involved in this example. Substituting these figures into equation 7.3 we find that β, the rebound angle, is $\sim 5^{o}$. We would also expect, from equation 7.3 and the observed variation of e with velocity (figure 8.3), that β would decrease rapidly with increasing velocity. Figure 7.7, however, shows these predictions to be badly in error; the experimentally determined value of β is about 20^{o}, and is independent of velocity over the range studied. Similar disagreement between the simple theory and the experimental result is found for the other angles of impact. An examination of the impact process, however, reveals the reason for this disparity.

Low values of rebound angle are deduced from the theory because the vertical component of the rebound velocity is assumed to be e times the vertical component before impact. For the case of a plastic sphere on an elastic plane, this may be a good approximation, but in the case of an elastic sphere on a plastic plane, there exists a mechanism by which horizontal momentum may be converted into vertical momentum. The end of the plastic indentation acts as a slope or ramp, being at an angle to the undisturbed surface of the metal; the reaction force on the ball, being normal to this slope (ignoring friction) will have a vertical component. We can see now how the large vertical component of rebound velocity arises. Only a part of it is derived from elastic forces, the remainder resulting from this conversion of horizontal to vertical translational momentum. The importance of this effect is shown in figure 7.10. Here the kinetic energy associated with the vertical component of the rebound velocity ($E_f \sin^2 \beta$) is plotted against velocity for a range of impact angles. The points obtained at normal impact show

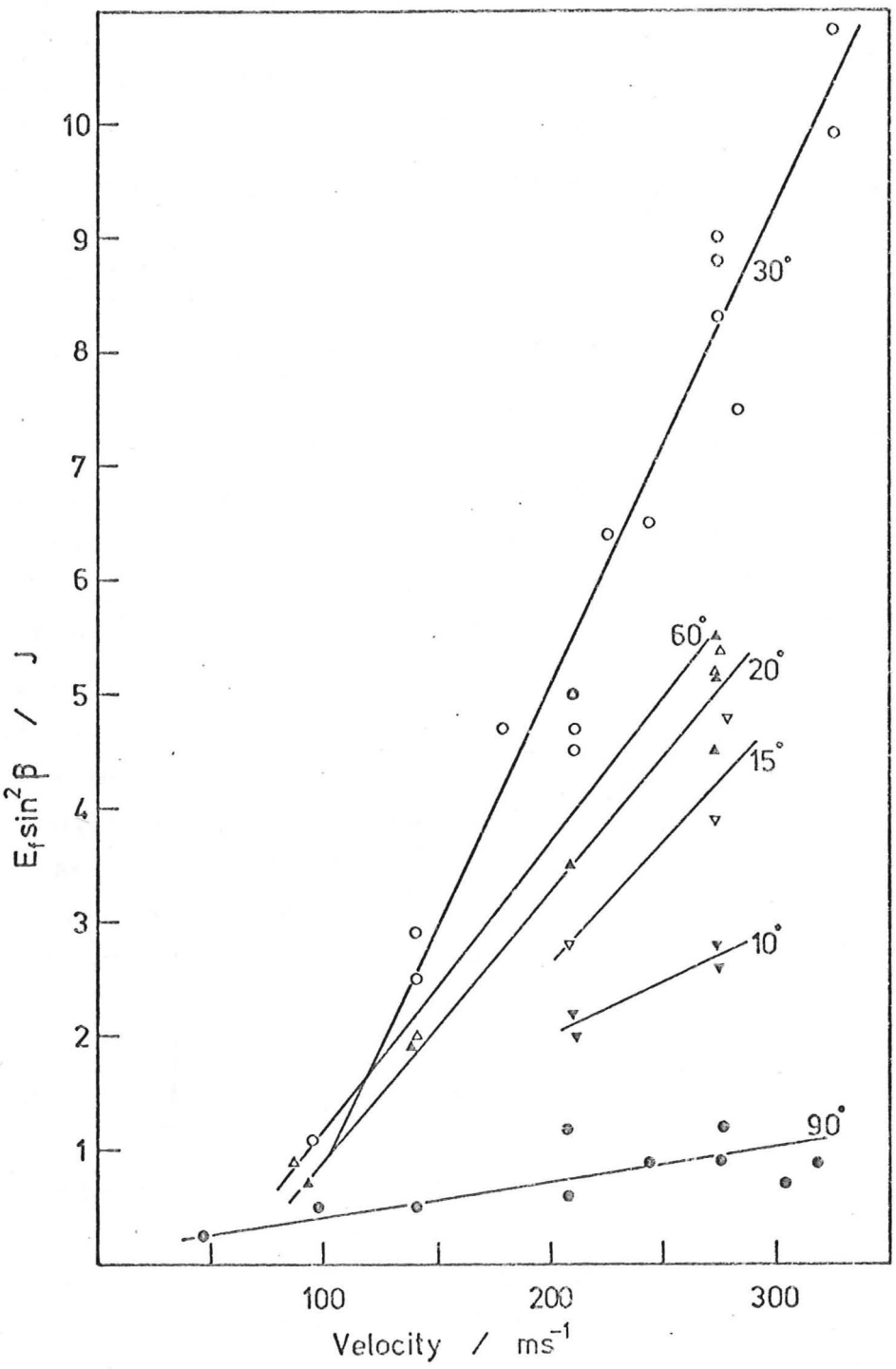

Figure 7.10
The kinetic energy associated with the final vertical velocity component (v sin β) plotted against impact velocity (u) for various impact angles (α).

the true effect of elastic energy storage; it can be seen that at very shallow impact angles ($\sim 10^{o}$) the elastic forces will again be most important. At intermediate angles, however, the "ramp" effect has a very marked influence. As may be seen in figure 7.10, this effect has the maximum influence at impact angles around 30^{o}; since the lip formed at the exit end of the crater, which constitutes most of the weight loss, must result from frictional forces between the ball and the "ramp", it is not surprising that this angle is near that at which the largest lip is formed.

7.5.4 The coefficient of friction in impact

From the measurements of ball rotation after impact discussed in section 7.4.3, the coefficient of friction between the ball and the surface during impact may be estimated. We shall assume that the classical theory of impact is applicable, arguing that the discrepancy noted in the previous section will have little effect on this calculation.

The sphere has radius r and mass m, the impact parameters u, v, α, β and μ being the same as in the preceding section. During impact, the total change in vertical momentum of the ball $= m(u \sin\alpha + v \sin\beta)$. This impulse results from a normal force N (t). So we can write:

$$\int N(t)\, dt = m(u \sin\alpha + v \sin\beta) \qquad (7.4)$$

where the integration is over the whole impact duration.

We have seen (section 7.5.3) that the ball slides throughout impact except at very high impact angles; the frictional force acting on the sphere at any moment is therefore $\mu N(t)$ and the angular impulse is equal to the change in angular momentum of the sphere:

$$\int \mu r N(t)\, dt = I\omega \qquad (7.5)$$

where I, the moment of inertia of the sphere, is $2/5\ mr^2$ and ω is its final angular velocity. Combining equations 7.4 and 7.5, and substituting for I, we find that

$$\mu = \frac{2r\omega}{5(u \sin \alpha + v \sin \beta)} \qquad (7.6)$$

Knowing r and the impact parameters ω, u, v, α, and β we can calculate μ. The "ramp effect", which was shown to introduce considerable disparity between the simple theory of impact and the experimental results, will introduce little error into this calculation; the term v sin β will be considerably larger than that predicted by the theory, but both v and ω are photographically determined, and it is these experimental values which are used in calculating μ.

The values of μ deduced from the photographic results by equation 7.6 are very consistent; not enough measurements of ball rotation were made to enable the variation of μ with velocity to be studied, but all the values of μ calculated may be represented by

$$\mu = 0.04 \pm 0.01$$

This value of μ is very much less than the coefficient of friction measured at low loads and sliding speeds (typically 0.8 - Bowden and Tabor 1950), but correlates well with the results of experiments at high sliding speeds under impact loading reported by Bowden and Persson (1961). They found values of 0.07 at a sliding speed of 200 ms^{-1}, and 0.05 at 400 ms^{-1} for the friction of hard steel (VPH 9.0 GPa) on itself in vacuo.

Studying the coefficient of friction at high loads and sliding speeds by measuring the rotation of a ball after oblique impact suggests itself as an alternative to Bowden and Persson's method; it has the advantage that the experiment need not be done in a vacuum, and any effects of a reactive gaseous atmosphere may be examined. A restriction of Bowden and Persson's approach is that the slider is rotated and supported electromagnetically, and must therefore be ferromagnetic; although electroplated metallic coatings may be used on a steel sphere, the method is not as versatile as that described above, in which the sphere may be made of any sufficiently strong material.

7.5.5 The energy dissipated in sliding

An estimate of the energy dissipated in sliding between the ball and the metal surface may be made from the measurements of ball rotation. If the frictional force $\mu N(t)$ (see section 7.5.4) produces an angular impulse $I\omega$, equation 7.5 applies. The work done by the frictional force during impact is equal to its impulse times the mean velocity of its point of application (see e.g. Routh 1905). We can therefore calculate the energy dissipated in frictional work:

$$W_F = \tfrac{1}{2} (u \cos\alpha + v \cos\beta) \int \mu N(t)\, dt$$

and using equation 7.5:

$$W_F = \tfrac{1}{2} (u \cos\alpha + v \cos\beta) \; I\omega/r$$

$$= (u \cos\alpha + v \cos\beta) \; mr\omega/5$$

Evaluating W_F for some of the experiments at an impact angle of 30^o, it was found that about 12% of the energy lost by the sphere in impact is dissipated in overcoming frictional resistance. For example, at 30^o and 210 ms^{-1}, the ball was found to lose $\sim$30 J in impact, $\sim$ 3.5 J of which formed W_F. At 142 ms^{-1} impact velocity, the energy loss was $\sim$12 J, and W_F was found to be $\sim$1.4 J.

The fraction of the ball's energy loss which is dissipated in sliding will clearly increase with decreasing impact angle; conversely, the fraction of the energy loss which corresponds to plastic deformation of the target will decrease with decreasing angle. The form of the curve in figure 7.9 may qualitatively be explained by this argument. The rotation of the ball at low impact angles could not unfortunately be detected with the camera used for this work; a slower framing speed would be needed to measure such low angular velocities. It was therefore not possible to measure the proportion of energy loss which was of frictional origin at shallow angles of incidence.

Chapter Eight

The Process of Normal Impact

8.1 Introduction

The previous chapter was largely concerned with the energy balance in oblique impacts; the dynamics of oblique plastic impact are very complex and no theoretical treatment which could be used to analyse the results has been published. The normal impact, however, is somewhat simpler, since the tangential forces which are so difficult to treat theoretically in the oblique case are absent. The static normal indentation of spheres into plane metal surfaces under loads sufficient to cause plastic flow has been studied by a number of workers. Rigorous theoretical analysis of the quasi-static problem is unfortunately impossible since the system has axial symmetry, but Ishlinsky (1944), using the unrealistic Haar-Karman criterion of plasticity, has determined analytically the distribution of oressure between a spherical indenter and its indentation. He finds that the mean pressure depends only slightly on the depth of the indentation, and is 2.6 to 2.9 Y where Y is the yield stress of the material. This has received experimental confirmation by Tabor (1948,1951) and other workers.

We have seen in section 5.2 that with the impact velocities used in this work, the mean rate of strain associated with the formation of an indentation is high ($> 10^4$ s^{-1}); the assumption of a constant mean pressure beneath the sphere under such conditions may well be invalid. The normal plastic impact of spheres on planes has received attention in the low velocity regime (< 5 ms^{-1}) in connection with dynamic hardness testing and the measurement of yield stresses under dynamic conditions (for example by Davies 1949, Tabor 1951 and Vincent, Gee & Hunter 1957); interest in terminal ballistics and meteoroid damage to spacecraft has stimulated research in the hypervelocity regime (> 1 kms^{-1}) where large-scale melting and cratering is produced, and the projectile

is damaged in the impact (Kinslow 1970 contains comprehensive reviews). Both low velocity and hypervelocity research have been reviewed by Goldsmith (1960) and Johnson (1972). Little information is, however, available about the intermediate velocity region (10 - 500 ms^{-1}) with which this work is concerned. At these velocities, with hard steel spheres impacting onto mild steel, the projectile suffers only elastic deformation and the crater formed during impact is less than the radius of the ball in depth.

Goldsmith and Lyman (1960) determined the force-indentation relation for steel balls striking various materials at 10 to 100 ms^{-1}; mild steel was not, however, studied by them. They found that for lead, aluminium (pure and alloyed) and annealed tool steel, the plastic indentation process departed from the assumption of a constant pressure beneath the indenter; the effective pressure was found to fall with increasing indentation depth. This effect, if corroborated, is clearly of importance in establishing a possible reason for the velocity exponents greater than 2.0 found in single impact tests (chapter 6); a series of experiments was therefore performed to examine the dynamics of the normal impact process, and to investigate, as far as possible, to what extent the deformation pattern differs from that caused by quasi-static indentation. The approach used was to measure the depths of craters formed by impact, and knowing the impact velocity of the indenting sphere, to plot a curve of energy against depth of indentation. Then by differentiating this curve (section 8.4) a graph of force against indentation depth could be obtained, and compared with the results of quasi-static loading experiments. The method is very simple, and makes the assumption that the energy losses due to elastic waves and frictional work are minimal. The justification of Davis and Hunter (1960) for ignoring the energy lost in elastic waves has been presented in section 7.1; for normal impacts the contact duration is greater than at oblique angles (typically > 100 us) and no great error is therefore introduced in ignoring elastic waves. The effects of interfacial friction will be discussed in section 8.5.2.

The experimental arrangements were almost the same as those described in chapter 7; for these experiments larger steel specimens were used to confine the region of plasticity well within the specimen.

8.2 Experimental

Specimens were cut from cold-worked En1A mild steel bar and were in the form of cylinders, 38 mm diameter and 40 mm long, with one face polished. The specimens were clamped to a massive ($\sim$ 10 kg) steel block and were impacted axially on the polished face, parallel to the direction of working of the steel. The 9.5 mm hard steel balls were accelerated in sabots using the gas gun described in chapter 3. The velocity of the balls before impact was measured photoelectrically to within $\frac{1}{2}$%; their rebound velocity was measured photographically using the technique described in section 7.3. Owing to the low value of the rebound velocity ($\sim$20 ms^{-1}) it could not be measured more accurately than $\sim$10% with the 20 μs framing interval of the Imacon camera used.

The depths of craters formed by impact were measured relative to the undisturbed surface of the specimen block using a dial gauge, and were reproducible to within 0.01 mm. Quasi-static loading tests were performed using a hydraulic press; the steel ball was placed between two mild steel specimens which were slowly (< 10 $kNmin^{-1}$) compressed. A dial gauge registered the separation of the two specimen cylinders, and hence the mean depth of the indentations.

8.3 Qualitative observations

Distinct differences were visible between the craters formed dynamically and quasi-statically. Figure 8.1 shows comparative photographs which illustrate the points of dissimilarity. These show two craters of identical depths, the one formed dynamically by the normal impact of a steel ball at 270 ms^{-1}, the other by the quasi-static application of a load of 110 kN. Immediately apparent is the nature of the surface at the bottom of the crater;

Figure 8.1
Indentations formed by quasi-static loading and by normal impact.

(a) was formed by the normal impact of a 9.5 mm diameter steel ball at 270 ms^{-1}.

(b) was formed by a 9.5 mm ball under a quasi-static load of 110 kN.

(c) and (e) show etched sections through the edges of the dynamic indentation in (a).

(d) and (f) show the edges of the quasi-static indentation in (b).

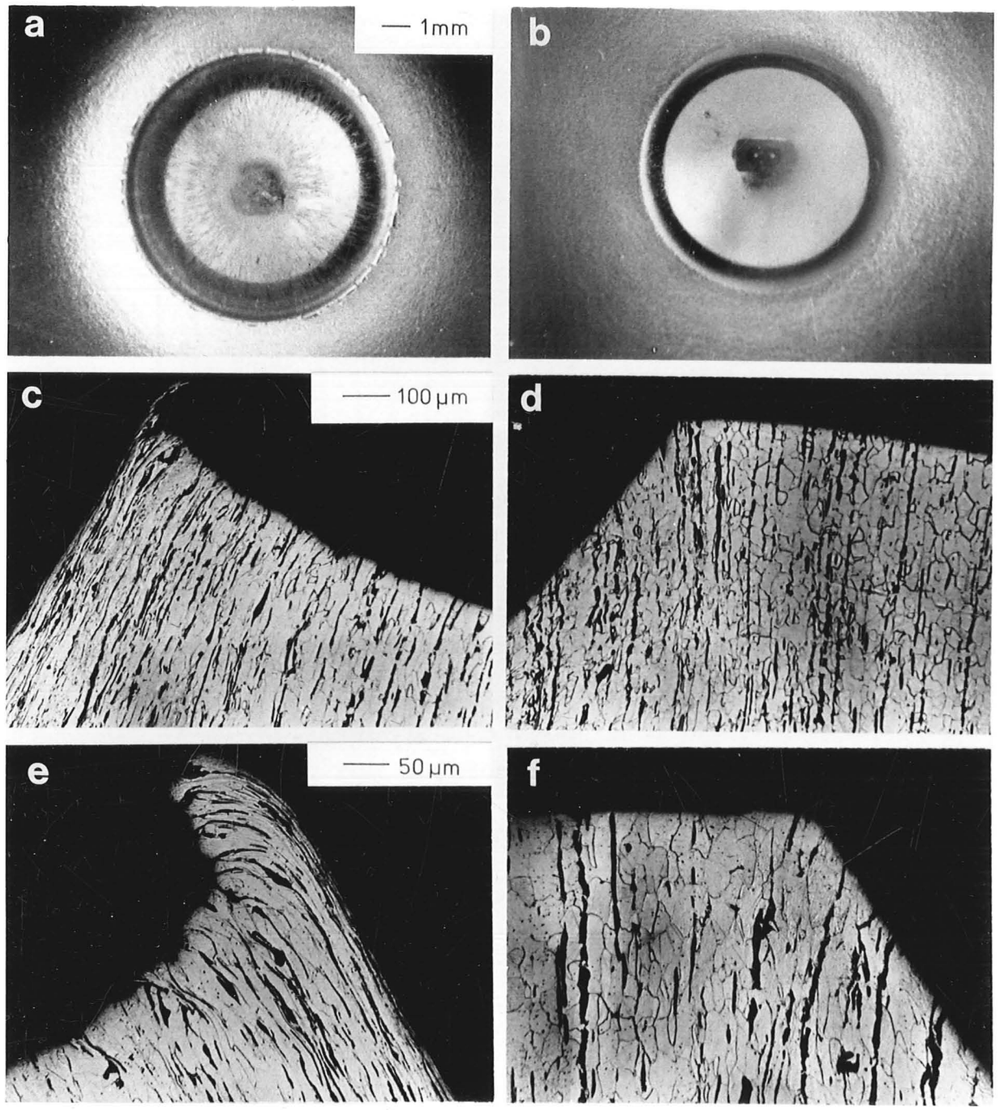

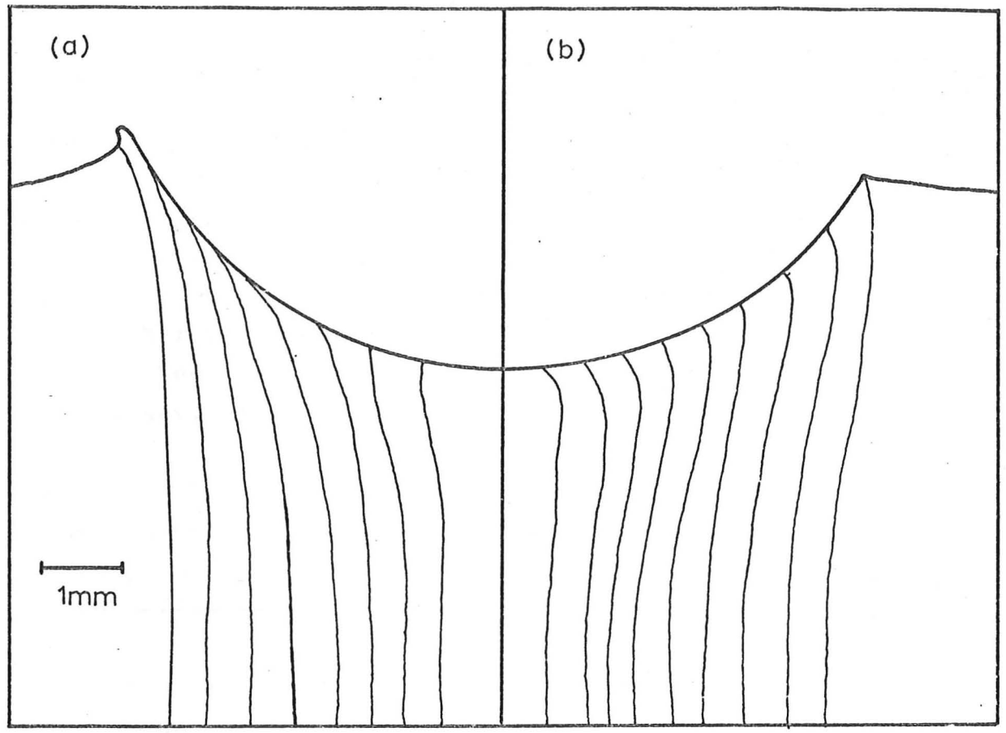

Figure 8.2
Subsurface deformation under normal impact sites, as revealed by distortion of drawing lines in the steel.
(a) Dynamic indentation by a ball at 270 ms^{-1}
(b) Quasi-static indentation under a load of 110 kN.
The drawing marks in the undeformed steel were perpendicular to the surface.

both specimens were polished before the experiment, and the static indentation in figure 8.1 b has retained this polish and has a smooth, shiny surface. The dynamic indentation in figure 8.1 a shows white radial streaks on its surface, identical with those seen at oblique angles of impact in figures 4.6 and 4.7. They are probably associated with frictional heating of the surface at high impact velocities.

The rim of the crater differs markedly between the two cases. Figure 8.1 c, d, e and f are photomicrographs of etched sections through the rims of the two craters. It is seen that there is little "piling-up" of metal close to the crater in the static case; the grain structure of the metal close to the crater rim shows that the plastic deformation is widely spread around the crater. The rim of the dynamic crater, on the other hand, is raised some way above the surrounding metal, there is considerable piling-up, and the grains in the raised lip are elongated. Furthermore, at the tip of the crater rim in figure 8.1 c there is a weakly-attached lip which might easily be removed.

The pronounced drawing marks in the specimens, visible in the photomicrographs, allow the pattern of deformation around the indentations to be assessed. After heavy etching, these drawing lines were photographed; figure 8.2 shows the pattern formed by the marks around (a) the dynamic and (b) the quasi-static indentations. These drawing lines were originally perpendicular to the impacted face of the specimen; it is seen that in (b) they have not been sheared far from this angle, whereas in the dynamically-formed crater in (a), the drawing lines at the edge of the indentation have been sheared parallel to the surface. The effect is particularly noticeable in figure 8.1c. Differences are also seen in the deformation below the centre of the indentations. The maximum deformation below the static indentation occurs some 500 μm beneath the surface; the drawing lines can be seen to bulge out around this point. In the dynamic case, the maximum deformation is immediately under the centre of the crater, and causes a different displacement of the drawing marks.

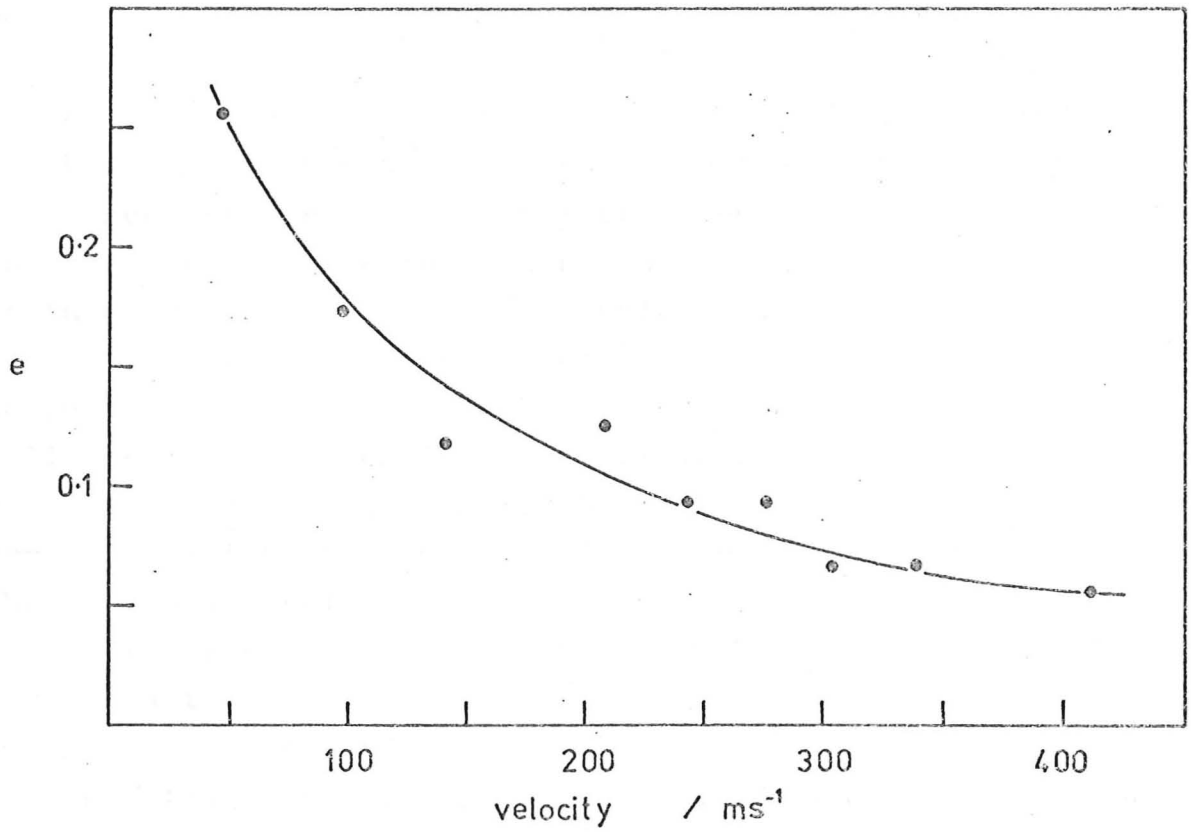

Figure 8.3
Coefficient of restitution (e) plotted against impact velocity for the normal impact of 9.5 mm steel balls against mild steel targets.

8.4 Quantitative measurements

Several experiments were made at impact velocities between 47 and 411 ms^{-1}. Figure 8.3 shows the results of the velocity measurements. The coefficient of restitution, e, which is the ratio of rebound velocity to impact velocity, has been calculated and plotted against impact velocity. It is seen that e falls with increasing impact velocity; the scatter in the points is no doubt due to the inaccuracy of the measurements of rebound velocity.

The depths of the craters after impact were measured. As Tabor (1951) has pointed out, the indentation will recover elastically by a certain amount during the rebound stage of the impact, the elastic energy stored up during impact being converted into the kinetic energy of the rebounding ball. As a result of this elastic recovery, the depth of the indentation measured after impact will be less than the maximum depth of penetration occurring during impact. Hertz's (1881) equations for the elastic deformation of contacting surfaces are not accurately applicable to the deep indentations formed in these experiments; the extent of the elastic recovery was therefore determined empirically. Specimens were loaded incrementally in the hydraulic press, the depth of the indentation being measured with a dial gauge; after each loading increment the load was relaxed and the elastic recovery of the crater depth measured. From these results the graph in figure 8.4 was drawn. The elastic recovery was small, less than $1\frac{1}{2}\%$ of the depth of the indentation; the wide scatter of the points is due to the resolution ($\sim$ 10 μm) of the dial gauge.

Figure 8.5 shows the initial kinetic energy of the impacting ball plotted against the depth of the indentation produced; to the depth measured after impact has been added the small correction for elastic recovery. From this curve, it is possible to derive the corresponding force/indentation curve. Neglecting elastic deformation, which as we have seen is much less than the plastic displacements, the work done, dE, in increasing the depth of the indentation from x to x + dx is

$$dE = F(x)\, dx$$

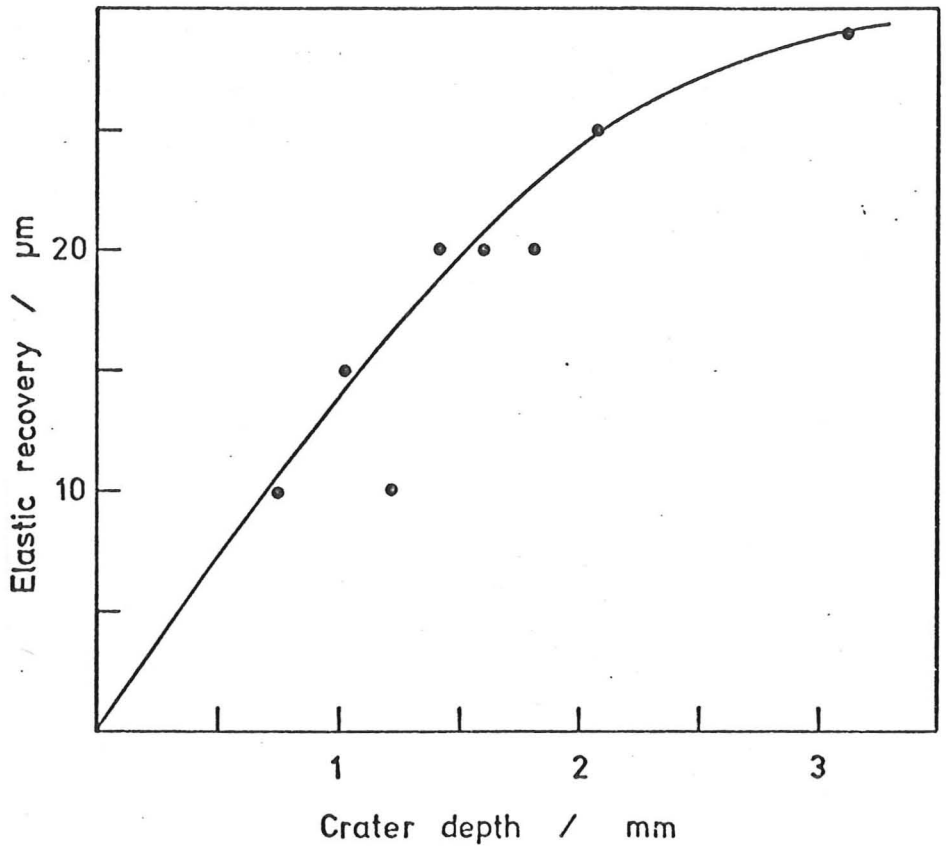

Figure 8.4
The elastic recovery measured in a slow-loading normal indentation test. The initial portion of the curve is only approximate - before any plastic indentation is formed, the elastic recovery will equal the (elastic) indentation depth.

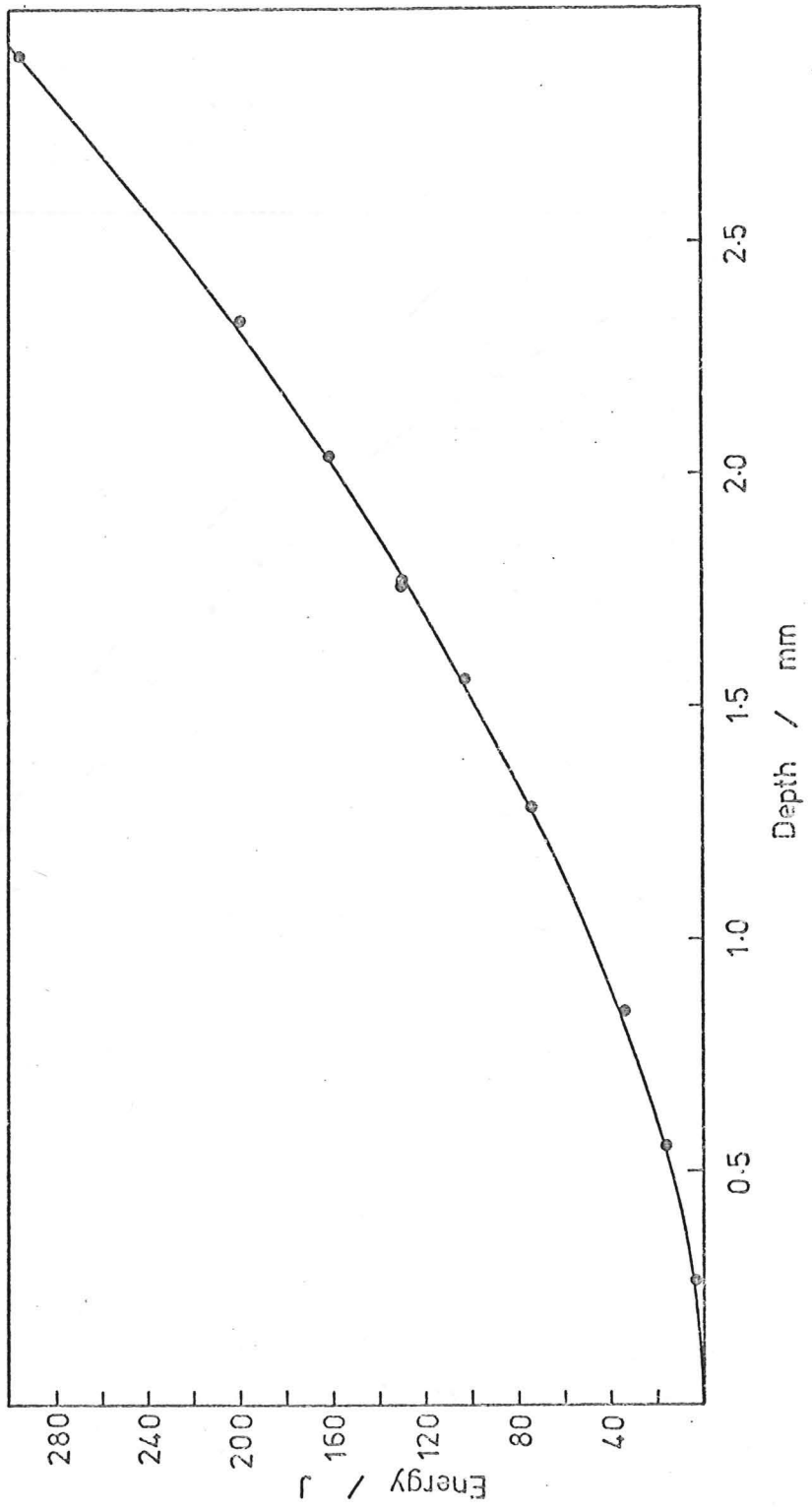

Figure 8.5
Kinetic energy of the ball versus indentation depth (plastic + elastic). The elastic recovery deduced from slow-loading experiments has been added to the crater depth measured after impact.

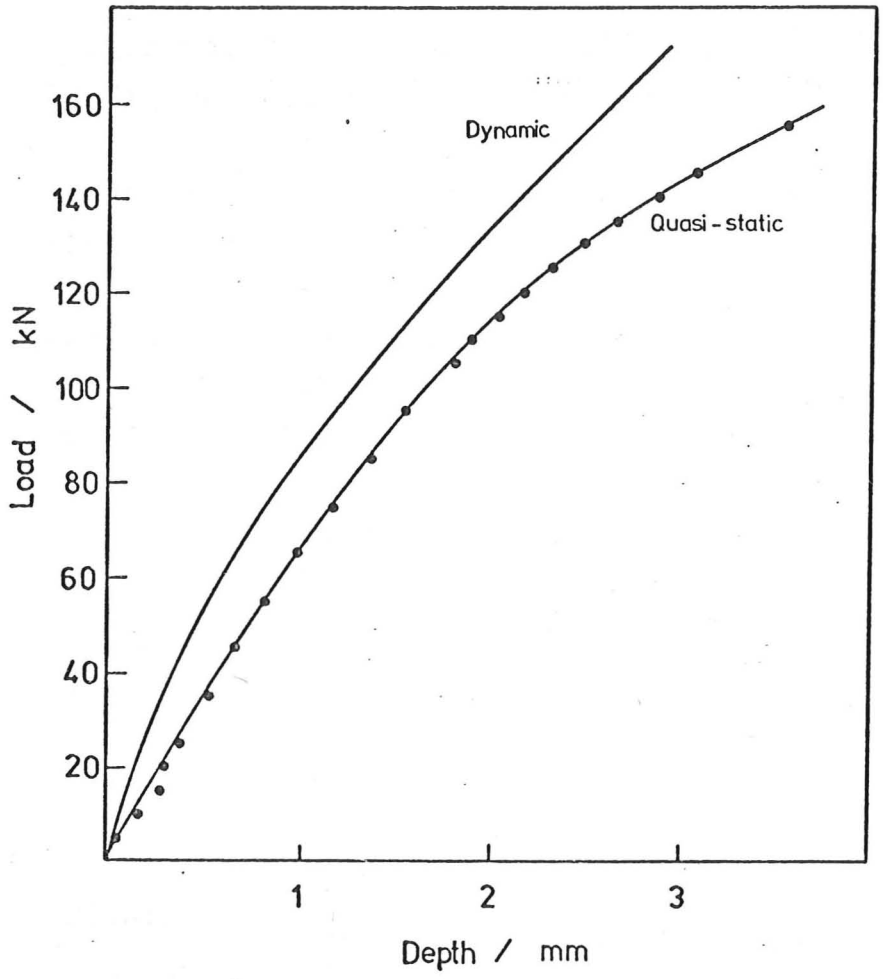

Figure 8.6

Load versus depth curves for normal indentation; quasi-static curve shows the result of a slow-loading experiment, dynamic curve is derived from figure 8.5 as described in the text.

Here F(x) is the force which must be applied to the indenter when in an indentation of depth x in order that further plastic yielding may occur. So

$$F(x) = dE/dx \text{ at the depth } x.$$

By differentiating the function E(x), which is displayed in figure 8.5, we can determine F(x). Numerical differentiation of the curve in figure 8.5 yields that in figure 8.6 (labelled "dynamic").

The results of a quasi-static loading experiment as described in section 8.2 are shown for comparison. The depth of indentation in this case was measured under load; so no correction for elastic recovery need be made and the two curves may be directly compared. Several quasi-static experiments were made, and the curves were found not to differ from that in the figure by more than 2%. The force acting on the sphere during dynamic indentation is consistently higher than that for the corresponding quasi-static indentation.

8.5. Discussion

8.5.1 Discussion of the mode of deformation

The extended crater lips visible in figure 8.1 are clearly the source of the weight losses measured in the normal impact of single spheres by Sheldon and Kanhere (1972), and suggested by the general trend of the curve in figure 6.1. The formation of these lips only occurs in dynamic indentations, and would not be predicted by any quasi-static analysis of the impact, such as that attempted by Sheldon and Kanhere. The weight loss, or even the lip volume, cannot be related to the crater volume by any theoretical treatment, and must therefore be determined empirically. The lips formed in dynamic normal indentations are very similar to the ridges raised at the sides of craters formed in oblique impacts (as in figure 4.13); such lips are probably responsible for the measurable weight losses at angles between 40° and 70° plotted in figure 6.1, when the terminal lip had not been removed during the impact.

The mechanism of formation of the lips must be considered alongside the differences in deformation pattern between the quasi-static and dynamic cases (figure 8.2). Yew and Goldsmith (1964), studying the impact of steel balls on lead at velocities of $\sim 3\ ms^{-1}$, measured displacements of inscribed grids beneath the indentation and found a similar difference in the pattern of deformation, for which they offered no explanation. The lip formation and the intense shear deformation at the sides of the indentation may be thought of as resulting from the extrusion of a comparatively weak layer of metal between the sphere and the bulk of the material. That this weaker region may have resulted from thermal softening is apparent from a simple calculation of the temperature rise which will have occurred during impact. If we assume that all the plastic work associated with the formation of the indentation is converted into heat (a reasonable assumption for the purposes of this calculation - see Taylor and Quinney 1934), and assume that the volume of metal deformed is equal to the volume of the indentation (supported by metallographic observations), we find that a temperature rise of some 900 K is associated with an impact at $275\ ms^{-1}$. The volume of such an indentation was found experimentally to be $39\ mm^3$, and the kinetic energy of the impacting ball 134 J. The specific heat of steel was taken as $500\ Jkg^{-1}K^{-1}$ and its density as $7.9\ Mgm^{-3}$. There is no metallographic evidence of a temperature rise in figure 8.1, but as was discussed in chapter 4, significant thermal softening may occur at temperatures below that needed for the transformation to austenite.

Another mechanism which might be suggested to explain the formation of the crater lips in normal impact is some form of plastic wave effect. The velocity with which a plastic strain can propagate in a metal is given by the formula:

$$v = (1 + \varepsilon).(K/\rho)^{\frac{1}{2}}$$

where ε is the strain, K is some modulus of the metal and ρ is its density (Taylor 1946). In the case of a plastic

strain, K is the slope of the stress-strain curve at the relevant plastic strain; for large strains in a fully work-hardened material, such as we have here, K, and hence v, may be very small. Any attempt to deform the metal faster than the corresponding plastic disturbance can propagate must lead to a localization of the strain, and might explain the formation of the lips. However, as we shall see in the next section, other observations indicate that thermal softening, rather than a plastic wave effect, is responsible for the differences between the quasi-static and dynamic indentations.

8.5.2 Discussion of the dynamics of the indentation process

The decrease in the coefficient of restitution with increasing velocity, noted in figure 8.3, is in agreement with earlier work on impact at lower velocities. Tabor (1951) has treated the subject in detail. It is of interest to compare the energy of rebound of the ball with the elastic energy stored during indentation. The velocity, and hence the energy, of the rebounding ball was measured photographically, and the elastic potential energy stored during impact may be deduced from the elastic recovery curve in figure 8.4 and the static loading curve in figure 8.6. The elastic energy stored, for example, by a ball impacting at 275 ms^{-1} may be deduced from the depth of the crater formed at this velocity (1.72 mm), the equivalent static load being found from figure 8.6 to be 110 kN. We know from figure 8.4 that the variation of elastic recovery with crater depth (and hence load) is almost linear up to this depth; the elastic recovery for a static load of 110 kN is $\sim$22 μm. So the elastic energy stored is $\frac{1}{2}$ x 22 μm x 110 kN = 1.2 J. The velocity of the rebounding ball was found to be 24 $\pm$ 3 ms^{-1}, implying a kinetic energy of 1.0 $\pm$ 0.3 J. The elastic energy stored during the impact correlates well with the rebound energy of the ball.

The most obvious implication of figure 8.6, namely that the dynamic indentation pressure is always greater than the static, has been pointed out by several workers (e.g. Tabor 1951, Davis & Hunter 1960 and Goldsmith & Lyman 1960), and is well established.

The data presented in figure 8.6 may be treated in another way. Knowing the load needed to deform the indentation further from any depth, and the geometrical shape of the crater (spherical), we can calculate the mean contact pressure (load/projected area of the indentation). Tabor (1951) has shown empirically that a representative strain (ε) may be associated with a spherical indentation, given by

$$\varepsilon = 20\ d/D\ \%$$

where d is the chordal diameter of the indentation and D is the diameter of the indenter. Making the somewhat naïve assumption that this expression will be valid for indentations formed quasi-statically and dynamically, we can convert the crater depth into a representative strain. Furthermore, dividing the mean indentation pressure by 2.8 (see section 8.1) gives an approximate value for the yield stress of the material under the indenter. This assumes, of course, that the deformation pattern around the dynamic indentation is the same as that around the static.

Figure 8.7 shows the yield stress, determined in this way, plotted against the representative strain, for the range covered by the impact velocities used. While the assumptions which are made in this analysis are sweeping, an interesting effect which cannot result from these assumptions is shown. The static stress-strain curve, derived from the load/indentation curve in figure 8.6, is parallel to the strain axis, indicating that the mean contact pressure (or stress) under the indenter is independent of crater depth (or strain). The curve derived from the dynamic results, however, shows a pronounced drop in the pressure at large strains; it appears that the indentation pressure falls with increasing crater depth (i.e. velocity of impact). Similar results have been obtained by Goldsmith and Lyman (1960) (see above) and by Goldsmith and Yew (1962) who examined the dynamic penetration of conical indenters into metals and found a drop in mean indentation pressure with increasing velocity. Inertial effects, work-hardening and the rise in yield stress

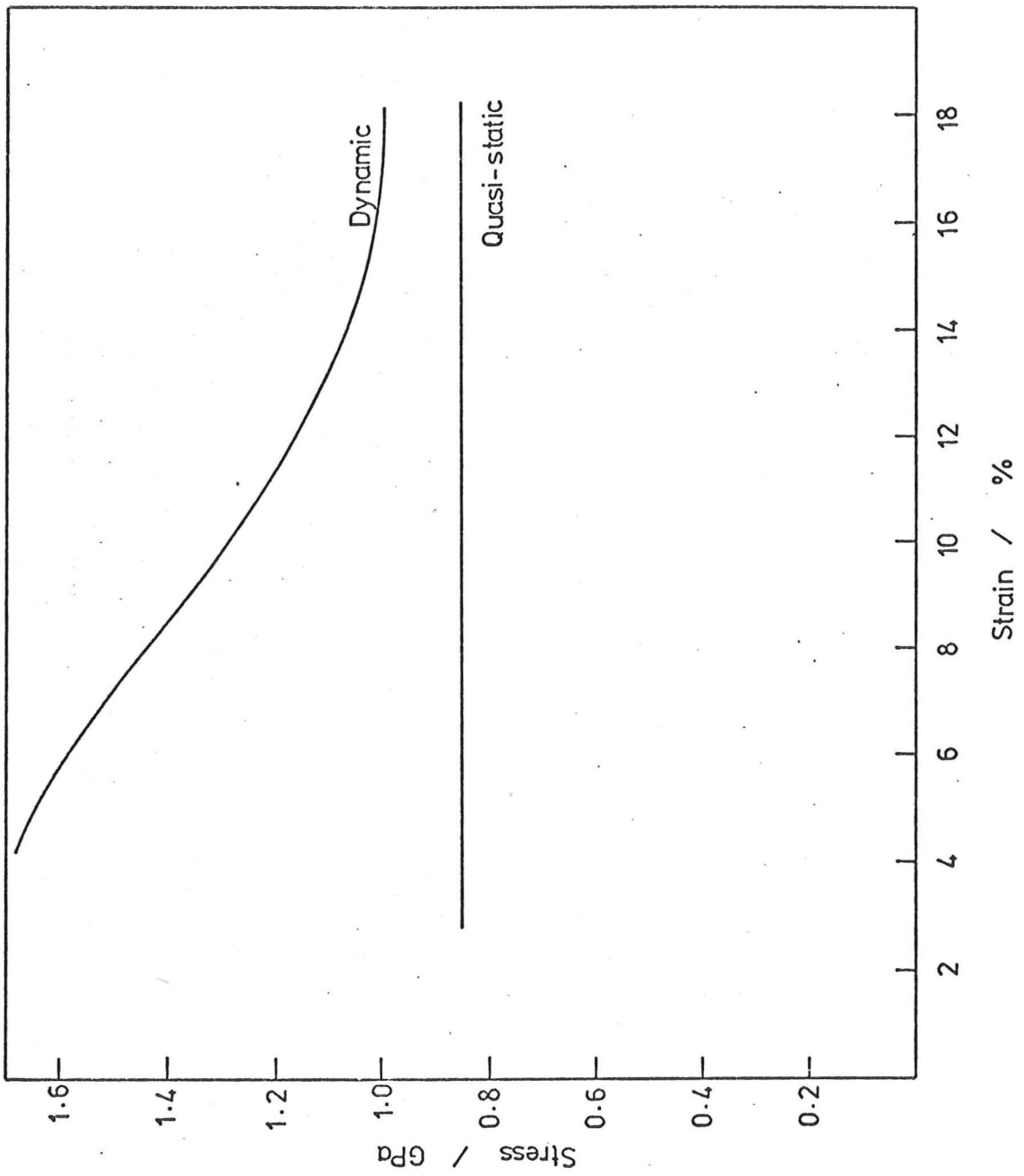

Figure 8.7
Dynamic and static stress-strain curves for mild steel. Their derivation is described in the text. Both curves must pass through the origin but the method of derivation of the curves does not allow them to be drawn accurately within the low strain region.

with strain-rate which is well established (for a review see Campbell 1973) would all tend to increase the mean indentation pressure. The observed fall is therefore surprising; Goldsmith and Yew suggested that the fall in coefficient of friction with increasing velocity (Bowden and Freitag 1958) caused the effect. However, Johnson (1970) has shown that although friction may influence the pattern of deformation below the indentation, the mean contact pressure is little affected; it therefore seems unlikely that the variation of friction can explain the whole effect. Johnson's calculation was performed for a wedge indenter, since the axially symmetrical problem is intractable, but the effect would be expected to be less for an axisymmetric indenter (Tabor 1970).

A mechanism which can explain the drop in mean indentation pressure at high velocities is the thermal softening suggested in section 8.5.1. As we have seen, provided the loss of heat from the deformed region is not too great during the impact time, high temperatures and consequent thermal softening of the deformed region may develop. The yield stress of the metal would fall, accounting not only for the deformation pattern visible in figure 8.2, and the extrusion of the crater lips, but also for the fall in indentation pressure with increasing velocity. This mechanism will be discussed in more general terms in the next chapter.

The plastic wave effect mentioned in section 8.5.1, which might explain the deformation pattern around the indentation, cannot however account for the drop in indentation pressure with increasing velocity; it would predict a rise rather than a fall. The effects of the plastic wave effect, inertia of the metal and the increase in flow stress with strain rate would tend to increase the indentation pressure with velocity. It appears that the opposing effect of thermal softening dominates in this case.

8.6 Conclusions

Significant differences exist between the patterns of deformation around indentations formed in mild steel by

the impact of steel spheres at velocities from 50 to 400 ms^{-1} and those formed by quasi-static loading. Pronounced lips are raised in the dynamic case which are absent in the static; the tips of these lips are fragile and account for the weight losses observed in single impacts at 90^{o}.

Measurements of the depths of craters formed by impact at different velocities indicate that the mean indentation pressure is always greater in the dynamic case than in the static. However, the mean dynamic indentation pressure is observed to fall significantly with increasing velocity. This effect, and the deformation patterns, may be explained by adiabatic heating of the deformed metal around the indentation, leading to thermal softening, which dominates over the opposing influence of strain-rate effects, plastic wave effects and inertia of the target metal.

Chapter Nine

General Discussion and Conclusions

9.1 Introduction

The work described in the previous chapters has provided information not only on the erosion of ductile metals by solid particles, but also on the coefficient of friction at high loads and sliding velocities and on the broad subject of the plastic impact process, for both normal and oblique impacts. It was felt that some unifying discussion was needed to combine the conclusions of the various chapters relevant to erosion; the other topics have been discussed in some detail already. This chapter therefore presents a general discussion of the results obtained in the previous chapters and examines the role in erosion of the various possible mechanisms of material removal. In section 9.5 a somewhat speculative approach to erosion is developed and a method of predicting the erosion resistance of a metal from its physical properties is presented and shown to correlate remarkably well with experimental data.

9.2 Ploughing deformation

It has been shown that spherical particles striking a metal surface obliquely can indeed remove metal from the surface by "ploughing deformation" as defined in chapter 2. A lip of material is sheared forward in front of the ball and may remain at the end of the crater as the ball rebounds from the surface. There exist a critical angle and velocity at which the lip formed at the end of the crater during impact becomes detached; above the critical velocity or below the critical angle all impacts result in removal of the lip. The critical angle and velocity are interdependent and are functions of other parameters such as particle density and target material. Metallographic examination reveals that lips which have been formed but

not detached, resulting from impacts just below the critical conditions, are attached to the bulk of the material by a relatively narrow neck of material; within this neck is a thin region of intense shear deformation. It is suggested that this band results from adiabatic shear: localized strain of the metal resulting from thermoplastic instability of the deformation process. The theory of such instability has been discussed in detail by Recht (1964). Observation of surface oxidation at the base of the lip in mild steel confirms that substantial localized temperature rises occur during impact. Other metallographic evidence shows that when lips are detached during impact the separation occurs within the shear band.

The fact that the size of the lip is defined, even when it is not removed, by this shear band, indicates that when the lip is removed from the crater by a subsequent nearby impact, as suggested by Tilly (1969a), it will have the same volume as if it had been removed by the particle which formed it. The measurements of weight loss in chapter 6 confirm this; the curve of weight loss against velocity, extrapolated below the critical velocity, shows excellent agreement with the results of the multiple impact erosion experiments of Kleis (1969).

Examination of lips recovered after detachment, and high-speed photography of the impact process, reveal that lips are removed in a small number of pieces (usually one or two) and may sometimes remain attached to the rebounding particle.

An investigation of the influence of particle size on the impact deformation reveals that the ploughing process may be expected to occur over the full range of sizes of erosive particles, from 1 μm to 1 mm, and that results obtained with particles as large as 10 mm will be applicable to the smaller sizes of particle.

Quantitative measurements of weight losses, crater volumes and energy losses in single impacts reveal that previous theoretical approaches are in error in assuming that the weight loss in a single impact will always be proportional to the kinetic energy of the incoming particle. Neither the weight loss, nor the crater volume nor the energy lost by the particle in oblique impact is proportional to its incident energy.

9.3 Normal impacts

While weight loss measurements were not made for impact experiments at 90^{o}, the general trend of the graph in figure 6.1 and the results of Sheldon and Kanhere (1972) indicate that weight losses result from single impacts of spheres at this angle. None of the theoretical approaches can account for this, since they suggest that wear at normal impact results from repeated deformation of the metal, from fragmentation of the particle, or is caused by impacts on a previously roughened surface; these explanations are clearly not applicable to this work. Sheldon and Kanhere (1972) suggest that metal "flows out around the sides of the cavity until it is strained sufficiently to break off".

The ridges raised at the sides of craters formed by oblique impact (figure 4.13) are very similar to those raised around normal impact craters (figure 8.1) and probably result from the same mechanism. They are characterised by fragile narrow tips which must be the source of the weight losses measured in normal impact. The observation that these ridges are only formed in dynamic normal indentation, and are completely absent in quasi-static experiments, is of great importance. Doubtless similar results would be obtained if the oblique impact could be simulated quasi-statically, but this experiment would be very difficult to perform. The process by which the ridges are formed depends therefore on the deformation being carried out rapidly; the mechanism of thermal softening proposed in chapter 8 accounts for these observations. Other possibilities, such as plastic wave effects, would not account for the pronounced fall in dynamic indentation pressure observed with increasing impact velocity (section 8.5.2), which may be explained by thermal softening.

The thermal softening envisaged is a rather less localised phenomenon than that responsible for the narrow bands at the base of crater lips in oblique impacts; the deformation of a comparatively large volume of metal leads to a temperature rise and subsequent softening. In this case, heat conduction from the deformed region will be much less important than from a narrow localised shear band, and the rate of strain involved in the deformation will therefore

not be critical, provided that it is sufficiently high to result in heating. The initial formation of the lip in front of the particle in oblique impacts will also be aided by thernal softening, although as the lip becomes further deformed during impact, a narrow shear band finally forms at its base. Against the effects of thermal softening must of course be set the work-hardening behaviour of the metal; as was seen in chapter 4, if the metal has a sufficiently high rate of work-hardening (e.g. annealed copper) the localization of deformation resulting from thermal softening is outweighed by the work-hardening tendency of the metal and only a small lip is formed in oblique impact. In practical erosion situations, however, the surface material is always heavily strained, and its rate of further work-hardening is very small.

It may therefore be argued qualitatively that the volume of metal removed in the impact, whether in the terminal lip or in the tip of the side ridges of the crater, will depend on the tendency of the metal to thermal softening during deformation. A predictor of erosion resistance based on these ideas will be presented in section 9.5. While the discussion of normal impacts presented here has mainly considered the impacts of spherical particles, the arguments would be expected to apply generally to any shape of angular particle; similarly, the discussion of oblique impacts will apply to the impacts of angular particles at large negative rake angles, which will constitute a large fraction of the oblique impacts of angular erosive particles (see section 2.3).

9.4 Other mechanisms of erosion

The results of the experiments performed with spherical particles shed some light on the mechanisms of erosion proposed by other authors. A study of the impacts of single angular particles (Winter & Hutchings 1974) and the arguments in section 2.3 suggest that ploughing deformation, as observed with spherical particles, will be an important mechanism of metal removal by angular particles impacting at shallow angles. It is, however, difficult to give a more accurate prediction of

the relative incidence of ploughing and cutting deformation than that presented in section 2.3. Certainly cutting deformation, of the type idealized by Finnie (1958, 1960) in his model, does lead to the removal of a fragile chip under some conditions (as evidenced by Tilly's (1973) SEM photograph), but Winter and Hutchings' work suggests that this may be a very infrequent occurrence, and that more often the impinging particle rolls over the surface, raising a large but firmly-attached chip.

Since these mechanisms, at least, of metal removal can be identified, the process of erosion must be stochastic; the relative importance of different mechanisms will depend on the probability of their occurrence and upon their efficacy in removing material. It therefore seems certain that no model which assumes a single mechanism can describe more than a part of the erosion process. It might be, however, that under certain circumstances one mechanism is so much more probable, or leads to so great a weight loss, that it outweighs all others in importance; in this case, a description of that one mechanism might enable erosion to be predicted. From the evidence presented in this work it is not possible to state whether the ploughing mechanism will dominate in importance, but it can certainly be said that some of the mechanisms suggested by other workers will make insignificant contributions to the total erosion rate.

Smeltzer et al.(1970) and Ascarelli (1971) suggested that erosion resulted from melting of the metal under the impacting particle; the molten metal is then sprayed out in the form of droplets or adheres to the rebounding particle. In order for this mechanism to be feasible, some mechanism must be envisaged whereby enough energy can be concentrated in a sufficiently small region of the target surface for melting to occur. While widespread melting and even vaporization of the target and projectile material certainly occurs at very high impact velocities (> 5 kms^{-1} - see e.g. Charters, Gehring & Maiden 1966), no evidence of such widespread melting was found in the velocity regime studied in this work. The low coefficient of friction during oblique impact (section 7.5.4) indicates that substantial softening or even melting of the metal has occurred at the interface, but the thickness of the inter-

facial layer must have been less then ~1 μm since no evidence of surface melting was visible in the sectioned specimens. Smeltzer suggests that if an angular particle impacts with a sharp corner downwards, this will lead to very high temperatures, and melting, at the point of impact. However, the volume of the indentation formed by any shape of particle, to a first approximation, is proportional to the kinetic energy lost in the impact; an angular particle impacting point downwards may lose more energy than in other orientations, but this will be dissipated over a proportionately larger volume. The correlation between erosion resistance and melting point pointed out by Smeltzer, or between erosion and Ascarelli's "thermal pressure", is no evidence that melting actually occurs.

Temperature rises definitely do take place in erosion; Neilson and Gilchrist (1968 b) observed bulk specimen temperature rises of ~160 K during accelerated erosion testing, and Uetz and Gommel (1966) made thermo-electric measurements of transient rises of ~300 K in the normal impact of steel balls on steel surfaces at 70 ms^{-1}. However, these temperature rises, although sufficient to account for some thermal softening, are not enough to agree with a theory involving widespread melting.

The only effect of geometrical scaling on this mechanism can be to change the effects of heat conduction; taking the results of chapter 5 to imply that Tabor's (1951) model of impact is applicable to this case, we see that the energy dissipated per unit volume of metal during impact must be independent of particle size. Changing the particle size will alter the impact duration and also the scale of the deformation, and may therefore change the heat losses by conduction. The maximum possible temperature rise in the deformed region may be calculated by neglecting these losses; we have already seen (section 8.5.1) that this will not be sufficient to cause melting.

Tilly (1975) considers particle fragmentation to be important; we have seen in figure 1.8 how it can affect erosion rates, especially at normal impact. However, fragmentation will not change the fundamental mechanisms by which the fragments remove material; even though the fragments may strike the surface at different velocities and angles from the original particle, they must

still remove material in the same way as single, non-fragmenting particles. For this reason the effects of fragmentation have been neglected in this study. However, fragmentation of many erosive particles will occur during impact and must clearly be allowed for in any comprehensive theory of erosion; another statistical element must be introduced into the analysis.

9.5 Prediction of erosion resistance

The dependence of erosion wear on particle velocity and angle of impact has been empirically determined by many workers, and is found to vary little among different metals (see sections 1.2.3 and 1.2.4). Such dependence may be easily represented by empirical equations for application to practical problems.

The solution of problems of erosion in industrial plant, however, often requires some method of predicting the comparative erosion rates of different metals under the same conditions, since it is rather more difficult to redesign the machinery to minimize the erosion rate than to change the material from which the wearing components are made. If theoretical approaches such as Finnie (1958) or Bitter's (1963) are tried it is found that the rate of erosion of a metal depends upon material properties which must not only be determined by practical erosion tests, but which are also found to vary with experimental conditions (see section 1.5). It would clearly be of considerable usefulness if some method of predicting the erosion resistance of a metal or alloy from a knowledge of its physical properties could be developed.

As was seen in chapter 1, indentation hardness is not a good predictor of a metal's resistance to erosion; melting temperature is better (Smeltzer et al. 1970). Ascarelli (1971) has developed a "thermal pressure" parameter which seems to predict erosion rather better than any of the indicators suggested by other workers. His arguments are somewhat implausible, but in the development of such an indicator, its validity when compared with experimental data is more important than the arguments leading up to its development.

Another indicator of erosion resistance, which is in some respects better than that of Ascarelli, may be deduced from the mechanism of lip formation discussed above (see section 9.3). The mechanism envisaged is one of thermal softening; the concentration of deformation which leads to the formation of an easily detached crater

lip results from adiabatic deformation of the metal, the consequent temperature rise leading to a drop in yield stress of the deformed metal. A detailed analysis of the mechanism of lip formation would be very difficult, but we can assess the importance to this mechanism of some physical properties of the metal. We shall assume that the process of deformation is carried out so rapidly that thermal conduction is not significant; the process is truly adiabatic. We would not therefore expect the thermal conductivity of the metal to influence the process. Factors which would increase the tendency to thermal softening under these conditions are a high plastic flow stress, since the energy dissipated for a given strain will be proportional to the flow stress, a low heat capacity per unit volume (= C x ρ) and a high rate of thermal softening. As an approximation we assume that the rate of thermal softening is inversely proportional to the difference between the specimen temperature and its melting point ($T_m - T = \Delta T$). The volume of the lip might be expected to be proportional to the volume of the associated crater, and therefore inversely proportional to the relevant plastic flow stress (see section 5.2). From these arguments, then, it is deduced that a large lip would be favoured by a low value of $C\rho\Delta T$, if we assume that the opposite influences of the metal's plastic flow stress cancel each other out. The arguments presented are purely qualitative; the sole evidence for the validity of the parameter $C\rho\Delta T$ as an indicator of erosion resistance lies in the empirical data to be presented below.

Comparison of the erosion behaviour of well-characterised metals under controlled conditions has received little attention; the only published results are those of Tadolder (1966) and Finnie, Wolak and Kabil (1967). Tadolder eroded a number of pure metals with quartz sand using a centrifugal accelerator; Finnie et al. tested a similar range of metals with silicon carbide grit in an air-blast rig.

Ascarelli (1971) compares his "thermal pressure" (P_t) with the results reported by Finnie, Wolak and Kabil; his figures have been replotted in figure 9.1. The volume eroded by 1 kg of abrasive at a velocity of 136 ms^{-1} is plotted against P_t calculated from the equation in 1.4.4.

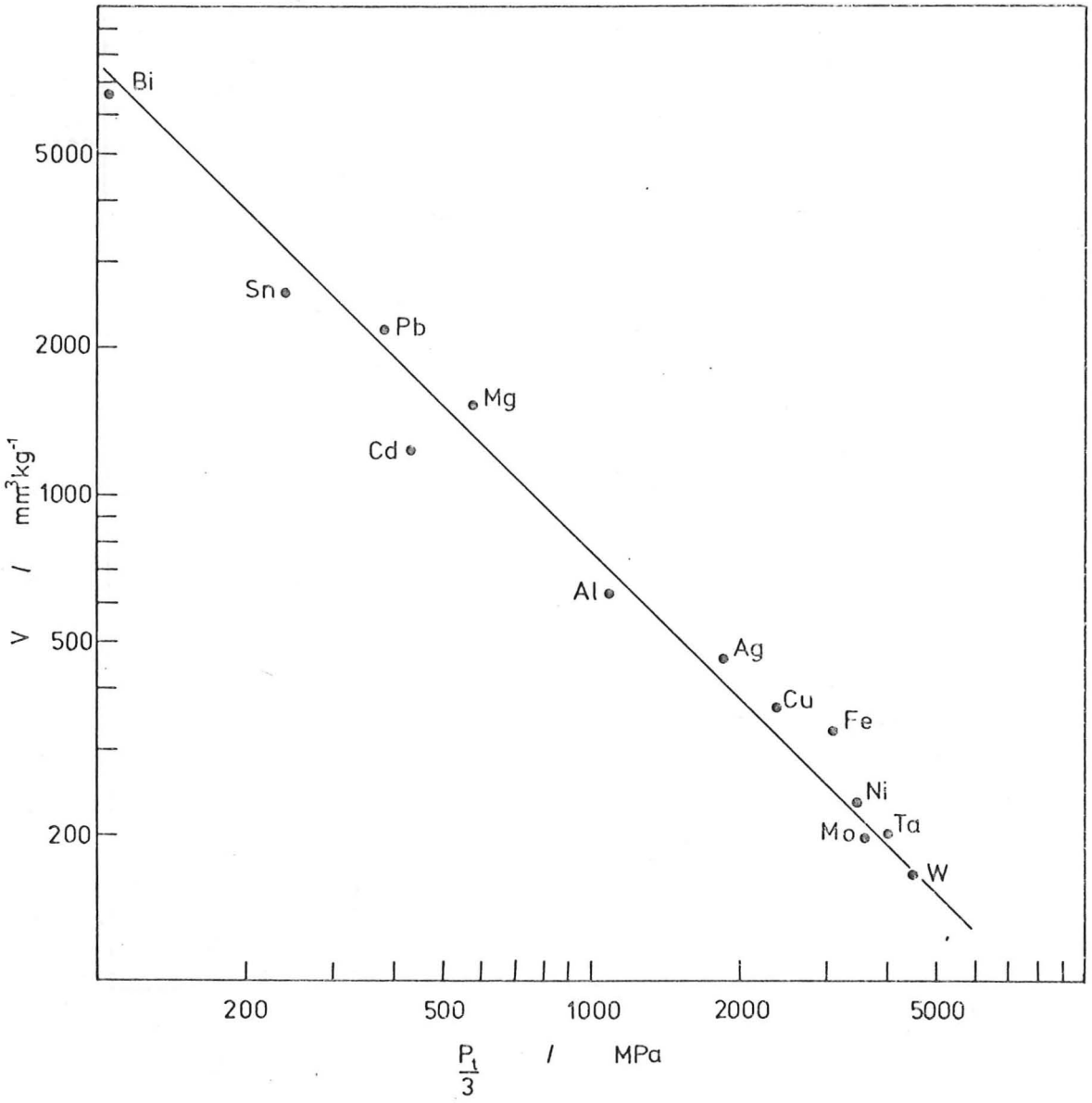

Figure 9.1
Volume erosion rates (mm^3 per kg abrasive) for pure metals plotted against Ascarelli's thermal pressure parameter, P_t. The erosion rates are those determined experimentally by Finnie, Wolak & Kabil (1967) using an air-blast rig, silicon carbide particles at 20^o impact angle, and a velocity of 136 ms^{-1}.

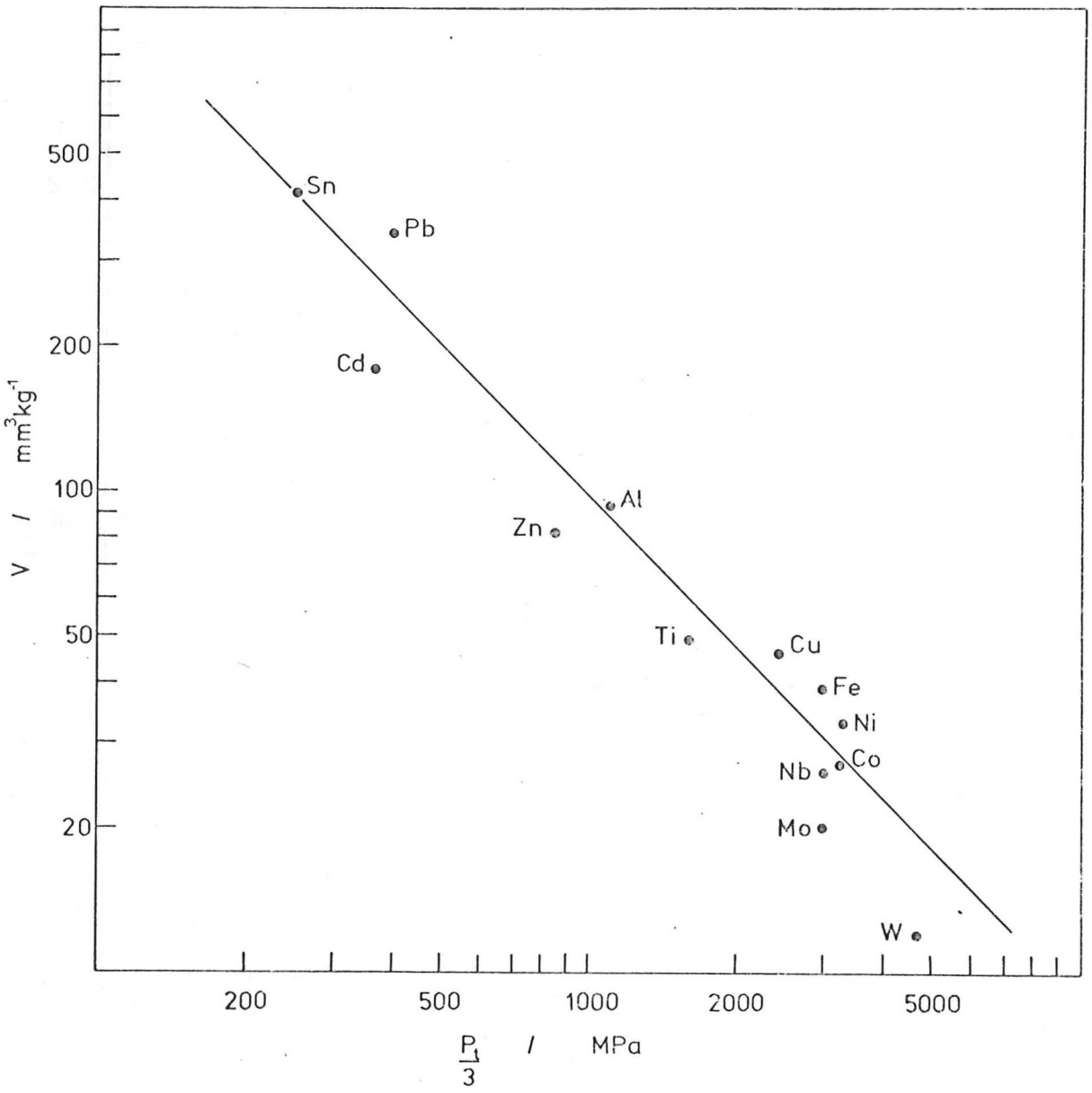

Figure 9.2
Volume erosion rates obtained by Tadolder (1966) using quartz sand at an impact angle of 45^{o} and a velocity of 60 ms^{-1}. plotted against Ascarelli's thermal pressure parameter.

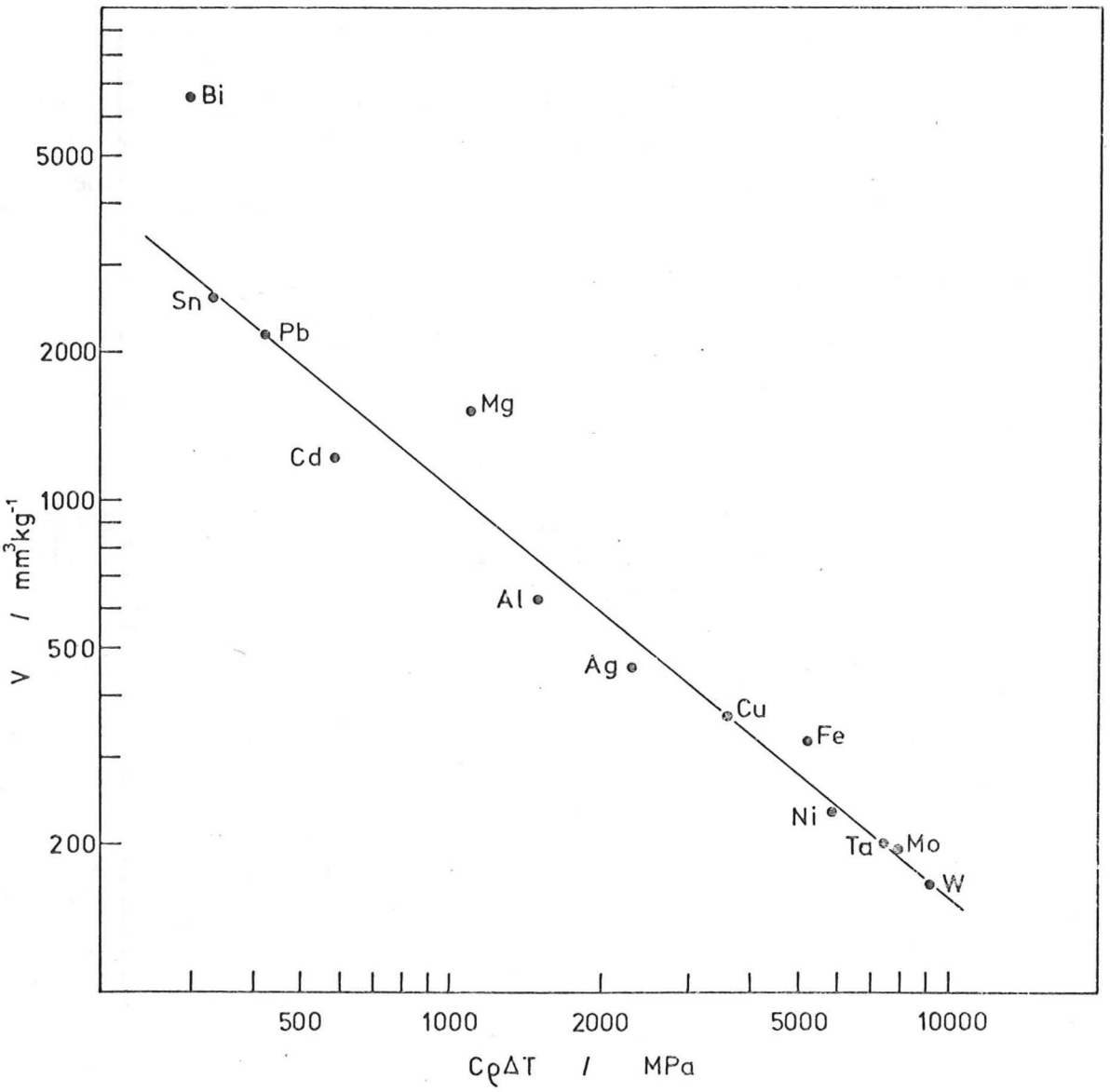

Figure 9.3
Finnie, Wolak & Kabil's (1967) experimental results plotted against the product $C\rho\Delta T$ for several pure metals.

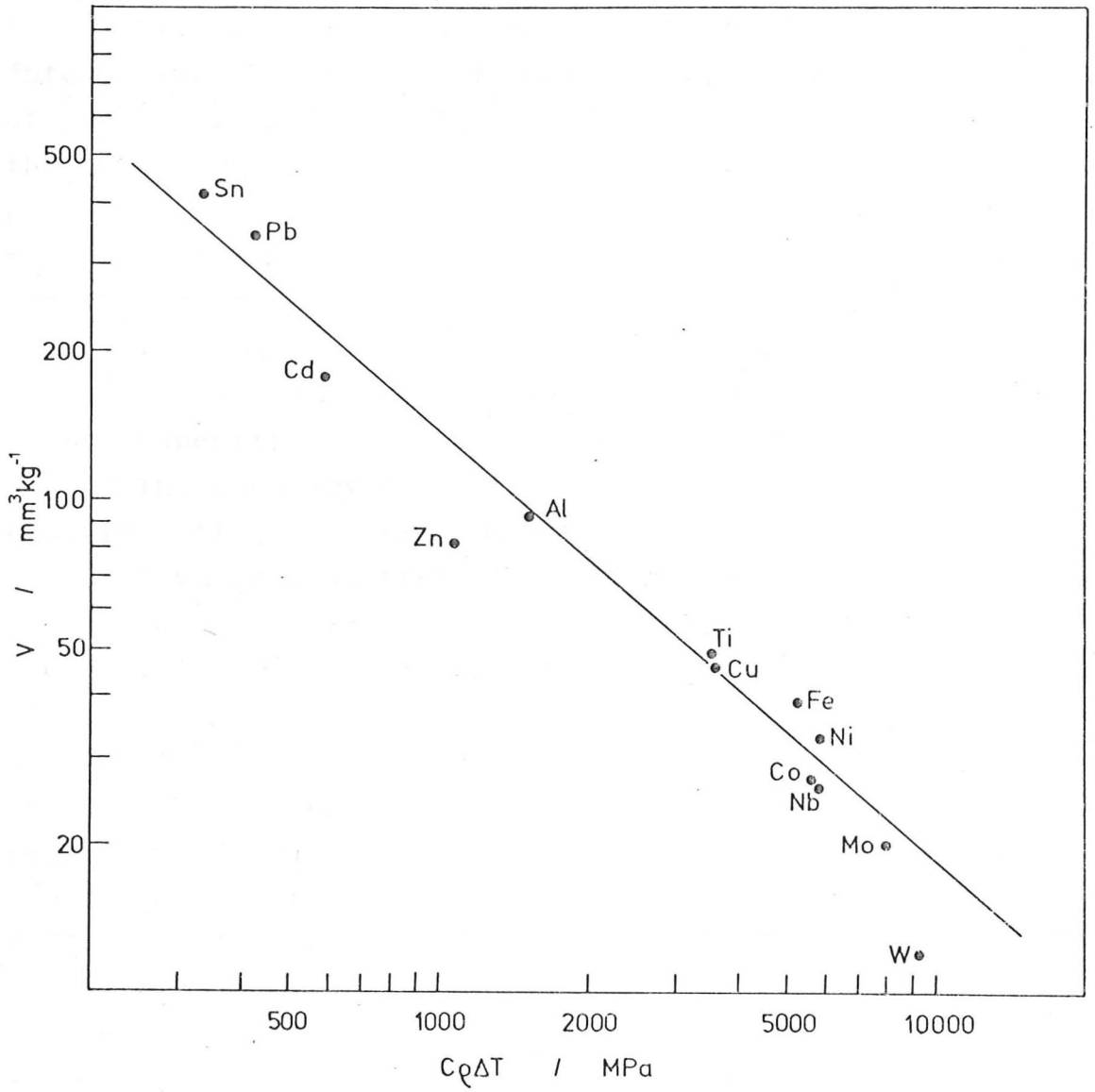

Figure 9.4
Tadolder's results for several pure metals plotted against the product CρΔT.

The correlation is, at worst, ± 25%. An appreciably greater disparity is found, however, between Ascarelli's parameter P_t and the experimental results of Tadolder (figure 9.2). Tadolder tested the metals titanium, zinc and niobium (columbium) which were not tested by Finnie et al., and the ability of Ascarelli's parameter to predict the erosion of these metals is of interest. The departure from the straight line in this graph is rather worse than in figure 9.1.

Figure 9.3 and 9.4 show Finnie's and Tadholder's data plotted against the product $C\rho\Delta T$, which has the units of pressure. While the difference between these graphs and those of Ascarelli's thermal pressure is not great, the prediction of erosion resistance among the more resistant metals (Ti, Cu, Fe, Ni, Co, Nb, Ta, Mo and W) is somewhat moure accurate with the product $C\rho\Delta T$ than P_t. Certainly both P_t and $C\rho\Delta T$ are considerably better indicators of the erosion performance of pure metals than other properties which have been suggested.

The accuracy of these indicators in predicting the behaviour of alloys has not been tested, since no comparative erosion tests have been carried out on a wide enough range of well-characterized alloys. However, Ascarelli's model would predict a much higher rate of erosion of the alloy Invar (Fe + 36% Ni) than of either pure iron or nickel. Invar has a low coefficient of thermal expansion, leading to a low value of P_t, whereas the value of $C\rho\Delta T$ for Invar is close to those for iron and nickel. Gold would be predicted by Ascarelli's theory to suffer a volume erosion less than that of iron and almost as low as nickel, while the $C\rho\Delta T$ parameter for gold is roughly the same as that of silver, which is intermediate in erosion resistance between aluminium and copper. Erosion tests on gold and Invar would therefore yield useful information about the relative value of these two methods of prediction.

While these indicators of erosion resistance do appear to predict the behaviour of pure metals quite well, their limitations and the assumptions made in their use must be appreciated. Since they both yield only one quantity to describe "erosion resistance" there is an inherent assumption that all metals show the same variation of

erosion with angle of impact. As we saw in figure 1.2, this is not so. The values of physical quantities used to determine P_t and $C\rho\Delta T$ plotted in the figures were all room-temperature values; C varies appreciably with temperature, as do α and χ, but allowing for such variation gives slightly worse correlation with erosion than using the values obtained at ~300K. Until more information is available on, for example, the comparative erosion behaviour of several alloys, little more can be decided about the value of these indicators. Although their validity can only be judged empirically, they may nevertheless be practically useful pointers to materials which have good resistance to erosion.

9.6 Conclusions

While it is impossible to list all the conclusions of this work in a short space, an attempt has been made to summarise the main points below.

(i) Spherical particles were shown to remove metal from a plane surface in oblique impacts under certain conditions. The mechanism, ploughing, has not been considered previously by other authors. Angular particles will also remove metal by this process under certain circumstances.

(ii) The process of ploughing involves the formation of a lip at the end of the impact crater, which may be removed by the particle which formed it, or by subsequent impacts. This lip constitutes more than 90% of the weight lost by the surface during the oblique impact of a sphere. Detachment of the lip occurs within a band of intense shear deformation, thought to be an adiabatic shear band.

(iii) Weight losses in normal impacts, and the weight losses in oblique impacts where the terminal lip has not been removed, arise from the fragile tips of ridges extruded to the sides of the projectile. These ridges are not formed in quasi-static indentations.

(iv) Weight losses occurring in the single impacts of spheres were found to correlate well with the weight losses found in multiple impact erosion tests, indicating that the study of single impacts was a valid approach to the erosion problem; a velocity exponent of 2.9 was found for weight losses in single impact experiments. The damage caused by single spheres was found to scale geometrically and scaling rules were established to include the effect of particle density.

(v) The energy required for unit weight loss was found to depend strongly on the impact conditions; the assumption of a constant specific energy made by some theories is false. The fraction of the volume of metal displaced in the impact which is actually removed from the target also

9.6 Conclusions

While it is impossible to list all the conclusions of this work in a short space, an attempt has been made to summarise the main points below.

(i) Spherical particles were shown to remove metal from a plane surface in oblique impacts under certain conditions. The mechanism, ploughing, has not been considered previously by other authors. Angular particles will also remove metal by this process under certain circumstances.

(ii) The process of ploughing involves the formation of a lip at the end of the impact crater, which may be removed by the particle which formed it, or by subsequent impacts. This lip constitutes more than 90% of the weight lost by the surface during the oblique impact of a sphere. Detachment of the lip occurs within a band of intense shear deformation, thought to be an adiabatic shear band.

(iii) Weight losses in normal impacts, and the weight losses in oblique impacts where the terminal lip has not been removed, arise from the fragile tips of ridges extruded to the sides of the projectile. These ridges are not formed in quasi-static indentations.

(iv) Weight losses occurring in the single impacts of spheres were found to correlate well with the weight losses found in multiple impact erosion tests, indicating that the study of single impacts was a valid approach to the erosion problem; a velocity exponent of 2.9 was found for weight losses in single impact experiments. The damage caused by single spheres was found to scale geometrically and scaling rules were established to include the effect of particle density.

(v) The energy required for unit weight loss was found to depend strongly on the impact conditions; the assumption of a constant specific energy made by some theories is false. The fraction of the volume of metal displaced in the impact which is actually removed from the target also

varies with velocity; the theoretical approaches assume it constant.

(vi) High-speed photography of the impact of a sphere on a plane provides a versatile technique to measure the coefficient of friction under impact conditions (high load and sliding speed). The values obtained agree well with those of other workers; this method eliminates some of the restrictions of previous approaches.

(vii) The mean indentation pressure beneath a normally impacting sphere on a steel surface, although always higher than that in static indentations, was found to fall with increasing velocity of impact. Large differences were found in the pattern of deformation below dynamic and quasi-static indentations. Thermal softening of the steel during rapid deformation was felt to be responsible for the drop in indentation pressure and to account for the different deformation patterns.

(viii) Thermal softening was suggested as an important process in the removal of metal by an impacting erosive particle, and a simple predictor of erosion resistance was developed from this idea and found to correlate well with experimental data.

The following lines of research are suggested as a continuation of the work described here.

(i) This work has suggested that thermal softening plays an important role in the erosion of ductile metals, and the simple product $\rho C \Delta T$ shows encouraging agreement with the experimentally determined erosion resistance of many pure metals. More data, however, are needed on the erosion resistance of alloys under controlled conditions, and a more rigorous theoretical analysis of thermal softening under adiabatic deformation conditions should be attempted.

(ii) The study of impacts on other materials using the techniques of chapters seven and eight would be informative.

In particular, the influence of work-hardening rate on the impact process and on the variation of dynamic yield pressure with velocity of impact would be of interest. In view of the results obtained already on copper (chapter four), work-hardened and annealed copper might be suitable metals. Inscribed grids could profitably be used to study the pattern of sub-surface deformation. The effect of adiabatic shear susceptibility might be studied by using titanium targets; titanium forms adiabatic shear bands very readily.

(iii) A theoretical analysis of the oblique impact of a rigid sphere on a plastic plane would be of great interest and would aid further analysis of the results presented in chapter seven. A simple analysis might be based on the assumption of a constant yield pressure as made by Tabor (1951) in his model of the normal impact, but it is not clear what physically reasonable simplifying assumptions may be made to render the analysis tractable.

UNIVERSITY LIBRARY CAMBRIDGE

References

Arbiter N. Harris C.C. & Stamboltzis G.A.	1969	Trans.ASME 244 118-132
Ascarelli P.	1971	AMMRC Tech.Rept. 71-47
Barnsley D.A. Meredith J.R.P. & Robinson M.H.	1968	RARDE Memo. 39/68
Bitter J.G.A.	1963a	Wear 6 5-21
Bitter J.G.A.	1963b	Wear 6 169-190
Bowden F.P. & Freitag E.H.	1958	Proc.Roy.Soc. A 248 350-367
Bowden F.P. & Persson P.A.	1961	Proc.Roy.Soc. A 260 433
Bowden F.P. & Tabor D.	1950	"The Friction and Lubrication of Solids" Part I . Oxford
Brauer H. & Kriegel E.	1965	Chemie-Ingenieur-Technik 37 265
Campbell J.D.	1973	Mat.Sci. & Eng. 12 3-21
Campbell J.D. & Ferguson W.G.	1970	Phil.Mag. 21 63
Carrington W.E. & Gayler M.L.V.	1948	Proc.Roy.Soc. A 194 323
Charters A.C. Gehring J.W. & Maiden C.J.	1966	AGARDograph 87 247-296

Constable F.H.	1928	Proc.Roy.Soc. 117 376
Daish C.B.	1972	"The Physics of Ball Games" EUP
Davies R.M.	1949	Proc.Roy.Soc. A 197 416-432
Davis C.D. & Hunter S.C.	1960	J.Mech.Phys.Solids 8 235-254
Fehndrich W.	1969	Mitt.V.G.B. 49 58
Feigl F.	1954	"Spot Tests" vol. I.Elsevier
Finnie I.	1958	Proc.3rd.U.S.Cong.Appl.Mech. 527-532
Finnie I.	1960	Wear 3 87-103
Finnie I.	1972	Wear 19 81-90
Finnie I. & Kabil Y.H.	1965	Wear 8 60-69
Finnie I. & Oh H.	1966	Proc.1st.Cong.Int.Soc.Rock Mech. 2 99
Finnie I. Wolak J. & Kabil Y.	1967	J.of Materials 2 682-700
Fowles G.R. Duvall G.E. Asay J. Bellamy P. Feistmann F. Grady D. Michaels T. & Mitchell R.	1970	Rev.Sci.Inst. 41 984-996
Gane N. & Cox J.M.	1970	Phil.Mag. 22 881

Goldsmith W.	1960	"Impact" Edward Arnold, London
Goldsmith W. & Lyman P.T.	1960	Trans.ASME E 27 717-725
Goldsmith W. & Yew C.	1962	Proc.4th.U.S.Nat.Cong.Appl.Mech. 177
Goodwin J.E. Sage W. & Tilly G.P.	1969	Proc.Inst.Mech.Engrs. 184 279-291
Graham D. & Baul R.M.	1972	Wear 19 301-314
Head W.J. & Harr M.E.	1970	Wear 15 1-46
Head W.J. Lineback L.D. & Manning C.R.	1973	Wear 23 291-298
Head W.J. Pacala T. & Poole J.	1967	Final rept. on phase 1 of Allison-Purdue dust technology program. Man-Mobility-Survivability Forum
Hertz H.	1881	J.Reine Angew.Math. 92 156 more accessible discussion in e.g. Timoshenko (1934) see below
Hunter S.C.	1957	J.Mech.Phys.Solids 5 162-171
Huston A.E.	1964	Appl.Optics 11 1231
Hutchings I.M. & Winter R.E.	1974	Wear 27 121-128
Ishlinsky A.J.	1944	J.Appl.Math.Mech.(USSR) 8 233
Johnson K.L.	1970	J.Mech.Phys.Solids 18 115
Johnson W.	1972	"Impact Strength of Materials" Edward Arnold

Jones J.R. & Gardos M.N.	1971	Lub.Eng. 27 393-399
Kinslow R. (ed.)	1970	"High-velocity Impact Phenomena" Academic Press
Kleis I.R.	1967	Russian Eng.J. 47 (8) 52
Kleis I.R.	1969	Wear 13 199-215
Kleis I.R. & Uuemyis K.K.	1971	Russian Eng. J. 51 13-15
Krushchov M.M.& Babichev M.A.	1956	Friction & Wear in Machinery 11 5-18
Lepikson H.H. & Siimpoeg R.V.	1969	Trud.Tallinsk.Politech.Inst. 271A 31-39
Miles A.W. & Pearson G.C.	1974	Rev.Sci.Inst. 45 459
Moore M.A.	1974	Wear 27 1-17
Mulhearn T.O. & Samuels L.E.	1962	Wear 5 478-498
Muravkin O.N. & Riabchenko A.V.	1960	Friction & Wear in Machinery 11 69-97
Neilson J.H. & Gilchrist A.	1968a	Wear 11 111-122
Neilson J.H. & Gilchrist A.	1968b	Wear 11 123-143
Newton I.	1704	"Opticks"
Perfect D.A.	1966	RAE Tech.Rept. TR66008
Raask E.	1969	Wear 13 301-315
Recht R.F.	1964	J.Appl.Mech. June 1964 189-193
Routh E.J.	1905	"Dynamics of a System of Rigid Bodies" London

Rubenstein C. Groszman F.K. & Koenigsberger F.	1966	Proc.Int.Ind.Diamond Conf.Oxford 161
Sage W. & Tilly G.P.	1969	Aero.J. of Roy.Aero.Soc. (1969) 427
Seigel A.E.	1965	AGARDograph 91
Sheldon G.L.	1970a	Trans.ASME D 92 619
Sheldon G.L.	1970b	footnote to Smeltzer C.E., Gulden M.E. Compton W.A. J.Basic Eng. Sep.1970 652-653
Sheldon G.L. & Finnie I.	1966a	Trans.ASME B 88 393
Sheldon G.L. & Finnie I.	1966b	Trans.ASME B 88 387
Sheldon G.L. & Kanhere A.	1972	Wear 21 195-209
Smeltzer C.E. Gulden M.E. McElmury S.S. & Compton W.A.	1970	USAAVLabs Tech.Rept. 70-36
Tabor D.	1948	Proc.Roy.Soc. A 192 247-274
Tabor D.	1951	"The Hardness of Metals" Oxford
Tabor D.	1970	Rev.Phys. in Technology 1 145-180
Tadolder Yu.A.	1966	Trud.Tallin.Politech.Inst. A 237 15-22 & 3-13
Taylor G.I.	1946	J.Inst.Civil Engrs. 26 486

Taylor G.I. & Davies R.M.	1942	Sci.Papers of Sir G.I.Taylor vol.I 480 . Cambridge 1958
Taylor G.I. & Quinney H.	1934	Proc.Roy.Soc. A 143 307-326
Thunborg S. Ingram G.E. & Graham R.A.	1964	Rev.Sci.Inst. 35 11
Tilly G.P.	1969a	Wear 14 63-79
Tilly G.P.	1969b	Wear 14 241-248
Tilly G.P.	1973	Wear 23 87-96
Tilly G.P. & Sage W.	1970	Wear 16 447-465
Timoshenko S.	1934	"Theory of Elasticity" McGraw-Hill
Uetz H. & Gommel G.	1966	Wear 9 282-296
Vincent B.J. Gee R. & Hunter S.C.	1957	Proc.Conf.Props.Matls.High Rates of Strain London 51-65
Wahl H. & Hartstein F.	1946	"Strahlverschleiss" Franck'sche Verlagshandlung Stuttgart
Wellinger K.	1949	Z.für Metallkunde 40 361
Wingrove A.L.	1971	J.Austr.Inst.Metals 16 67
Winter R.E.	1971	Ph.D. Thesis University of Cambridge
Winter R.E. & Hutchings I.M.	1974	Wear 29 181-194

Wood C.D.	1966	Proc.Inst.Environ.Sci. 55 63
Yew C.H. & Goldsmith W.	1964	Trans.ASME E 31 635-646
Zener C. & Hollomon J.H.	1944	J.Appl.Phys. 15 22-32

UNIVERSITY LIBRARY CAMBRIDGE